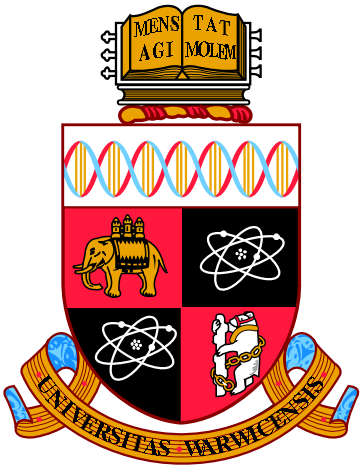

Green Technology: Storing Energy in Nanostructures

by

Volker Gerhard Keinhorst

Thesis

Submitted to the University of Warwick

for the degree of

Doctor of Philosophy

Department of Physics

December 2014

THE UNIVERSITY OF WARWICK

Contents

List of Tables

List of Figures

Acknowledgments

Foremost, I would like to thank my supervisor Dr. Jeremy Sloan for his guidance and support throughout my PhD project. I would have never been able to finish my thesis without access to his immense knowledge, his motivation and his patience. Thank you for being a truly great supervisor!

I would also like to thank my second supervisor, Dr. Neil Wilson, for all his help and guidance, as well as Dr. Ana Sanchez and Dr. Richard Beanland and the rest of the Microscopy at Warwick group for hosting (and putting up with) me during my time at Warwick.

A big thank you goes to Dr. Reza Jalili Kashtiban, for all the help he has provided, in particular with regards to operating and training with the TEMs. I am also particularly grateful to Dr. Matthew Weyland of Monash University, Melbourne, Australia, for all his work.

Special thanks go to Steve York, Steven Hindmarsh and Tom Orton for helping me whenever a piece of equipment failed, even if it was me breaking it, as well as all the training they provided for me. I would also like to thank Dr. Ben Douglas for training me in the use of the porosimeter, and for all the provided help. Thanks also go to Dr. David Walker for training me in the use of the XRD machines.

A special shout-out goes to Adam, Alex, Josh, Keith and the other inhabitants of Office MAS1.06, as well as Sally and Ben, Anja, Sam and Mike of Office PS1.31 and the members of WURC.

I would like to say a special thanks to Dr. Jeremy Sloan, Dr. David Leadley, Karl West, Karen Jewison, Bob Lilley and Jason Yardley for making my MPAGS placement both possible and enjoyable.

Finally, this thesis would never have happened without the undying support and motivation of my parents and siblings: Gerhard Keinhorst, Dr. Annette Keinhorst, Heike Keinhorst and Carsten Keinhorst. Likewise, I am very grateful for Ewelina Pior and her unwavering support, wit and patience, especially as I had to spend a large amount of time finishing off my thesis abroad. Thank you all for keeping me sane, endless spell checking and all the other millions of little things you have done for me.

I would like to acknowledge, and am very grateful for, the funding for my PhD work by the Warwick Centre for Analytical Science under the supervision of my supervisor, Dr. Jeremy Sloan.

And thank you to you, the reader, for taking the time to read this document.

Declarations

This thesis is submitted to the University of Warwick, UK, as part of the requirements for the admission to the degree of Doctor of Philosophy. The work described within was performed during the period from October 2010 to December 2014 under the supervision of Dr. Jeremy Sloan and Dr. Neil Wilson and, unless otherwise specified, was carried out by myself.

Electron microscopy measurements were undertaken at the Microscopy at Warwick group facility. Transmission electron microscopy was performed with the help of Dr. Jeremy Sloan and Dr. Reza Kashtiban.

BET experiments were conducted at the Department of Chemistry, University of Warwick, UK.

Electron Tomography work was carried out on samples produced in Warwick by Dr. Matthew Weyland of Monash University in Melbourne, Australia.

XRD measurements were conducted at the X-ray diffraction suite at the University of Warwick.

Abstract

This thesis presents the work carried out on two types of nano-particle materials with the purpose of investigating their lithium ion storage properties. Several different types of morphologies of tin disulfide were grown hydrothermally, including several known and two novel morphologies. These have been extensively characterised using both electron microscopy and computational simulation, which led to a good understanding of the topology of the particles. In a further step, these were tested electrochemically in lithium ion test cells to elucidate their lithium ion storage properties. While it was possible to reversibly store a significant amount of lithium, the cells unfortunately could not yet compete with other available lithium ion cells.

In addition, a hybrid material composed of lithium niobate and lithiated niobium sulfide was also investigated. For this, a lithium niobate precursor was created using either a hydrothermal synthesis or commercially available material. The synthesis route was shown to be able to produce lithium niobate, but unfortunately still contained other niobium oxide contaminants. Both were sulfidised using a novel approach and shown to exhibit layered shell growth as would be expected for lithiated niobium sulfide. Initial test cells were constructed and tested, but solid electrochemical results could not be gathered before the end of the project.

Chapter 1

Introduction

1.1 Motivation and Aim

Over the last sixty-five years, the world has undergone some extremely significant changes. The world population has risen by 180% from 2.52 billion in 1950 to 7.18 billion in 2014 [U.S. Census Bureau [2013]]. At the same time, energy consumption in general and of each individual has increased dramatically as well (see Figure 1.1 and Figure 1.2) [Tverberg [2012]].

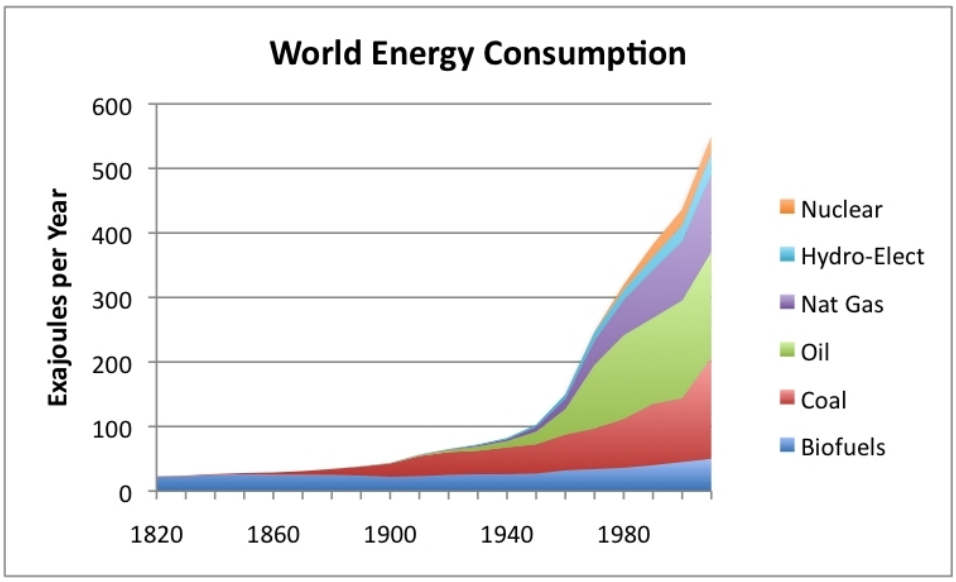

Figure 1.1: *World energy consumption by source, based on Smil's estimates [Smil [2010]] together with BP statistical data for 1965 onwards [British Petroleum [2014]]. From [Tverberg [2012]].*

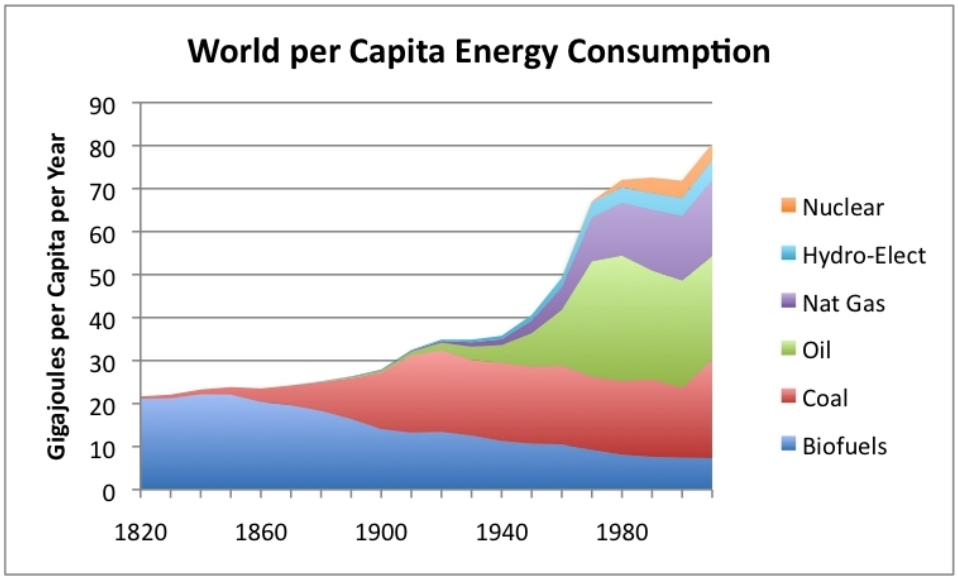

Figure 1.2: *World energy consumption per capita by source showing the increase in personal energy consumption. From [Tverberg [2012]].*

This development has left the world with a bigger population demanding higher energy consumption. This, however, is not solely a problem of power generation, but also a significant problem of power distribution. Innovation in power grids and fuel distribution networks can compensate for this to a degree, but it is also necessary to find better ways of storing and transporting power, particularly electricity, off-grid.

The energy is broadly consumed in four major sectors: industry; transport; residential; and services. Within today's 28 EU member states, the relative total energy consumption between 1990 and 2013 has been as follows (see Table 1.1):

	1990	1995	2000	2005	2010	2013
Total EU-28	1080.0	1078.8	1130.6	1186.4	1158.2	1104.6
Industry	367.6	329.5	331.9	326.9	286.5	277.0
Transport	284.2	306.8	345.2	369.6	364.6	348.4
Residential	273.6	283.6	294.4	305.6	311.6	295.8
Agriculture	31.6	30.6	27.7	27.2	24.7	23.4
Services	109.0	115.4	117.7	144.3	159.6	153.4
Other	13.0	12.1	12.7	11.9	10.3	5.4

Table 1.1: *Final energy consumption in the EU-28 by sector (in million tonnes of oil equivalent, Mtoe) [EUROSTAT [2015]].*

Even if, as indicated in Table 1.1, the total final energy consumption in the EU-28 has incidentally been broadly constant since 1990, this does not mean that nothing has happened within the different sectors. Between 1990 and 2013 the most significant drop in total energy consumption happened in the industrial sector (-90.6 Mtoe/-25 %), which was, however, overcompensated by total energy consumption increases in the services (+44.4 Mtoe/+41 %) and transport sectors (+64.2 Mtoe/+23 %). Reasons behind this development were in the industrial sector the economic crisis which set in in the middle of the years 2000, energy savings measures in the widest sense, and a shift from industrial production to services, and in the transport sector the increasing mobility in Europe of people and goods after the fall of the Soviet Union. During the same period, total energy savings in the agricultural sector were in a comparable order of magnitude (-8.2 Mtoe/-26 %), whilst total energy consumption in the residential sector increased slightly (+22.2 Mtoe/+8 %).

One of the drivers behind the consumption changes in residential sector as seen in Table 1.1 has been the rise of the silicon age, where more and more people are using electronic devices for all kinds of purposes, from entertainment to work to instrumentation to safety features, leading to a significant increase in total electricity consumption of these devices (see Table 1.2).

	1990	2010	2030
OECD North America	80	200	400
OECD Pacific	8	80	160
OECD Europe	64	160	320
Rest of World	48	80	840
Total consumption	200	520	1720

Table 1.2: *Estimated electricity consumption (in TWh) by ICT (information and communication technologies) and CE (consumer electronics) equipment in the residential sector by region from 1990 to 2030. [International Energy Agency [2009]]*

In 1965, Moore predicted that over the history of computing hardware, the number of transistors in a dense integrated circuit will double approximately every two years [Moore [1965]]. This prediction, which was later called 'Moore's Law', is still valid today. Due to the developments in material science and miniaturisation as described by Moore's Law, it has become possible to further shrink these electronic devices down and make them portable, while at the same time increasing the number

of built-in features. As a consequence, the power consumption of these miniaturised devices increased, making it necessary to provide them with improved means of storing energy in a portable fashion. As miniaturisation doesn't allow to simply increase battery size, it becomes necessary to improve the storage characteristics of these batteries by other means.

And a third and final point to consider is the current trend in the ever-changing climate. The global greenhouse effect has been under constant debate for some time and a clear conclusion is that the continued use and expansion of 'dirty' energy sources, which produce gases and waste which contribute to the change in the climate, is not sustainable in the long run. The fossil fuels are the biggest fuel source under debate in this regard. Their dominance in use for electrical energy production is increasingly being challenged by novel technologies such as renewable or fusion energy. Furthermore, their dominance in the transport sector as the energy carrier for cars and engines is also being slowly challenged by the introduction of electric cars. These have long suffered from severe drawbacks such as low range or long charging times. Recently, however, the world has seen the development of electric cars that can rival fossil fuel cars, most notably the Model S produced by Tesla, which uses an array of lithium ion batteries as sole means of energy storage [Tesla Motors Inc. [2014]]. The car is being powered by 7104 modified Panasonic NCR18650 lithium ion batteries [Panasonic [2015]] with nickel-cobalt-aluminium cathodes assembled in so-called battery packs [Mollenkopf [2011]]. An additional big advantage contributing to the rise of these batteries in the automotive industry has also been their weight, which is far lower than that of a comparable lead-acid battery.

This project is aimed at investigating particular materials for the use in lithium ion batteries. These batteries are used in practically all modern electrical devices, ranging from mobile phones over laptops to cars and planes. Due to a high energy density, no significant memory effect and only a slow loss of charge when not in use, these batteries are currently one of the most popular types of low-weight rechargeable batteries for portable electronic devices. They are therefore a central pillar in the global energy storage challenge, and constant scientific research is undertaken to improve their capabilities, in particular regarding increased high-power capabilities without decreasing battery life-times. Nanomaterials seem to offer advantages regarding better strain accommodation in high-capacity electrodes, allowing for the reversible extraction of more stored energy whilst not reducing cycle life-time [Venugopal et al. [2010]]. This was an essential point for the decision to investigate novel morphologies of SnS_2 in this project, as these potentially promised

an even higher resistance to strain via their complex shapes. The choice of lithium niobates was also promoted by better strain resistance, but here it promised to come from the combination of a flexible outer sulfide shell with a strong lithium-saturated niobate inner core. The materials investigated in this project were intended to be used in the electrodes contained within lithium ion cells. First, they were characterised physically to investigate their topological properties and then tested in prototype electrochemical cells. In case of promising energy storage capabilities, an additional aim was to try to investigate the exact relationship between the topology of nano-particles of the produced material and their electrochemical properties, in particular with respect to the relationship between exposed surface areas and the lithium ion storage properties.

1.2 Literature Review

1.2.1 Current Lithium Ion Battery Technology

A lithium ion battery (LIB) is a type of chemical energy storage. Chemical energy storage can be achieved by exploiting a reversible chemical red-ox reaction. During a red-ox reaction, in which energy is released, electrons and ions are exchanged between the reactants to produce more stable, energetically favourable compounds. However, since these are reversible reactions, it is possible to run them in reverse direction under the expenditure of energy. This can, for example, be achieved by applying an external electric potential. By separating the reaction components spatially and insulating them electrically from one another, it is possible to disconnect the external electric potential without the energy-release reaction immediately taking place again. Only by connecting the two reaction components electrically can the reaction take place, whilst electrons move through the external connection and ions move through the internal electrolyte. Thus, it is possible to retrieve the stored electric energy in form of an external electric current, which can be used for a multitude of purposes. In the case of lithium ion batteries, this is achieved by having two electrodes containing the reactants connected internally by an electrically-insulating electrolyte, which only allows the movement of lithium ions, and an external circuit as a carrier of the electron flow (see Figure 1.3).

A large number of modern electrical devices rely on lithium ion batteries. This range includes both traditionally electrical devices such as mobile phones and laptops, as well as devices that conventionally used to rely on other types of stored energy, such as cars. Lithium ion batteries have several strong advantages over other types of energy storage media, which explains the drastic rise in their use. They

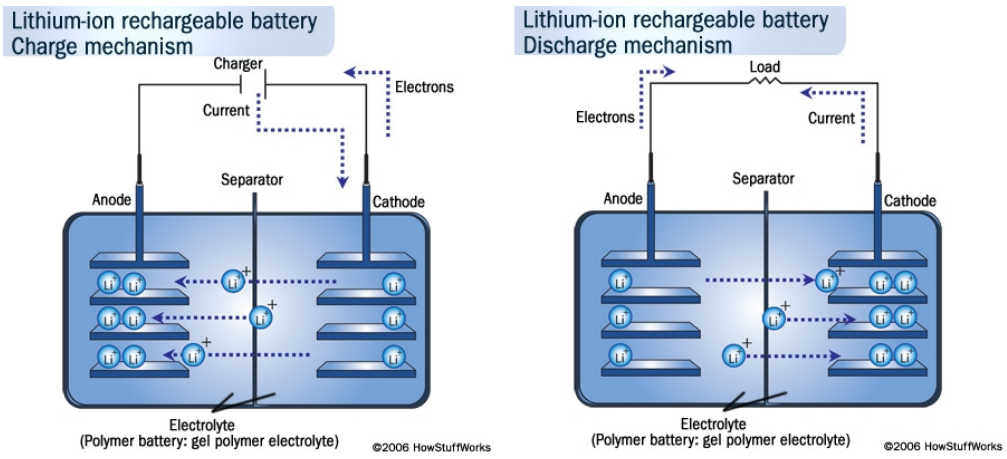

Figure 1.3: *Flow-process diagram of a lithium ion battery charge/discharge cycle. From [Brain [2006]]*

can attain very high energy densities due to the small size of the charge carrier and do not suffer from memory effects that affect conventional battery operation.

The particular specifications and electrochemical properties of lithium ion batteries vary drastically over the range of available cell types. Factors such as cell geometry, electrolyte type or electrode materials have got a strong influence. Handheld devices often rely on LIBs with positive electrodes made from lithium cobalt oxide or lithium iron phosphate. A sample selection of positive electrode materials and their measured charge capacities are shown in Table 1.3. Likewise, common negative electrodes include graphite and other carbon hybrids. A selection of possible materials is listed in Table 1.4. Each material has got certain advantages. For example, early lithium cobalt oxide based electrodes were initially delivering a relatively good storage capacity and chemical stability, but were soon outperformed by modern lithium iron phosphate systems, which provide better safety properties (higher chemical stability, as well as lower toxicity) and higher storage capacities.

Under certain conditions, lithium ion batteries can pose severe safety hazards. The most basic cells use elemental lithium as one of the battery electrodes, which, when it comes into contact with water, can react violently under the production of hydrogen gas and thus pose an explosive hazard. Furthermore, the most common electrolytes are based on flammable organic compounds and contain very toxic lithium salts. The danger is further exacerbated by the fact that most lithium ion batteries are kept pressurized, thus allowing for an easier release of these chemicals from the battery container. In the past (and also in the present, as in the case of the battery fires in Boeing Dreamliners [Mouawad [2014]]), there have been several

Type of Electrode Material	Capacity	Reference
Lithium Iron Phosphate	145 mAh/g, 130 mAh/g	[Chen and Whittingham [2006], Vu and Stein [2014]]
Lithium Cobalt Oxide	130 - 140 mAh/g	[Chen et al. [2002], Wang et al. [2015]]
Lithium Manganese Oxide	250 mAh/g, 220 mAh/g	[Johnson et al. [2005], Choi and Jo [2014]]
Lithium Nickel Manganese Cobalt Oxide	185 mAh/g, 406mAh/g	[Yoshizawa and Ohzuku [2007], Lee et al. [2014]]
Lithium Nickel Cobalt Aluminium Oxide	210 mAh/g, 185 mAh/g	[Chen et al. [2004], Watanabe et al. [2014]]
Lithium Vanadium Phosphate	150 mAh/g, 162.8 mAh/g	[Saïdi et al. [2003], Li et al. [2015]]
Metallic Lithium	3860 mAh/g	[Fauteux and Koksbang [1993]]

Table 1.3: *Positive electrode materials and their charge storage capacity.*

incidents with malfunctioning LIBs, ranging from product recalls to severe fires or explosions. Therefore, testing procedures and standards to ensure safe lithium ion batteries are more strict and severe than for other types of batteries [Basu [1981]].

Historical Development of Lithium Ion Batteries

Storage of electrical energy by means of a lithium chemistry based electrochemical cell was first suggested by M.S. Whittingham in the mid-1970s [Whittingham [1976]]. Whittingham used a prototype cell based on metallic lithium and titanium sulfide in a proof-of-principle experiment. The use of lithium metal had severe drawbacks as it is highly reactive and very unstable if brought into contact with atmospheric air [Kirchhoff and Bunsen [1861]] due to the water content of the atmosphere, as outlined in the previous section. A primary research goal was therefore to develop means to abandon the use of the pure metal and move to safer, more stable electrode alternatives.

Besenhard was able to demonstrate lithium intercalation into both graphite [Besenhard and Fritz [1974], Besenhard [1976]] and cathodic oxides [Schöllhorn et al. [1976], Besenhard and Schöllhorn [1977]] in Germany in the 1970s, as shown in Figure 1.4. This work was of particular importance, as it not only demonstrated the intercalation into these materials, which was known before, but showed that this could be done reversibly, thus paving the way for modern lithium ion cells.

Type of Electrode Material	Theoretical Max. Capacity	Reference
Graphite	372 mAh/g, [Yazami [1999]]	320 mAh/g [Towada et al. [2015]]
Tin Oxide	782 mAh/g, [Sunkara [2014]]	500 mAh/g, [Brousse et al. [1998]]
Silicon	4,200 mAh/g, [Chan et al. [2007]]	1368 mAh/g, [Jiang et al. [2014]]
Lithium Titanate	125 mAh/g, [Tang et al. [2009]]	308 mA h/g after doping with Zr, [Li et al. [2014]]

Table 1.4: *Negative electrode materials and their charge storage capacity. In the final row it can be seen that the theoretical value is exceeded when the material is doped with other elements, zirconium in this case. Some electrode materials lend themselves to this process, especially spinels like lithium titanate.*

At this stage, however, lithium ion cells were still suffering from severe issues with the electrolyte [Besenhard and Eichinger [1976], Eichinger and Besenhard [1976]]. In 1977, S. Basu [Zanini et al. [1978], Basu et al. [1979]] was able to use this information to create a lithium-intercalated graphite electrode as an alternative to the dangerous lithium metal electrodes [Basu [1981]].

Goodenough and Mizushima were investigating compounds of the type $A_xM_yO_2$. This investigation led to the discovery of $LiCoO_2$ [Goodenough and Mizushima [1981]], which quickly became an important compound in the development of lithium ion batteries. $LiCoO_2$ is safe and stable, and it is able to act as a lithium ion donor in electrochemical cells, thus making it possible to construct cells that do not rely on lithium metal as a lithium source. Goodenough and Mizushima were able to demonstrate that it was possible to use this material in electrochemical cells relying on lithium chemistry, which led to their ground-breaking patent in 1981. The use of $LiCoO_2$ allowed for a big range of new possibilities in the development of lithium ion batteries.

Yazami was able to further develop the already known graphite electrodes in 1980 [Yazami and Touzain [1983]]. A solid electrolyte was used to overcome previous issues with organic liquid electrolytes, most notably the undesired decomposition of the electrolyte during cycling. The developed electrode has been widely used in modern, commercially available, lithium ion cells.

Goodenough, Thackeray and co-workers introduced a positive lithium ion battery electrode based on manganese spinels in the early 1980s [Thackeray et al.

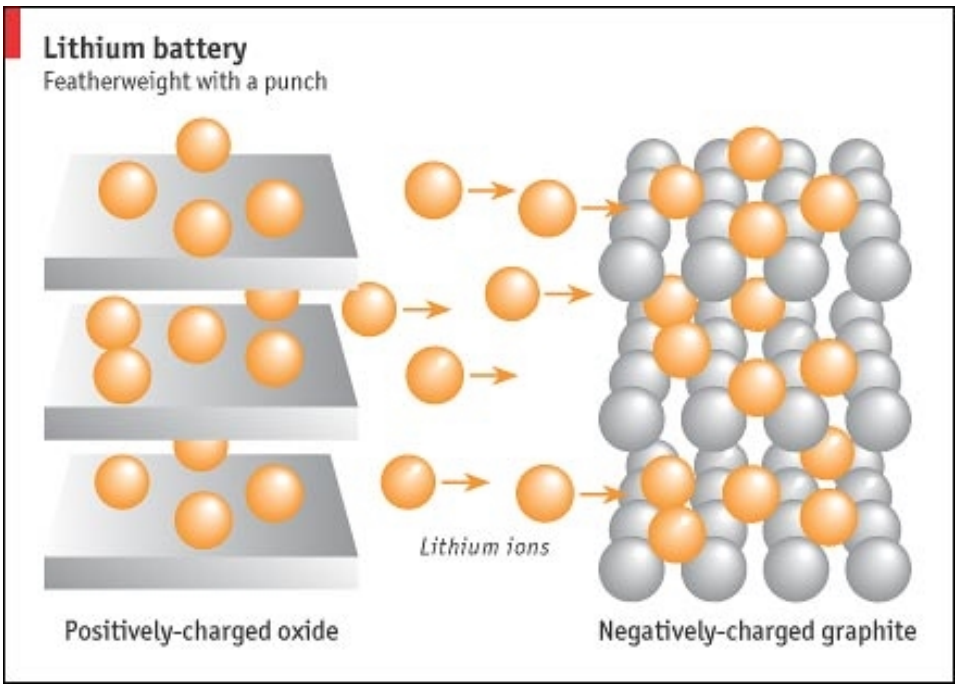

Figure 1.4: *Image showing the intercalation process of lithium ions into a graphitic structure. From [The Economist [2002]]*

[1983]], which demonstrated many positive properties such as low cost and good structural stability, but suffered from poor cycle life. Their continued work has shown that this issue can be addressed by selective doping [Johnson et al. [2005]] and batteries based on the manganese spinels are now available commercially. In the case of spinel structures, it is possible to introduce foreign elements, which then have an impact on the structure of the spinel. This can lead to an opening or closing of internal spaces and channels, and if done correctly, as can be seen in Table 1.4, lead to much improved characteristics for the material with regard to its application in LIBs.

Nevertheless, it took until the mid-1980s for lithium ion batteries to become industrially viable. Yoshino constructed a prototype cell based on lithium cobalt oxide as the positive electrode and graphitic material as the negative electrode, which avoided the dangerous use of elemental lithium [Yoshino et al. [1987]]. Furthermore, lithium cobalt oxide can be produced on an industrial scale, and thus Yoshino's battery can be seen as the first modern lithium ion battery. However, it was not until 1991 that the first lithium ion battery became commercially available to the public, produced by a joint venture between Sony and Kasei [Yoshio et al. [2010]].

In order to increase storage capacity and cycle life, as well as to improve the

usage safety of the cells, intensive research in the field has produced many more different materials for use as positive or negative electrodes, or electrolytes, (for further details see below) and many more are likely to be discovered in the future.

Modern Lithium Ion Batteries

The principal functional components of any lithium ion battery are the two electrodes, anode (negative) and cathode (positive), and the electrolyte connecting the two electrodes ionically. As seen in Table 1.3, the most basic cathode is lithium metal, but for safety reasons modern lithium cells no longer contain the pure metal and use lithium compounds instead. One of the most popular anode materials is still carbon, however, it is also slowly being replaced by materials of higher charge capacity, such as silicon (see Table 1.4).

The electrolyte in a lithium ion battery has to perform two primary tasks. On one hand, it needs to allow lithium ion movement between the electrodes. On the other hand, it needs to be electrically insulating in order to ensure that electrons can only move from one electrode to the other if an external circuit, such as an electronic device like a mobile phone, is applied. In practice, this is done by creating a carrier fluid composed of a mixture of organic carbonates such as ethylene carbonate, diethyl carbonate or dimethyl carbonate, which have found widespread use due to their electronic insulation properties and their non-reliance on water to remain liquid. Decomposition of the organic carrier fluid is a common feature during charging and results in the build-up of a layer on the negative electrode, which can have an impact on overall cell performance. This layer is commonly referred to as the solid electrolyte interphase (SEI) [Balbuena and Wang [2004]]. With the right choice of organic solvents, however, it is possible to create an SEI with favourable properties such as good ionic conductivity and improved stability [Fong et al. [1990]]. A lithium salt, such as lithium hexafluorophosphate ($LiPF_6$), lithium hexafluoroarsenate monohydrate ($LiAsF_6$), lithium perchlorate ($LiClO_4$) or lithium tetrafluoroborate ($LiBF_4$) is then dissolved in the carrier fluid, which can subsequently be used in cell construction. A sample selection of these electrolytes and their conductivities is presented in Table 1.5.

As pure lithium is highly reactive (it reacts vigorously with water to form lithium hydroxide and hydrogen gas), the non-aqueous electrolytes, such as the ones listed in Table 1.5, are typically employed, and a sealed container is used to exclude moisture from the battery pack. However, several aqueous electrolytes, such as $LiNO_3$ in water, have also been developed for use in lithium ion batteries [Li et al. [1994]].

Type of Electrolyte Material	Example Conductivities	Reference
Lithium Hexafluorophosphate ($LiPF_6$)	11.63 mS/cm at 25°C in y-Butyrolactone (BL)	[Chagnes et al. [2002]]
Lithium Hexafluoroarsenate Monohydrate ($LiAsF_6$)	10.48 mS/cm at 25°C in y-Butyrolactone (BL)	[Chagnes et al. [2002]]
Lithium Tetrafluoroborate ($LiBF_4$)	7.33 mS/cm at 25°C in y-Butyrolactone (BL)	[Chagnes et al. [2002]]
Lithium (Trifluoromethylsulfone)-imide (LiTFSI)	9.21 mS/cm at 25°C in y-Butyrolactone (BL)	[Chagnes et al. [2002]]

Table 1.5: *Several common electrolyte salts used in lithium ion cells and their respective conductivities.*

Lithium ion batteries can take on a wide range of different shapes (see Figure 1.5). However, it is possible to split them up into four main categories:

- Small or Large Cylindrical Cells (similar to the standard AA batteries);
- Coin or Button Cells (most common examples are industry standards such as CR2016 or CR2032);
- Pouch Cells (such as mobile phone batteries);
- Prismatic (these can take a range of different shapes, most common examples are laptop or electric vehicle batteries).

Battery Operation

Modern lithium ion batteries rely on the intercalation and de-intercalation of lithium ions in the structural matrices of the host electrodes. During intercalation, lithium ions move into the structure of a material and deposit themselves in structurally favourable positions (as can be seen in Figure 1.6 for the example of graphite, where a lithium ion takes up position in the centre of each hexagonal ring, provided none of the neighbouring rings contains a lithium ion). This can be done via an alloying process, as is the case, for example, with silicon [Chan et al. [2007]], which will become relevant when discussing SnS_2 later. De-intercalation is the reverse process in which lithium ions are released from the host electrode. In the case of lithium intercalation in graphite, the lithium ions enter the structure of the graphite along the layers until they find a valid and favourable position to remain in. During de-intercalation, the ions again begin to move along the space between the layers until

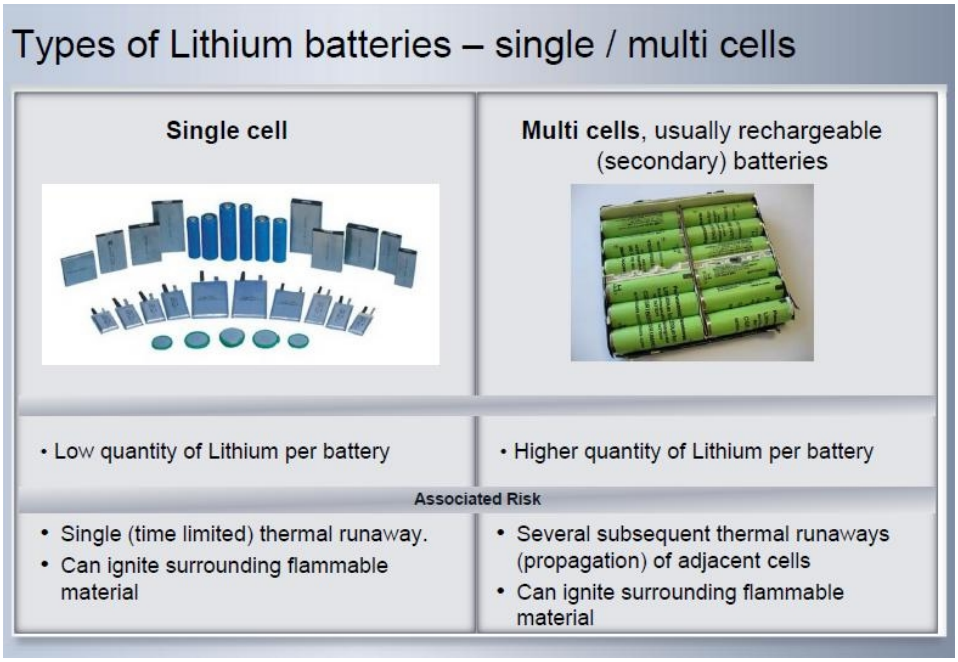

Figure 1.5: *Common types of lithium ion batteries and battery packs, as well as safety concerns for each type. From [Hamilton [2013]]*

they leave the structure. No chemical modification is made to the graphite. The movement of the ions is accompanied by a corresponding electron flow, which needs to occur in order for the intercalation/de-intercalation to take place. By choosing two appropriate electrodes (an anode and a cathode) and an electrolyte, so that the de-intercalated ions from one electrode can intercalate in the other, and by providing an external electrical connection between the two electrodes, it is possible to design a basic battery. If the electric current flows naturally, the cell is discharging and can be used to power electronic devices. If the current does not flow naturally and needs to be forced via an applied electric potential, the battery is being charged. A schematic representation of this process is shown in Figure 1.3.

When the cell is fully or partially charged, connecting the two electrodes with an external circuit causes the electrochemical reactions within the cell to run autonomously, causing an electron current to flow through the external connection, which can be used to power electronic devices. Using a cell based on graphite and lithium cobalt oxide, the two electrode reactions are respectively [Kganyago and Ngoepe [2003], Smart Electronics [2013]]:

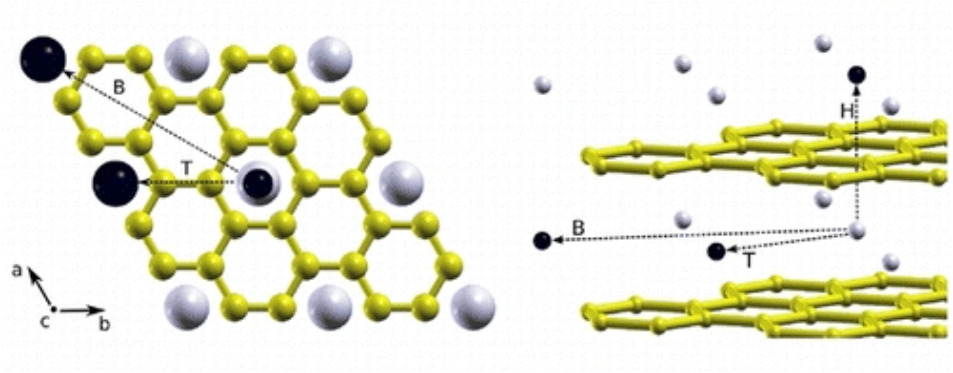

Figure 1.6: *The positions lithium ions (black spheres) take up between two layers of graphite (carbon atoms in yellow). Note that the position of a lithium ion in one carbon ring automatically excludes neighbouring rings from also containing a lithium ion. This gives rise to the maximum capacity of one lithium ion for 6 carbon atoms. From [Thinius et al. [2014]]*

$$xLi^+ + xe^- + xC_6 \leftrightarrow xLiC_6 \tag{1.1}$$

$$LiCoO_2 \leftrightarrow Li_{1-x}CoO_2 + xLi^+ + xe^- \tag{1.2}$$

Here, x gives an indicator of de-intercalation of lithium from the lithium cobalt electrode and intercalation into the graphite electrode. This example is also suitable to show what occurs when the cell is operating beyond its healthy charge states. Over-charging the cell causes the decomposition of lithium cobalt oxide into lithium and cobalt oxide [Amatucci et al. [1996]], while over-discharge leads to the synthesis of lithium oxide and cobalt mono-oxide by supersaturating the electrode with lithium [Choi et al. [2003]].

The ambient temperature also has an impact on the overall battery operation. A higher temperature will lead to an increased reaction rate for the reactions taking place inside the lithium ion cell as would be expected. Arrhenius' Equation demonstrates this dependence of the reaction rate constant k on the temperature T, where A is the pre-factor, E_a is the activation energy of the reaction and R is the universal gas constant [Arrhenius [1889]]:

$$k = A \exp - \left(\frac{E_a}{RT} \right) \tag{1.3}$$

However, if temperatures are too high, unwanted side-reactions may take

place or the cell may slip into thermal runaway, which will be discussed later. This can negatively affect the battery up to the point of explosion. Luckily, lithium ion batteries also show good performance characteristics for low temperatures between 5 - 45 °C [Sony Corporation [2014]], which is suitable for most commercial devices. It is possible to utilise lithium ion cells even below 0 °C, but their performance suffers drastically with temperature dropping to the freezing point of the electrolyte solution. Batteries that have to perform at such low temperatures often come equipped with internal heating circuits that raise the temperature to more desirable levels.

Self-Discharge

As with other types of chemical batteries, lithium ion batteries suffer from a small drain of charge over time if stored in a non–discharged state. This is primarily caused by diffusion of ions within the cell, and can be modelled in the case of lithium ion cells by application of Fick's second law modified for diffusion in porous media [Crank [1976] and Gratwohl [1998]]:

$$\frac{\partial c(x,y,z,t)}{\partial t} = D\frac{\epsilon\sigma}{\tau}\Delta c(x,y,z,t) \tag{1.4}$$

In this equation, D is the diffusion coefficient for lithium ions, while the porosity ϵ represents the fraction of the total volume available for diffusive transport of the electrolyte, σ is the constrictivity and τ is the tortuosity. ϵ represents all possible and available diffusion routes, while excluding those that cannot contribute to the process. The constrictivity describes the shape effects of space available for diffusion, with narrower channels slowing down the process. Tortuosity describes the effect of distorted diffusion paths, as channels that are twisted and bent contribute to slower overall diffusion. If using lithium hexafluorophosphate, D takes a value of $7.5 * 10^{-10}$ m^2/s and $\epsilon_t = \frac{\epsilon\sigma}{\tau} = 0.724$ [Summerfield [2013]].

Typically, lithium ion batteries discharge at a rate of 0.3 - 2 % per month [Sanyo Electric [2004], Harding Energy [2004], Huang et al. [2015]], which is a significant improvement over a discharge rate of around 30% for conventional nickel metal hydride batteries [Winter and Brodd [2004]].

Battery Ageing

A full charge-discharge cycle of a battery is considered a full cell cycle. As the cell is put through more and more cycles, its performance characteristics slowly diminish and overall storage capacity drops. This effect is commonly referred to as cell ageing and a wide range of factors contribute to it. As previously mentioned, over-charging

and over-discharging reduces the integrity of the electrodes, the inappropriate setting of charge or discharge currents damages the structure of the electrodes, and the ambient temperature can also contribute to the degradation of the overall storage capacity. The lifetime of a battery is therefore usually quoted in completed cell cycles before the actual cell capacity drops below a set nominal value, as opposed to in units of time. For commercially available cells, this value is around 80% of the original capacity. The previously mentioned Panasonic NCR18650 batteries for example have a cycle life of around 300 cycles [Panasonic [2015]]. It should be noted that this method of measuring cell lifetime is only appropriate where one can assume that the total number of cycles will be performed before time-effects become noticeable. Modern cell lifetimes vary strongly, but it is possible to construct cells with lifetimes beyond 10000 cycles [Wilka [2013]].

Battery Safety Concerns

Due to the safety drawbacks mentioned above of using elemental lithium (see Figure 1.7), modern LIBs no longer contain pure lithium, but rather lithium intercalated into the working electrodes.

Figure 1.7: *Cell failure can lead to severe volume increases as seen in this example. In the worst case, the cell bursts and either catches fire or releases toxic chemicals. From [Mpt-Matthew [2013]]*

This also prevents a phenomenon referred to as lithium dendritic growth, during which lithium collects at preferential locations on the electrode surface. As can be seen in Figure 1.8 (a), this preferential deposition results in the creation of

lithium growths on the otherwise flat electrode. These growths, due to their shape, are commonly referred to as 'lithium dendrites'. They still provide lithium ions for the general operation of the cell, but over time grow in size, which can eventually short-circuit the cell internally by bridging the electrodes with a direct lithium metal wire or bridge. On non-elemental lithium electrodes, lithium is not directly deposited on the electrode, but rather intercalated into the electrode structure, as can be seen in Figure 1.8 (b). Therefore, the problems caused by preferential deposition sites no longer exist.

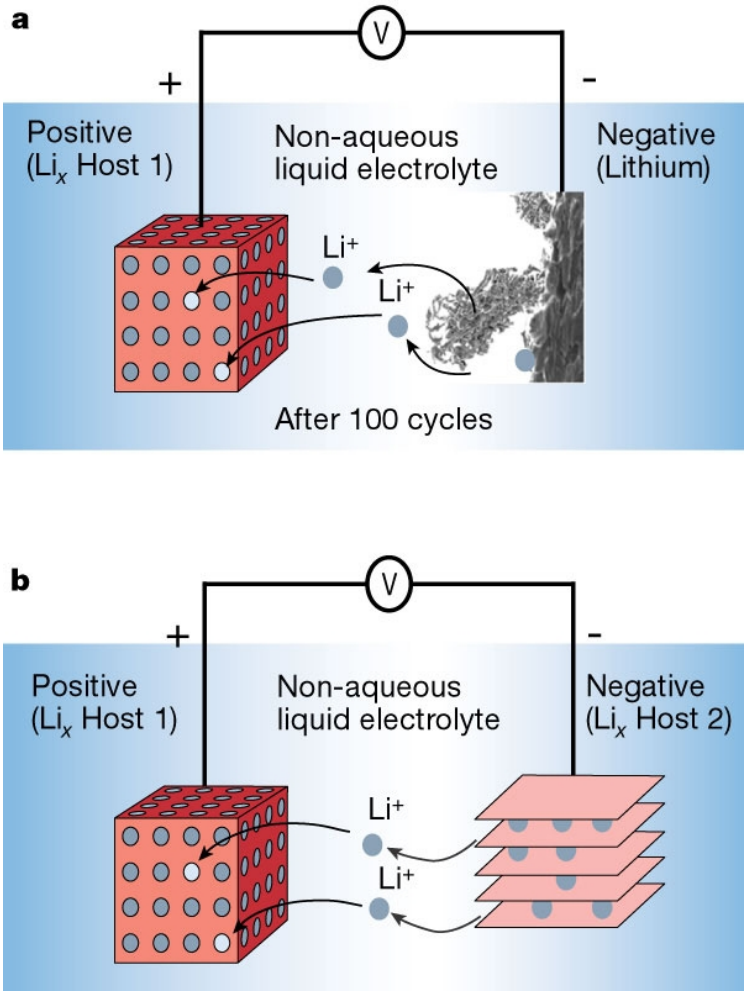

Figure 1.8: *(a) The secondary electron image shows a real-life view of a lithium dendritic structure as grown in a cell. (b) shows that the same issue does not occur for non-metallic lithium electrodes. From [Tarascon and Armand [2001]]*

However, lithium ion batteries are still susceptible to an effect called thermal

runaway. This is caused by a malfunction of the battery, caused by either applying too strong charge currents or causing the battery temperature to rise by some other means. The increased temperature causes the ionic current in the cell to increase via increased reaction rates, which in turn further heats the battery. Eventually, either the battery bursts into flames or the casing experiences an explosive failure. Several safety features are included in LIBs to prevent such catastrophic failure. The five most notable are [Smart Electronics [2013]]:

- A Shut-down separator (prevents thermal runaway by melting at high temperatures and sealing all ion channels);
- A Tear-away tab (designed to prevent pressure to build up inside the cell case);
- A Vent (provides pressure relief in case of internal pressure build up);
- A Thermal interrupt (prevents overcharging by shutting down the cell if temperatures rise too high);
- A Safety circuit (to prevent operation outside of the safe voltage window).

A full schematic of a modern cylindrical lithium ion cell including all its safety features is shown in Figure 1.9.

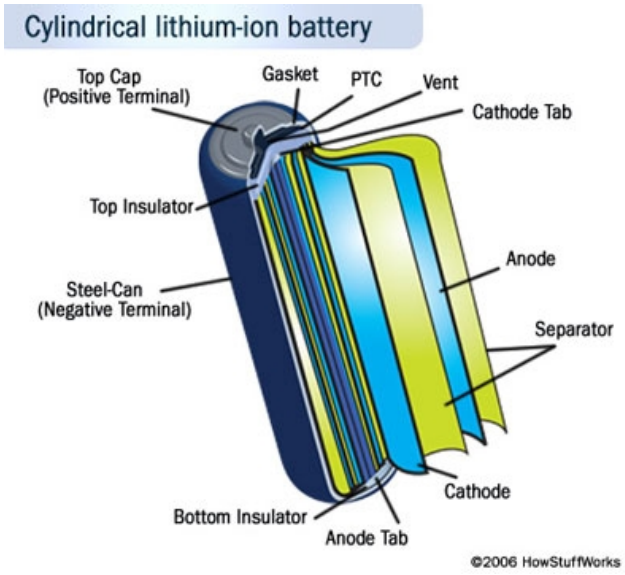

Figure 1.9: *Full schematic of a lithium ion cell including all common safety features: Pressure Vent; Separator; and Positive Thermal Coefficient (PTC) device. From [Brain [2006]]*

1.2.2 The Use of SnS_2 as Lithium Intercalation Material

When researchers around Zhu [Zhu et al. [2005]] discovered that tungsten disulfide was capable of forming layered structures such as nano-tubes [Rothschild et al. [2000]] or -sheets [Elias et al. [2013]] that likened their carbon-based counterparts, this marked the birth of a new class of materials. This class was named inorganic fullerenes in tribute to their likeness to carbon-based fullerenes. Over the years, the membership of the group of these materials has steadily grown and nowadays ranges from chalcogenides, such as molybdenum sulfide MoS_2, to materials such as boron nitride, BN.

Particular interest lay with sulfide-based materials of the type MS_2. Materials of this type are often members of the group of inorganic fullerenes. Their layered superstructures lend themselves to the intercalation of smaller ions, such as lithium. By having a sufficiently large layer spacing, these materials allow lithium to diffuse deep into the material relatively easily and, therefore, at relatively high speeds. Conversely, if the layer spacing is too small, diffusion will be hindered or stopped altogether. By designing a material that exposes a maximum area of open layers of sufficient layer spacing, it should therefore be possible to create very high-performing electrodes for lithium ion batteries. A further advantage of these types of sulfide-based materials is the presence of the sulfur atoms. These can react with lithium irreversibly under the creation of a lithium sulfide buffer matrix that adds stability to the overall structure.

As already stated above, SnS_2 is part of the family of inorganic fullerenes. When crystalline SnS_2 forms, it forms layers of material, as seen in Figure 1.10. Each layer consists of three sub-layers. Sulfur atoms form the two outer layers and sandwich a layer of tin atoms in between them. These three sub-layers form a standard single layer of SnS_2. The force holding two adjacent layers of SnS_2 together are Van Der Waals forces and the spacing from tin layer to tin layer is around 0.59 nm [Hong et al. [2003]]. This space is sufficiently large to allow an easy diffusion of lithium ions along the layers.

As mentioned above in Equation (1.1), when lithium intercalates into carbon, it is possible to store up to 1 lithium ion per 6 carbon atoms. When using elemental tin, however, it is possible to achieve a theoretical maximum of 4.4 lithium ions per tin atom. This means an improvement from $8.36 * 10^{21}$ Li-ions/g for carbon to $2.23 * 10^{22}$ Li-ions/g for tin. This is an improvement of roughly 166%. However, using elemental tin also has its drawbacks, most notably its poor performance in terms of cycle life. This is due to severe volume changes that the material undergoes when lithium intercalates. For some materials, such as silicon (which is also able to

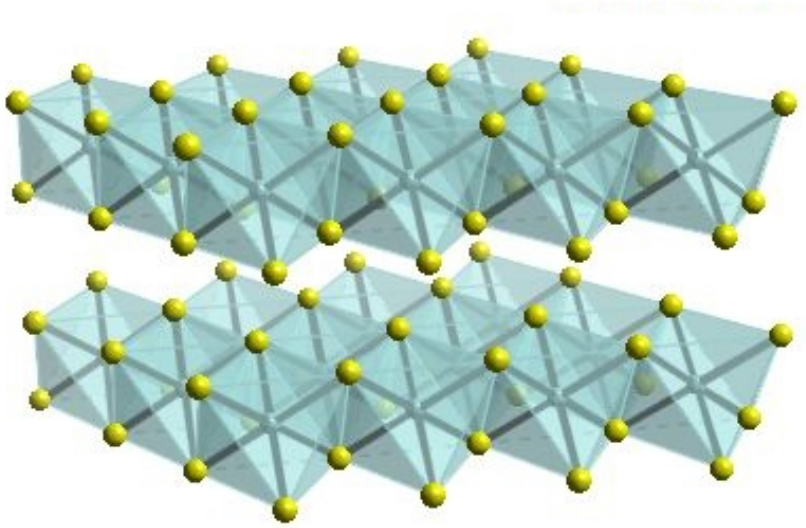

Figure 1.10: *Schematic representation of the structure of tin disulphide. Sulfur is displayed as yellow spheres, tin as grey spheres. From [Brain [2006]]*

store 4.4 lithium ions per atom), this can be as high as 400% [Chan et al. [2007]]. These volume changes cause cracks to appear in the material when undergoing electrochemical cycling, which in turn eventually causes the electrode to disintegrate. Using SnS_2 this effect can be reduced significantly by the presence of sulfur atoms. These undergo a separate reaction with lithium, which will be described later in more detail, forming a protective matrix around the tin atoms, and thus holding them in place. Overall, this increases stability and improves cycle life.

SnS_2 has therefore enjoyed a high level of research interest in terms of its lithium ion storage properties. As it belongs to the group of inorganic fullerenes as previously mentioned, research groups were able to synthesise a large variety of different morphologies of this material and test them in lithium ion cells. A selection of various different morphologies is shown in Figure 1.11:

As can be seen from Table 1.6, SnS_2 is a promising material with very high possible discharge rates over a large number of cycles. It is the aim of this project to synthesise and characterise a novel morphology of SnS_2 (as introduced in Chapter 3) and add it to the long list of potential lithium ion battery electrode candidates.

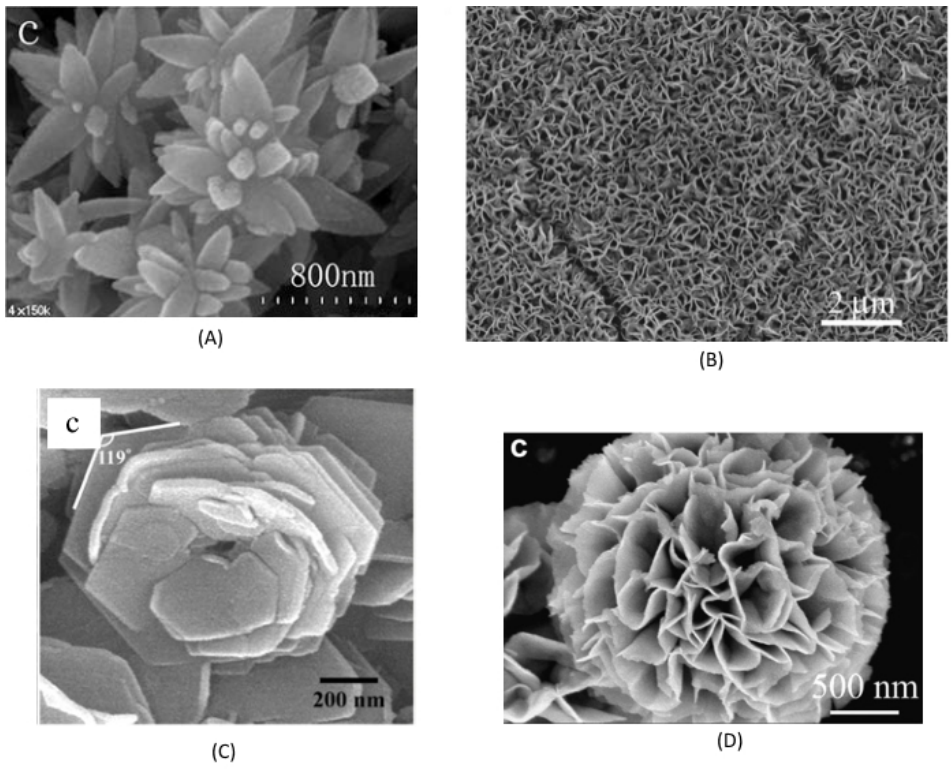

Figure 1.11: *A sample selection of SEM images depicting a few different nano-morphologies of SnS_2. (A) Aloe-like SnS_2, from [Zhu et al. [2006]]; (B) SnS_2 Nano-wall Arrays, from [Liu et al. [2010b]]; (C) SnS_2 Nano-flower, from [Shi et al. [2006a]]; (D) SnS_2 Nano-flower, from [Liu et al. [2010a]].*

Type of SnS_2 Morphology	Claimed Charge Capacity	Reference
Nano-flowers	502 mAh/g over 50 cycles	[Liu et al. [2010a]]
Nano-wall arrays	400 - 700 mAh/g over 40 cycles	[Liu et al. [2010b]]
Nano-rods	535.7 mAh/g over 25 cycles	[Wu et al. [2012]]
Nano-platelets	583 mAh/g over 30 cycles, 513 mAh/g over 50 cycles	[Zhai et al. [2011], Seo et al. [2008]]

Table 1.6: *A selection of various morphologies of SnS_2 as discussed in the literature and their charge capacities as a means of comparison between them all.*

1.2.3 The Use of Lithium Niobate as Lithium Ion Storage Material

Lithium niobate is not traditionally linked to lithium ion storage. It is mostly known for its properties in optical and electronic devices. It is a well-known optical waveguide [Tanzilli et al. [2001]], has piezoelectric properties [Weis and Gaylord [1985]] and can even be used as an explosion monitor [Bundy et al. [1990]]. However, only a few pieces of work exist on the material in terms of its lithium ion storage properties. In 2011, Pralong et al. [2011] published work showing that they manufactured a lithium niobate based electrode capable of reversibly intercalating lithium at a capacity of 130 mAh/g, which remains well below the performance of its competitors, and work as early as 1995 by Özer and Lampert [1995] showed that it was in fact possible to perform reversible lithium intercalation. Lithium niobate has, however, never enjoyed the rush of research as much as other materials such as silicon or graphite have in terms of its lithium intercalation properties. Similar to SnS_2, niobium sulfide forms layered structures with a sufficient layer spacing to allow lithium ion diffusion along the layers. Therefore, it seems promising to study a combination of the robust lithium niobate as a lithium ion reservoir with the layered niobium sulfide to provide increased lithium diffusion. This could result in enhanced charge/discharge (most notably cycle speed and electrode stability) properties of an electrode manufactured from this hybrid material. At the time of this writing, no previous work had been conducted on the synthesis and characterisation of a sulfidised lithium niobate hybrid material.

Chapter 2

Methodology and Techniques

2.1 Electron Microscopy

The structures under investigation in the course of this research project were of very small dimensions, usually in the range of several tens or hundreds of nanometres. Therefore, it was necessary to use electron microscopy to reveal these structures to the human eye and analyse them.

In conventional optical microscopes, as magnification is increased, point-like objects transform from sharp points into fuzzy disks surrounded by diffraction rings. These disks are referred to as Airy disks [Airy [1835]] and are the main restricting factor behind the limitation on resolution power of a microscope, which is defined as the ability of a microscope to distinguish between two close objects or structural features. A common way to express this is the maximum resolution d (minimal distance between two discernible points), which is dependent on the wavelength of the light used λ and the numerical aperture NA of the microscope, as described by Equation (2.1) [Fultz and Howe [2007]].

$$d \approx \frac{\lambda}{2 * NA} \tag{2.1}$$

When estimating d while using optical microscopes, the wavelength of the light used is usually 550 nm. The numerical aperture is dependent on the transmission medium and lies around 1.00 for air, 1.33 for water and 1.5 for oil [Cargille [1964]]. Thus, for conventional optical microscopes, the maximal resolution d is usually around the value of 200 nm. This limit of $d = 200$nm made optical microscopy inappropriate for the needs of the project, as the structures under investigation lay well below this range.[1]

[1]It needs to be noted, however, that several techniques exist to push the resolution of optical

Thus it became necessary to utilise other types of microscopy, electron microscopy in particular. These microscopes use beams of accelerated electrons as a means of illumination instead of visible light, and the wave characteristics of their electron beams is described by the de Broglie wavelength λ_e [Meschede [2010]]:

$$\lambda_e = \frac{h}{p_e} \tag{2.2}$$

$$= \frac{h}{\sqrt{2E_{mic}m_e}} \tag{2.3}$$

Here, h is the Planck's constant, E_{mic} is the kinetic energy of the accelerated electron and m_e is the electron mass. As the electrons in an electron microscope are commonly accelerated using potentials in the range of 80 to 400 kV, they reach relativistic speeds and thus an additional correction for these relativistic effects needs to be made:

$$\lambda_e = \frac{h}{p_e} \tag{2.4}$$

$$= \frac{h}{\sqrt{2E_{mic}m_0 * \left(1 + \frac{E_{mic}}{2m_0c^2}\right)}} \tag{2.5}$$

For 20 keV electrons, for example, the de Broglie wavelength is in the order of magnitude of 10^{-1} Ångstrom and is even smaller for higher accelerating voltages. However, the image resolution of electron microscopes is not only limited by aperture diffraction [Goldstein et al. [2003]], which is broadly described in analogy to Equation (2.1), but also by other factors, such as the imperfections of the electromagnetic lenses (aberrations) used in these microscopes, and which raise the resolution limit considerably (these are discussed in Section 2.1.1). As a consequence, for bulk objects an instrumental resolution is currently routinely quoted for commercial instruments in the order of 1 nm to 5 nm [Goldstein et al. [2003], Williams and Carter [2009]], whilst modern machines, such as the JEOL ARM200F at the University of Warwick, demonstrate resolutions in the sub-Ångstrom domain ($< 10^{-10}$ m) (see also [Max Planck Institute for Intelligent Systems [2014]]). This makes electron microscopy the tool of choice for the characterisation of the nano-structures. Three different types of electron microscopes were used during this project and will be

microscopes beyond this theoretical limit, but even with these techniques it was not possible to investigate the finer structures of the investigated particles. Therefore, these techniques will not be discussed here.

presented below.

2.1.1 Scanning Electron Microscopy (SEM)

The main tool of the investigation into the morphologies of the materials was the scanning electron microscope. This was due to the interest in investigating the topological properties of the nano-structures, as well as a necessity due to the size of the nano-particles making them hard to examine using transmission electron microscopy.

Set-up

The schematic of a SEM can be split up into several different stages, which are shown in Figure 2.1.

At the top of the microscope column sits the electron source. Three main types of electron sources are used in electron microscopes.

A tungsten hairpin filament is the simplest type of source. It consists of a single bent tungsten wire. If a strong potential is applied to this source, electrons are emitted thermionically from the tip of the bend, which can then be manipulated in further sections of the microscope to form the electron beam [Avadhanulu and Kshirsagar [1992], Goldstein et al. [2003]].

Another type of source uses lanthanum hexaboride (or more commonly, LaB_6) [Leung et al. [1984]]. It consists of a small, single crystal of lanthanum hexaboride with a sharp tip. Similarly to the tungsten filament, a high applied potential generates thermionic radiation of electrons from the tip of the crystal. While the process behind the emission is similar to the tungsten filament, the use of LaB_6 allows for a much brighter electron beam than using a tungsten filament (often by an order of magnitude, because of its lower work function, which allows for a higher electron emission at the same heating temperature [Goldstein et al. [2003]]) and a higher lifespan [Zhang et al. [2005]]. Nevertheless, the vacuum conditions necessary for operating a LaB_6 source are more demanding than those for the tungsten filaments.

The third type of source are called field emission guns [Otten and Coene [1993]]. Cold Field Emission guns [Crewe [1971]] are free of the disadvantages of the thermionic electron sources described so far, namely low brightness, limited lifetime and large electron energy spread and have a smaller source size [Goldstein et al. [2003]]. They are commonly fashioned out of a wire of single crystal tungsten, which has been sharpened to a tip with a diameter of 100nm or less. Due to this small

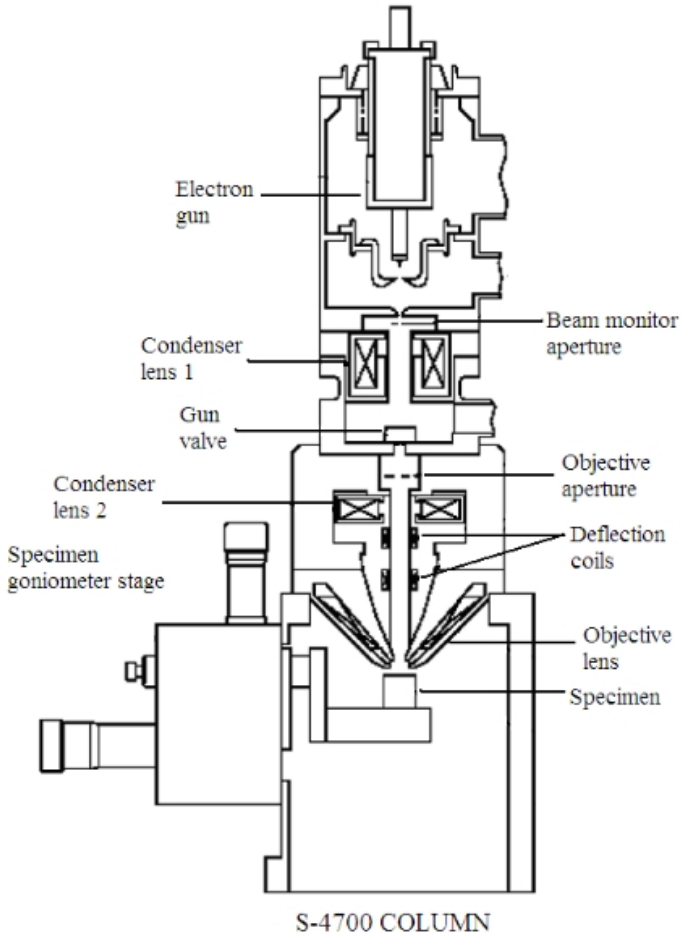

Figure 2.1: *A schematic diagram of the different elements making up a modern scanning electron microscope (SEM). From [Hafner [2007]]*

diameter, an applied electric field is focussed at the tip, which causes the emission of electrons via tunnelling without the need of any heating current. Hot-type, or Schottky-type, field emission guns exist as well [Tuggle and Swanson [1985]]. They are field assisted thermionic electron emitters and are fashioned by coating a thin tungsten wire with materials to enhance thermionic emission, such as zirconium oxide [Pawley [1997]], which increases electric conductivity at high temperatures. These field emission guns have somewhat larger source sizes and energy spreads than cold field emission guns, but they provide a greater stability of the beam current [Williams and Carter [2009]].

The emitted electrons then pass through the condenser lens system. These lenses are electromagnetic lenses and their purpose is the control of the beam size. This is done by passing the electron beam through the lens set-up, which often

consists of electromagnetic quadrupole [Grivet et al. [1972]] or hexapole [Reimer and Kohl [2008]] lenses. It demagnifies the source of the electrons via the interaction of the electrons with the surrounding fields to form a smaller spot on the specimen. The resulting electron beam spot on the specimen commonly has a diameter of 0.4 to 5 nm [Goldstein et al. [2003]].

The beam produced by these lenses then passes through the scanning stage. Here, the beam is shifted in such a fashion (raster fashion) that it covers the area of interest row for row at high speeds. This is typically done either by the use of a set of coils, which produce a magnetic field to induce the beam shift, or by a set of deflector plates, which shift the beam via an electric field. A final electromagnetic lens is used to focus the beam onto the sample and to contribute additional demagnification [Goldstein et al. [2003]].

Image Resolution

In scanning electron microscopes, the electron probe size d_p on a specimen depends as follows on various aberration effects [Goldstein et al. [2003], Williams and Carter [2009]]:

$$d_p^2 = d_G^2 + d_s^2 + d_d^2 \tag{2.6}$$

with:

- d_G is the aberration-free Gaussian diameter at the electron source;
- d_s is the diameter of the spherical aberration disk (caused by differences in magnetic fields seen by electrons along their respective trajectories closer to or farther away from the lens axis);
- d_d is the diameter of the aperture diffraction disk.

Aberration disks caused by astigmatism of the lenses due to rotational asymmetries perpendicular to their axes or by energy variations in the electron beam have been omitted from Equation (2.6), because they can be well controlled and suppressed.

The diameter of the aperture diffraction disk is described by [Goldstein et al. [2003]]:

$$d_d = 0.61 * \frac{\lambda}{\alpha} \tag{2.7}$$

where:

- λ is the de Broglie wavelength of beam electrons
- α is the beam convergence angle

Equation (2.7) corresponds in substance to Equation (2.1), which describes the resolution limit of visible-light microscopes.

From Equation (2.7) follows that the minimum electron probe size on a specimen is normally in the order of magnitude of 1 nm [Williams and Carter [2009]], which is clearly beyond the value for aperture diffraction alone, which, for 20 keV beam electrons, is in the order of magnitude of 10^{-2} nm.

Image Formation

When the electron beam hits the sample, two main types of interactions occur: elastic and inelastic scattering of electrons. Because of the energy of the incident beam, the electrons penetrate the sample, and these two types of processes do not only occur at the surface. The resulting volume of interaction between beam and specimen is often pear shaped, as shown in Figure 2.2.

The exact shape and size of this volume is dependent upon several factors:

- The energy of the incident beam electrons;
- The angle of the incident beam with the sample surface;
- The topology of the sample;
- The material making up the sample in terms of its composition and density;
- The change in trajectory through elastic interactions;
- The change in trajectory and/or energy loss through inelastic interactions.

Given a flat sample surface and an incident angle of 90°, the maximum depth and width of the penetration volume (see Figure 2.2) can be approximated as follows [Potts [1987]]:

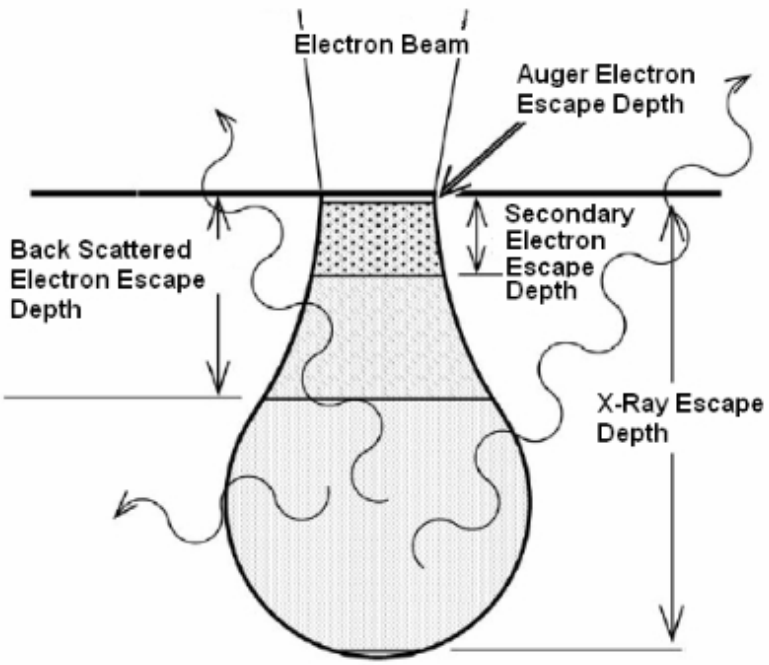

Figure 2.2: *A schematic of an interaction volume as encountered in SEM studies and an indication of the possible products of the interaction between electron beam and sample. From [Hafner [2007]]*

$$\Delta X_{depth} = \frac{0.1 E_{mic}^{1.5}}{\rho} \tag{2.8}$$

$$\Delta Y_{width} = \frac{0.077 E_{mic}^{1.5}}{\rho} \tag{2.9}$$

Here, E_{mic} is the kinetic energy (in keV) of the accelerated electrons and ρ is the material density in kg/m^3. ΔX_{depth} and ΔY_{width} are both in μm. The resultant excite volume has a truncated pear shape. The shapes can be approximated based on the calculation of individual electron trajectories using Monte Carlo simulations [Potts [1987], Joy [1991]].

Both interaction processes, elastic and inelastic scattering, produce a number of different signals that can be recorded using appropriate detectors.

During an elastic scattering process, the incident electron's kinetic energy remains unaltered while its trajectory changes. The primary signal that is produced this way is made up of so-called back-scattered electrons [Darlington [1975]]. These are created via an electromagnetic interaction between the incident electron and

the atomic nucleus. As the resulting energy of the electron is not different from its original energy, no other electrons are emitted. An approximation of the ratio between back-scattered and incident electrons can be formulated as in Equation (2.12) [Caceres-Valencia [2006], Love et al. [1978]]:

$$\eta_{b20} \approx -5.23791 * 10^{-3} + 1.5048371 * 10^{-2} Z - 1.67373 * 10^{-4} Z^2 + 7.16 * 10^{-7} Z^3 \tag{2.10}$$

$$A \approx -0.11128 + 3.0289 * 10^{-3} Z - 1.5498 * 10^{-5} Z^2 \tag{2.11}$$

$$\eta = \eta_{b20} * \left(1 + A * ln\left(\frac{E_0}{20}\right)\right) \tag{2.12}$$

Here, E_0 is the incident electron energy in keV and Z is the average atomic number of the sample, which can be simply calculated using Equation (2.13), where the index i corresponds to all present elements and Z_i and W_i correspond to the respective atomic numbers and relative weight fractions:

$$Z = \sum_{i=1}^{n} Z_i * W_i \tag{2.13}$$

Taking SnS_2 as an example, these equations produce, for an incident electron energy of 15 keV, the result:

$$Z = 0.3507 * 16 + 0.6493 * 50 = 38.0762 \tag{2.14}$$

$$A = -0.0184 \tag{2.15}$$

$$\eta_{b20} = 0.3634 \tag{2.16}$$

$$\eta = 0.3653 \tag{2.17}$$

Thus, in the case of SnS_2, roughly 37% of all incident electrons are back-scattered.

As can be seen, there is a dependence of the ratio of back-scattered electrons on the average atomic number of the sample. This results in an increased Z-contrast in the obtained image, which gives an indication of the distribution of elements within a sample. Care has to be taken though, as the number of back-scattered electrons can also be affected by the tilt angle of the surface relative to the incident beam. Greater tilt angles make the escaping of back-scattered electrons easier and thus produce a higher signal [Wittke [2008]].

Back-scattered electrons are collected in a special detector placed above the sample and around the incident electron beam (see Figure 2.1).

During inelastic scattering events, incident electrons interact with the electrons in the sample while experiencing loss of energy. These interactions can have a range of different results, such as the emission of electrons from the sample (secondary [Seiler [1983]] and Auger [Harris [1968]] electrons), the emission of photons (characteristic x-rays [Gabriel [1985]], cathodoluminescence [Steyn and Holt [1976]]) or simply a heating up of the sample [Vine and Einstein [1964]]. In this project, the main signals collected were emitted secondary electrons and emitted characteristic x-rays.

Secondary electrons are produced via the ejection of weakly bound electrons in the sample during the interaction with the incident electrons. Their emission is generally insensitive to the atomic number of the sample and their energy is lower than 50 eV. The energy distribution of the secondary electrons peaks at around 2-5 eV and around 90% of all secondary electrons are emitted with energies below 10 eV [Goldstein et al. [2003]]. Such low energies mean that emitted secondary electrons are quickly re-absorbed within the sample and their signal therefore only gives information about the top layers of a surface. For this reason, these electrons are a preferred tool when investigating surface properties of samples, where the signal of the bulk material might otherwise obscure the surface signal. As described above, for back-scattered electrons an increased tilt angle creates a stronger signal due to secondary electrons being able to escape the surface more easily.

In order to detect the emitted secondary electrons, an electron detector is placed near the sample facing the centre of the sample area under investigation. To attract a maximum amount of electrons, it is often equipped with a positively charged cage around the detector opening. This way, more electrons are guided into the detector. However, due to the placement of the detector, care has to be taken when evaluating the obtained images, as it now contains 'shadows' caused by surfaces facing the detector, which produce a higher brightness than surfaces facing away.

The interaction of the incident electron beam with the sample leads also to the emission of characteristic x-rays. These x-rays are produced when an incident electron interacts inelastically with a shell electron in an inner orbital of a sample atom within the exited volume at energy level E_0 and knocks it out of the atom. Another shell electron from a higher energy state E_1 then drops down to fill the position, and the energy lost this way is emitted in the form of a photon. This photon has an energy characteristic of the energy gap between the two energy states

of the shell electron, which in turn is characteristic of the element the sample atom belongs to (see Figure 2.3) [Potts [1987]]:

$$E_{x-ray} = |(E_1 - E_0)| \tag{2.18}$$

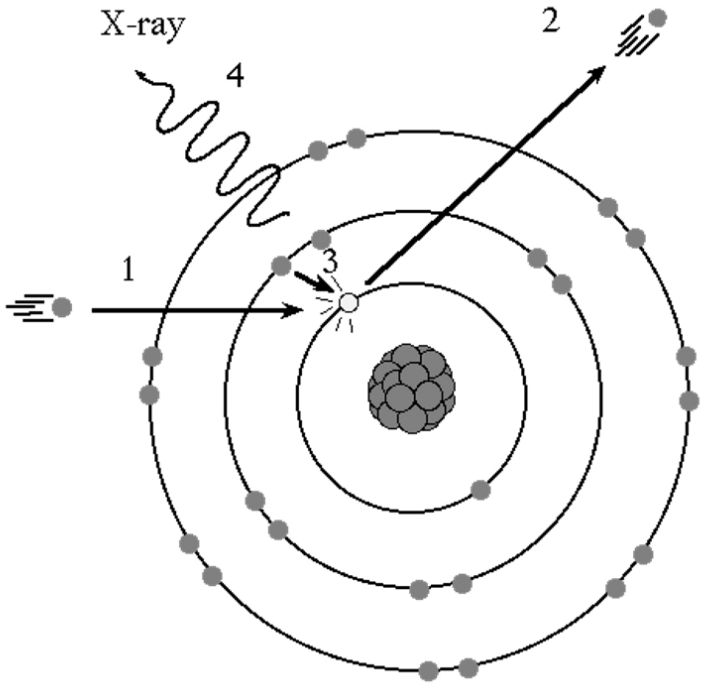

Figure 2.3: *An incident electron interacts with a shell electron (1), ejecting it from the atom (2). A higher-energy shell electron then drops down to fill the lower energy state (3) under the emission of an x-ray (4). From [Disher et al. [2006]]*

By collecting a large number of characteristic x-rays produced this way, a spectrum of the sample can be obtained and used to determine which elements are present and, by further analysis, in what relative ratios [Goldstein et al. [1977]]. However, the emission of these x-rays is a relatively inefficient one. Most interactions occur between the incident electron beam and electrons in outer orbitals of atoms making up the sample. As a result of the deceleration of primary beam electrons due to interactions with the electric fields created by these outer orbital electrons, a continuous x-ray spectrum is generated which superimposes the characteristic x-ray lines of the sample (see 2.4) [Potts [1987]].

This technique is used to perform quantitative chemical analysis of specimens

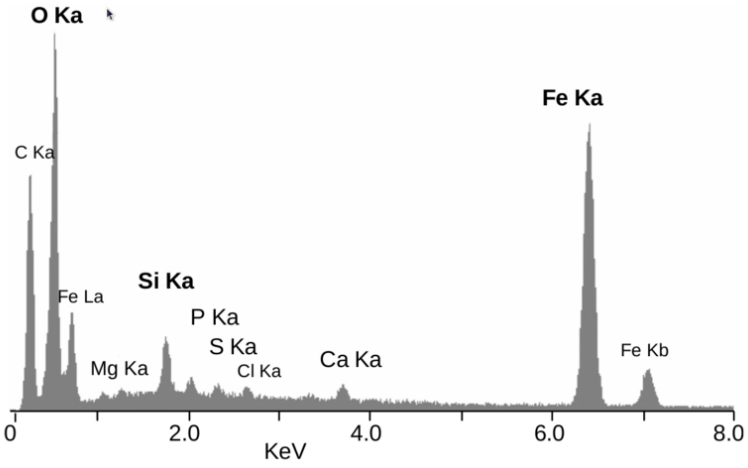

Figure 2.4: *EDS spectrum of the mineral crust of the vent shrimp Rimicaris exoculata. It shows peaks caused by X-rays given off as electrons return to the K electron shell and one peak resulting from the L shell of iron. From [Corbari et al. [2008]]*

and is commonly referred to as Energy-Dispersive X-Ray Spectroscopy (commonly abbreviated as EDXS, EDS, EDX or EDAX).

X-ray detection is commonly done using two main types of detectors. Each detector needs to be fitted externally to the microscope and can be inserted into the sample chamber when necessary. Solid state detectors (SSD) [Klug and Alexander [1974]] are based on electron-hole pair generation in semiconductors contributing to an electrical current proportional to the energy deposited in the semiconductor crystal. The classical detectors are based on lithium doped germanium (Ge(Li)) or silicon (Si(Li)) crystals, which have to be cooled down to $-196°C$ using liquid nitrogen for low signal-to-noise ratios and suppression of Li diffusion, which would destroy the detectors [Beckhoff et al. [2006]; Grupen and Buvat [2012]]. A newer generation of detectors are the so-called silicon drift detectors (SDD) [Lechner et al. [2001]]. These detectors use high-purity silicon, which allows for easy Peltier-based cooling to about $-20°C$ as opposed to the expensive and inconvenient use of liquid nitrogen cooling for Ge(Li) and Si(Li) detectors [Williams and Carter [2009]]. As each incident x-ray hits the detector and causes ionisation, an electric field generated by a set of ring electrodes cause the charge carriers to drift to the respective electrodes. This technology allows for higher count rates and better energy resolutions when compared to standard SSDs.

The actual collected image is produced by moving the electron beam across the sample in a raster fashion at high speeds. Thus, each image is a collection of data

points obtained from subsections of the sample area. Back-scattered and secondary electrons can be used to create electron images in such a way that they give a strong indication of the properties of the uppermost surface areas in the sample and thus are ideal for determining topological properties. Characteristic x-rays can be collected to produce an average sample spectrum and give an indication of the elemental set-up of the investigated sample section. Nevertheless, because of the scanning nature of the microscope, it is also possible to use the individual spectra of each data point to create elemental maps indicating the location of each element in the sample. This is particularly useful to determine elemental distributions (see Figure 2.5).

As regards, the accuracy of compositional analyses based on Energy-Dispersive X-Ray Spectroscopy, it should be kept in mind that the x-rays collected by the detectors are emitted from large parts of the electron excited volume which is pear shaped and has a diameter between 0.1 and 2 μm (for further details see above). The spatial resolution is thus somewhat limited. Other factors potentially influencing the accuracy of the compositional analyses are secondary x-ray fluorescence induced in the sample by the characteristic x-rays, partial overlap of x-ray lines, x-ray absorption in the sample, the take-off angle between the surface of the sample and the spectrometer entrance slits (or collimator), and specimen tilt [Potts [1987]].

Sample Preparation

Due to the penetration of incident electron beams (the maximum penetration depth is described above by Equation (2.9)), scanning electron microscopes permit the observation and characterization of heterogeneous organic and inorganic materials on a nanometre to micrometre range [Caceres-Valencia [2006]]. Depending on the concrete examination undertaken, secondary or backscattered electrons or characteristic x-rays used for image formation do, strictly speaking, not only rise from the sample surface but could have been emitted from parts of the interaction volume up to a few micrometers below the surface. However, scanning electron microscopy does not rely on the transmission of electrons through the sample. Thus, no special care needs to be taken in order to ensure a sufficiently thin sample. In practice, it is even possible to image samples of significant thickness, as the SEM is a mainly surface-orientated technique due to the low electron penetration depths caused by a low accelerating voltage.

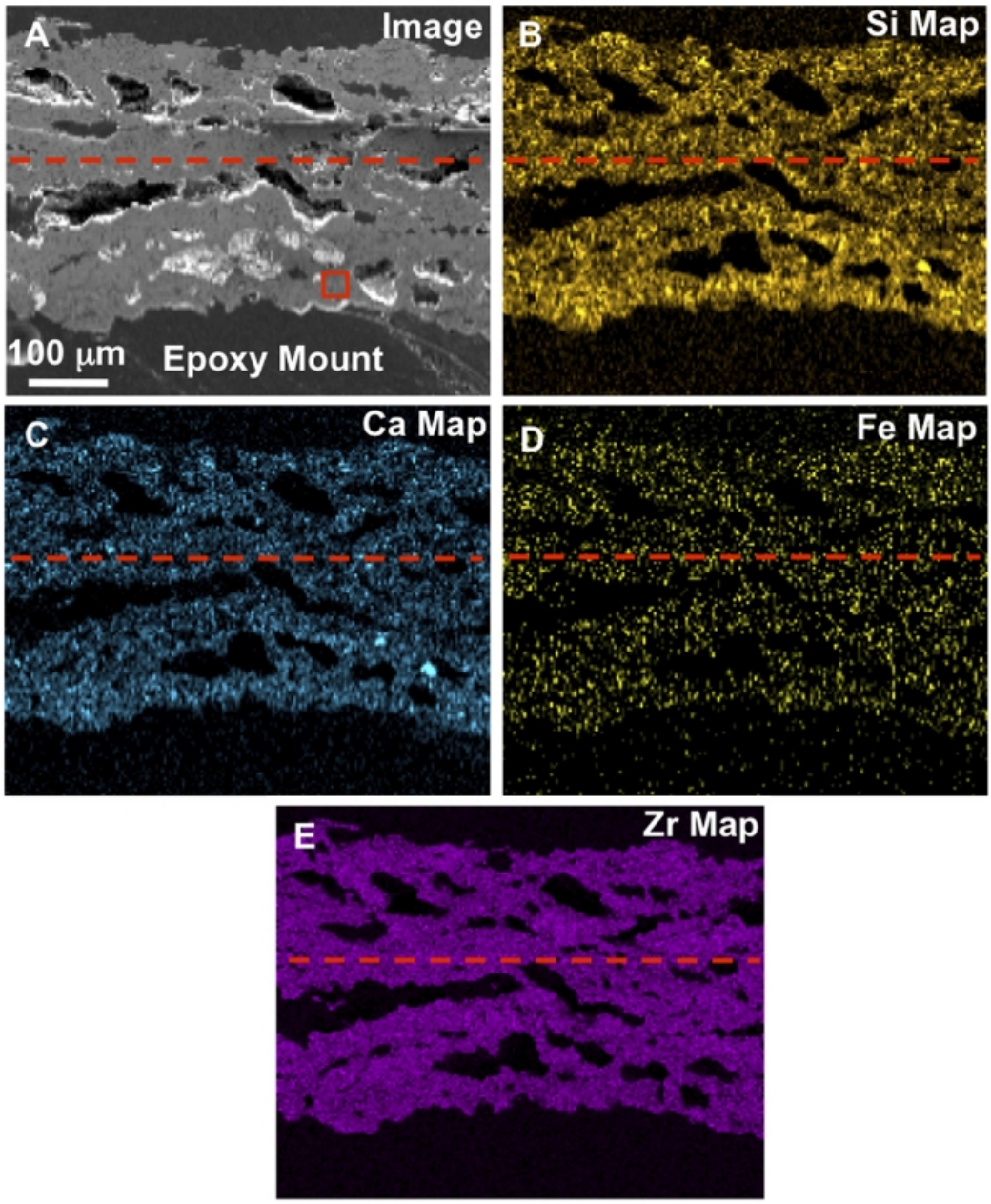

Figure 2.5: *A sample for a set of elemental maps obtained via energy dispersive x-ray spectroscopy (EDX). The individual maps can be compared to the secondary electron image to determine the composition of different structures in the image. From [Gledhill et al. [2011]]*

Several factors do need to be taken into account with sample preparation however. First, sample robustness needs to be determined. While most inorganic

samples are relatively stable under the electron beam, some fine structured samples or biological samples are known to degrade rapidly when placed under a constant stream of electrons [Thach and Thach [1971]]. One way to avoid this is to cool the sample using a cryo-system, which often uses liquid nitrogen to lower the temperature of the sample and thus limits the damage caused by heating under the beam [Knapek and Dubochet [1980]]. Fortunately, the synthesised samples were sufficiently stable to allow standard, non-cryo investigations to take place.

Second, as the sample chamber inside the SEM is kept at a very high vacuum of about 10^{-4} Pa or 10^{-6} torr [Goldstein et al. [2003]], it is necessary to ensure the sample is sufficiently free of volatile substances. If small amounts of these volatile substances, such as water or other solvents, remain in the sample, they can get trapped in little bubbles or fractures within the sample. Once the pumping mechanism for the vacuum sets in, this causes a drastic expansion of these materials as they evaporate, which can lead to significant damage to the sample itself. Furthermore, through this process the sample chamber inside the SEM can get contaminated.

Third, as the sample is exposed to the electron beam, a significant amount of electrons can be absorbed by the sample, depending on the conduction properties of the exposed material. This could cause a negative charging of the sample, which could have two major effects. On the one hand, inhomogeneous charging in a fragile sample may cause damage to the sample by electrostatic repulsion [Egerton et al. [2004]]. On the other hand, as the SEM relies on electrons to form images, strong negative fields in the sample can cause electrons to be diverted and knocked off trajectory, which in turn leads to distorted images. One way to address this issue is to allow electrons to drain away from the sample once they have been absorbed. This is done by mounting the sample on a conductive stub as a standard procedure. While this works sufficiently well for conducting samples, insulating samples will still accumulate charge. In these cases it is necessary to coat the sample with a thin conductive film. Commonly, a thin gold film is used for this because of its ability to create thin and homogeneous films [Brunk et al. [1981]]. However, should the sample to be examined contain gold, other materials need to be used such as palladium or carbon (see Figure 2.6).

For the purpose of samples produced during this project, it was fortunate that these all had semiconducting properties and were stable under electron beams, and thus didn't need to be cooled or coated. However, the work conducted on SnS_2 in particular showed a great ability of the material to retain liquid solvents and therefore more elaborate drying processes were required. It proved sufficient to dry the samples at elevated temperatures in vacuum, but this will be discussed in more

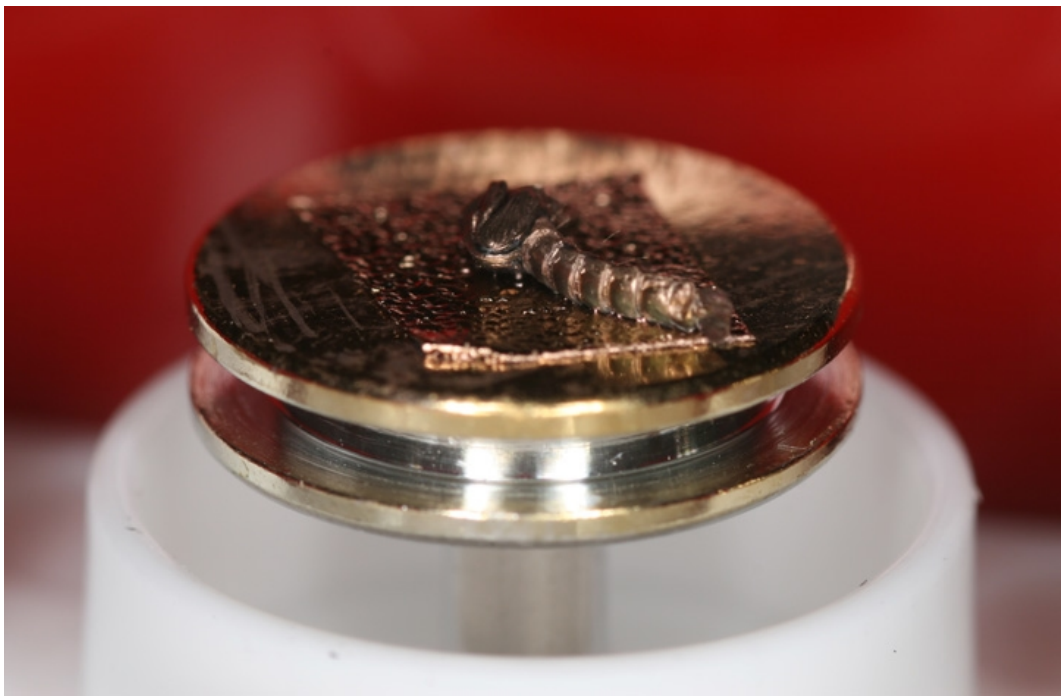

Figure 2.6: *A sample prepared for SEM analysis. The figure shows a biological sample, a mosquito larvae, mounted on a standard SEM aluminium sample stub and coated with gold for enhanced surface conductivity. From [Kinsman [2008]]*

detail in Chapter 3.

2.1.2 Transmission Electron Microscopy (TEM)

Set-up

As shown for the SEM above, a diagram of a TEM can be seen in Figure 2.7.

The set-up of the TEM is very similar to that of the SEM up to the specimen stage. The electron source is located at the top of the column. As with the SEM, this source can be one of the three previously mentioned, so either a tungsten filament [Avadhanulu and Kshirsagar [1992]], a LaB_6 crystal [Leung et al. [1984]] or hot- or cold-FEG (field emission gun) [Tuggle and Swanson [1985]; Crewe [1971]]. Practically though, as the TEMs are high precision instruments, they are often equipped with advanced electron sources and therefore usually use a FEG or LaB_6 electron source.

The lensing system in a TEM, mounted between the electron gun and the sample, contains condenser and objective lenses similar to the SEM. These lenses use magnetic fields to create a lens for the emitted electrons from the electron

source with the purpose of controlling the size of the electron beam and to focus it onto the sample, whilst demagnifying its spot size. This is usually done with the before-mentioned quadrupole and hexapole lenses. A new lens system for the TEM as compared to the SEM consists of the lenses mounted in flight direction of the electron beam behind the specimen on the sample holder. The lens system comprises an objective lens, potentially one or several intermediate lenses and a projector lens and has the purpose of magnifying and focusing the image formed from the electrons transmitted through the sample on the imaging system (see Figure 2.10) [Williams and Carter [2009]] .

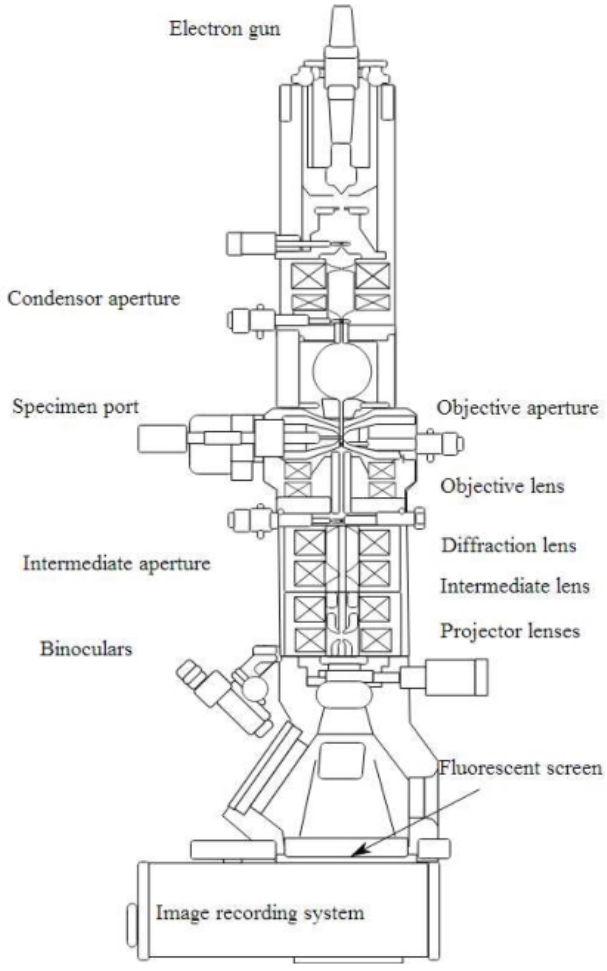

Figure 2.7: *A schematic of a transmission electron microscope (TEM) containing all essential elements. Modern TEMs are often further equipped with advanced aberration correctors, which are also fitted into the microscope column. From [White [2014]]*

The imaging system for the TEM is either a viewing screen that allows a direct observation of the image by eye, or a charge-coupled device (CCD) system to allow digital capture and manipulation of the image. In the case of the viewing screen, this is usually done using a phosphor screen, which converts incident electrons into photons. It is necessary to use a phosphor coating that allows for a high conversion efficiency, short decay times and good spatial resolution in order to allow for a smooth operation of the microscope. The digital option uses a special CCD system that enables the recording of the beam of electrons and a subsequent conversion of this signal into a digital image. The quality of the CCD system is a direct factor affecting the image quality and has been a focus of recent innovations [Janesick [2001]].

The specimen mounting system inside a TEM is significantly different compared to that in the SEM. Unlike with the SEM, the TEM column is under constant vacuum, and sample loading therefore has to be done via a system of valves in order to maintain the purity of the vacuum. The material specimen is dispersed onto a small, circular metallic grid. Commonly, copper is used as a base metal for the grid, but other grids made from gold, molybdenum, platinum and more exotic metals are also used. TEM grids come in different mesh sizes, which can be adjusted to accommodate the needs for the specific specimen under investigation. Often, these grids will have an additional coating to improve imaging conditions, such as amorphous carbon films. The specimen holder itself can usually accommodate one or two grids at a given time. The holders range from simple hold-in-place systems to single- or double-tilt holders, which allow a rotation of the sample inside the microscope column.

A final part of the TEM are its apertures, of which there are commonly three: the condenser aperture, the objective aperture and the selected-area aperture. While the condenser aperture is fixed in place and can only be adjusted in terms of its diameter, objective and selected-area apertures can either be inserted or removed from the beam path. The apertures consist of a hole in a metal disk, which is thick enough to prevent transmission of electrons anywhere other than the aperture hole. This has two main effects. First, the exclusion of electrons lowers the overall beam intensity after the aperture. Samples that are particularly sensitive to high beam dosages can benefit from this. Second, by only allowing central electrons to pass, it is possible to filter out unwanted electrons. These include electrons that are scattered to high angles caused by unwanted processes such as spherical or chromatic aberration or due to diffraction processes within the sample [Reimer and Kohl [2008]].

Aberrations and Correctors

Whenever light passes through a lens, imperfections in the lens can create aberrations in the transmitted beam. Electron beams are similarly affected by aberrations when they pass through electromagnetic lenses. As no electromagnetic lens is perfect, a number of aberrations are well known to electron microscopists, such as spherical and chromatic aberration and (two-fold) astigmatism. However, other forms of aberrations are also known such as comatic, star and three-lobe aberration, and three- and six-fold astigmatism. Spherical and chromatic aberration and astigmatism are considered standard defects of illumination system lenses and are discussed in more detail below [Williams and Carter [2009]].

The most common, and easiest to correct, type of aberration is the so-called astigmatism. Under optimal imaging conditions, the incident electron beam has a circular cross-section. However, a variation in this shape to a ellipsoid cross-section causes problems when attempting to correctly focus the image. In severe cases of astigmatism, the image, even at optimal focus, appears to be pulled along one direction. This aberration can be corrected by using a stigmator, which is a set of electromagnetic coils that enable a tuning of the electron beam cross-section via the application of a magnetic field. Using this, the beam can be forced to take a circular cross-section again by adjusting this field.

A different type of aberration is called chromatic aberration. In optical microscopy, this aberration is caused by a lens system failing to focus light of different wavelengths to the same focal point. For example, this can mean that all green light elements are in focus while all red light elements are out of focus and vice versa. In electron microscopy a similar effect occurs. Here, elements of the electron beam with different energies have slightly different focal points. The easiest way to minimise chromatic aberration effects is to minimise the spread of electron energies of the incident beam. This type of corrector is called a monochromator and it operates by only allowing electrons within a small energy window to pass (in the range of 0.1 eV). The drawback to this is that by doing so, the beam intensity drops significantly due to the diminished amount of electrons permitted to pass. A second type of correction can be used by placing an imaging energy filter designed to exclude inelastically scattered electrons and only permitting zero-loss electrons to pass.

As a beam passes through a lens, the ideal case would allow for all rays that pass through the lens to be focussed onto the same point. However, in reality, rays that pass through the lens off-centre are bent to focus either before (positive spherical aberration) or after (negative spherical aberration) the theoretical focal

point. The same holds true for electron beams and electromagnetic lenses. The way to correct for this is to include special corrector lens systems with negative spherical aberration to counter the positive spherical aberration of the objective lens, thus reducing the total spherical aberration to near zero.

Image Formation

Bright Field

As the electrons pass through the sample, the TEM image contrast is formed because of the interaction of the incident beam within the specimen, giving rise to changes in both the amplitude (mass-thickness and diffraction contrast) and phase of the electron wave (phase contrast). In a sense, the image thus formed corresponds to a two-dimensional projection of the sample.

In TEM bright field (BF) mode, the most common method of TEM imaging, an aperture is placed behind the objective lens which allows only the directly transmitted beam to pass. As the direct beam is weakened by scattering, diffraction and absorption within the sample and the scattered and diffracted electrons are hindered by the objective aperture to contribute to the image, thicker or denser regions of the sample, or regions containing atoms with higher atomic numbers, appear darker in the resulting image, than regions with thinner or less dense material or with elements of lower atomic numbers (see Figure 2.8) [Williams and Carter [2009]]. The difference between BF image and diffraction pattern mode will be explained in more detail below.

Diffraction Contrast and Dark Field

As with bright field imaging above, the sample is placed in the incident electron beam, which is weakened inside the sample by scattering and absorption (in crystalline parts of the specimen, Bragg diffraction of the electrons contributes to that too). In the case of dark field imaging, however, the directly transmitted beam does not contribute to the image, only the scattered and diffracted electrons. This is achieved by tilting the incident electron beam against the optic axis and adjusting the objective aperture to selectively exclude the direct beam (see Figure 2.9). This imaging technique is called Centered Dark Field imaging (DF or CDF, sometimes also called On-axis DF) and the images obtained only contain information from those parts of the samples which contributed to the scattering and diffraction of the incident electrons. In BF mode, areas of the sample that are thicker or contain material of a higher mass show up darker, while thinner or lower-mass areas show

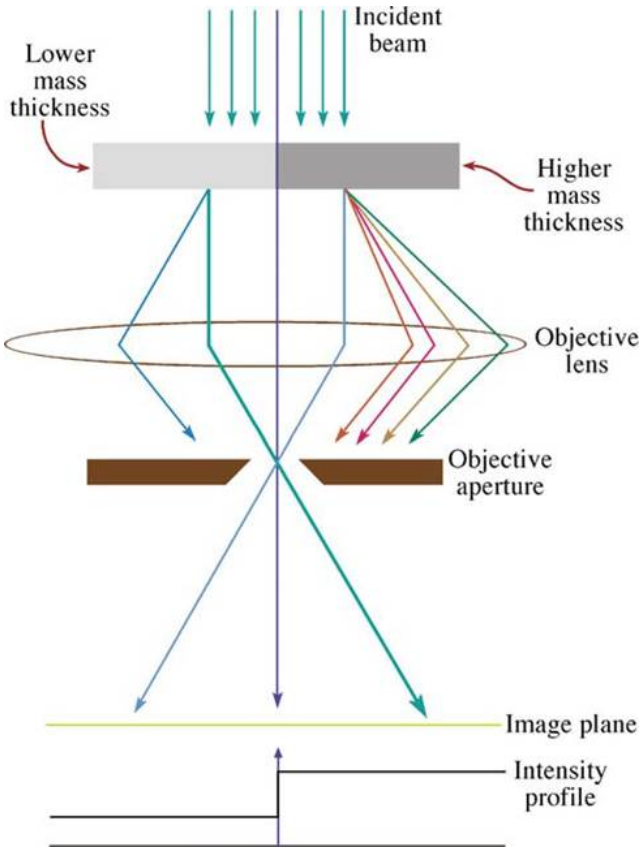

Figure 2.8: *Formation of mass-thickness contrast in BF images. Thicker, denser or areas with higher atomic mass numbers are scattering more electrons off the incident electron beam, thus, due to the use of the presence of the objective aperture, leading to fewer electrons falling onto the equivalent area of the image plane/screen. As a consequence, these areas appear darker in BF images. From [Williams and Carter [2009]].*

up brighter. In dark field mode, the reverse is true (see Figure 2.9) [Williams and Carter [2009]].

Another imaging technique to produce DF images consists in using a non-tilted incident electron beam in combination with an off-axis objective aperture for producing images to which only scattered electrons contribute (Displaced-Aperture or Off-axis DF). Due to the technically more demanding use of off-axis electrons, DADF is much less widely used than CDF and, thus, not explained here in more detail [Williams and Carter [2009]].

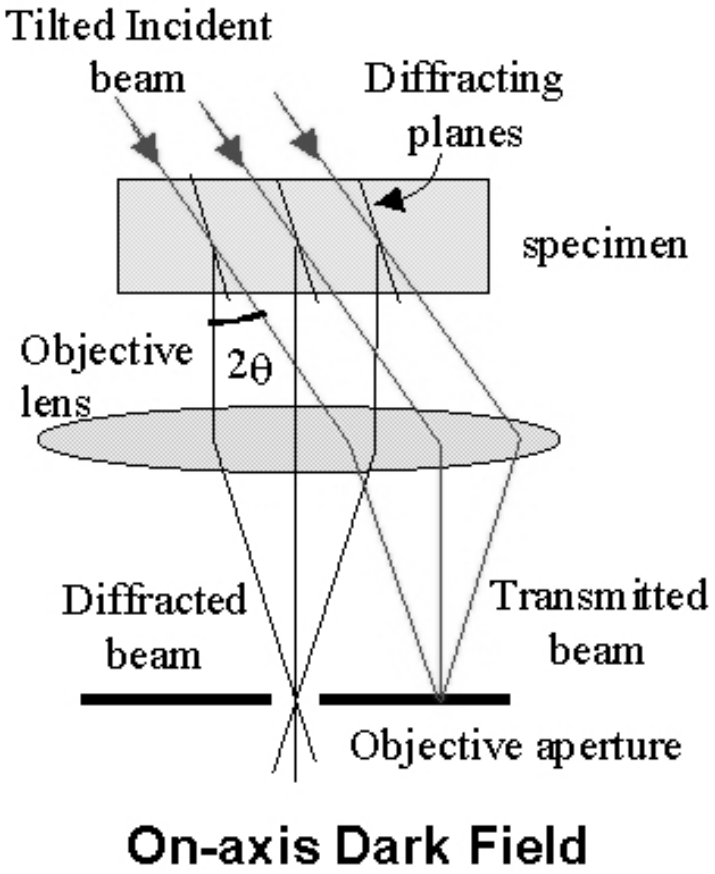

Figure 2.9: *Ray diagram showing the use of tilt, objective lens and objective aperture in combination to produce on-axis DF images. From [Kanellopoulos [2011]]*

Phase Contrast or High-Resolution TEM

As already described above, when incident electrons pass through a sample, they interact with the atoms in the specimen. Each electron is considered as a planar electron wave incident on the sample, whose wave amplitude and phase is changed due to the interactions taking place, causing constructive or destructive interference. The resulting electron exit-wave is a combination of the various Bragg-diffracted waves and the transmitted plane wave. The wave is collected by the objective lens and focused on the image acquisition system of the microscope. For achieving a high resolution, not only the direct beam must be allowed to contribute to the image, but also the diffracted ones. As a consequence, no or only a rather large objective aperture is used in HR TEMs. The contrast mechanism, described by a so-called phase contrast transfer function (CTF), is very sensitive to many factors, including the focus and astigmatism of the objective lens. Through an appropriate choice

of negative defocus of the lens, the so-called Lichte Defocus, the point resolution of the method can be optimized. Its value is usually negative and in the order of magnitude of several hundred nanometers [Lichte [1991]].

An image obtained by phase contrast imaging is not simply dependent on the number of collected electrons in the image acquisition system, and it does not constitute a direct representation of the sample, which could be directly interpreted by eye. However, the data can be used, based on a number of assumptions, to reconstruct the respective exit-wave and thus obtain, in a trial and error approach, in the end a very high resolution image of the probable crystal structure of the sample material. In practice, such a reconstruction is done, based on a through-focus series of images taken around the Lichte Defocus [Lichte [1991], Williams and Carter [2009]]. As exit wave reconstruction was not included in this project, it will not be further described here.

High-resolution phase-contrast imaging is one of the highest resolution techniques developed so far and allows for resolutions of below 0.1 nm, even if the images have to be interpreted. The technique enables the direct viewing of columns of atoms in crystalline sample material [Williams and Carter [2009]].

Electron Diffraction

The two principle modes of operation of TEM imaging systems are the image and diffraction modes. All electron rays originating from the same point in the sample and emerging from the exit surface are gathered by the objective lens and focused onto the same point in the image plane of the lens, which thus contains an image of the illuminated area of the sample. At the same time, the objective lens focuses all rays, which are leaving the sample in the same direction, onto the same point in the back focal plane of the lens, where these points form an image of the diffraction pattern of the sample (see Figure 2.10). In diffraction mode, the diffraction pattern (DP) in the back focal plane of the objective lens is projected by subsequent intermediate and projector lenses onto the viewing screen (final image plane). In image mode, the same lens system projects, instead of the diffraction pattern in the back focal plane, the image in the image plane of the objective lens onto the screen [Williams and Carter [2009]].

In TEM diffraction mode, for single crystals this produces a pattern of bright dots, which is dependent on both the overall structure of the crystal and its current orientation under the beam. By analyzing the observed pattern, it is possible to make deductions about the space group symmetries of the crystal structure and its orientation. This necessitates, however, converging the normally used parallel

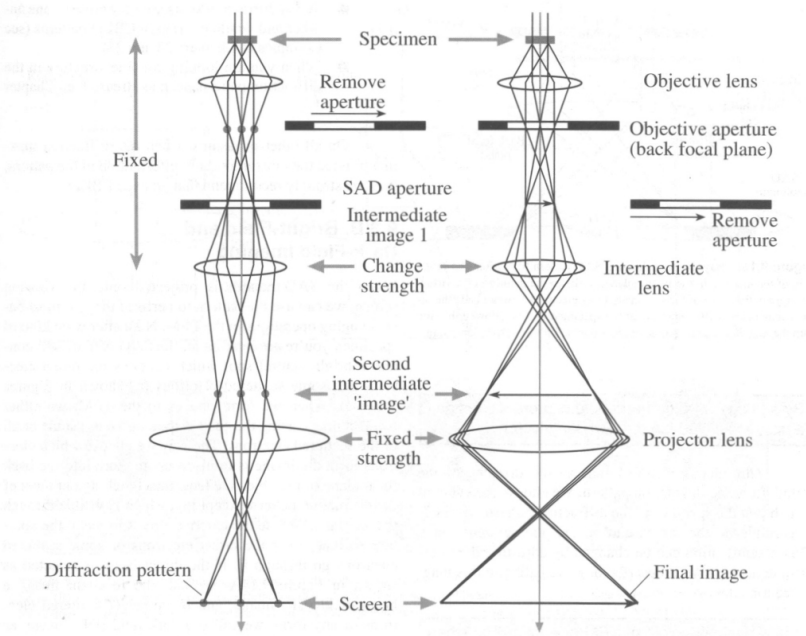

Figure 2.10: *The two basic operating modes of the TEM imaging system: image mode (right) and diffraction mode (left). From [Williams and Carter [2009]]*

incident electron beam into a well-focused probe, a technique called convergent beam electron diffraction (CBED). In the case of multiple crystals in the diffraction area, the diffraction pattern loses its dot-like pattern and smears out into a more complex structure, comprising also sets of concentric rings instead [Williams and Carter [2009]].

Electron Tomography

When taking an electron image, a flattened 2D projection of the 3D sample is produced perpendicular to the incident beam. While this can already give valuable structural information, complex structures remain difficult to interpret. However, by using a single- or double-tilt sample holder, it is possible to tilt the sample by a set amount and take another image. If this is done in set intervals across the tilt range, a series of 2D projections at different angles throughout the sample can be collected. By using image reconstruction software it is possible to combine these images to draw conclusions about the structure of the sample and create a 3D reconstruction, thus regaining depth information lost when taking 2D projections from the 3D sample (see Figure 2.11). This is, however, only possible for features showing mass-thickness or diffraction contrast. The technique does not work using phase-contrast imaging,

because specimen tilting changes the phase contrast [Williams and Carter [2009]].

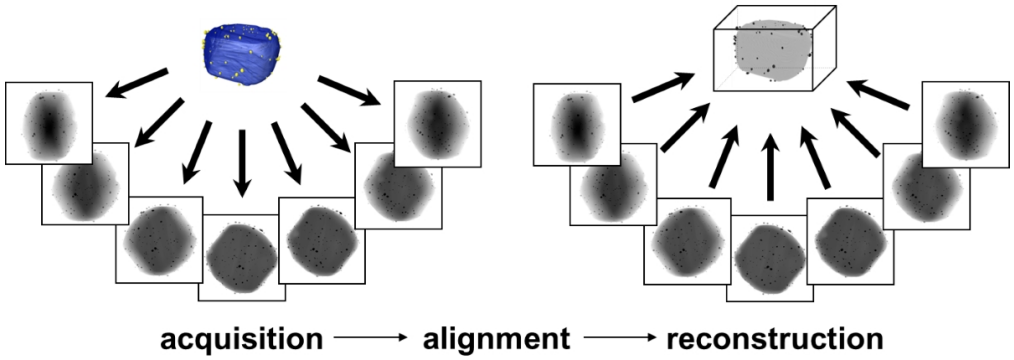

Figure 2.11: *A schematic representation of the imaging and reconstruction process when using the electron tomography technique. From [Kübel et al. [2010]]*

It needs to be noted that a full reconstruction requires a full tilt range from $+90°$ to $-90°$. However, due to the spatial restrictions of the sample, this is not possible. A good tilt sample holder can reach tilt ranges from around $+70°$ to $-70°$, which leaves a wedge of the structure unavailable for reconstruction. By using a double-tilt holder, the size of this wedge can be further reduced, but a small, non-imaged volume of the sample still remains. Nevertheless, it is possible to use data obtained from the rest of the structure to make deductions about the missing section and produce an approximated total reconstruction.

For a successful 3D reconstruction, the projection images must be true projections of the structure and its characteristics to be analysed (this excludes, as already mentioned above, the use of phase-contrast images), the tilt-series has to be very well aligned, so that the differences between the recorded images correspond only to the tilting around a well-specified axis. In practice, therefore, the images in a tilt-series need to be realigned properly before starting the 3D reconstruction. This can be best achieved by using characteristic markers. Regarding the numerical reconstruction, attention has to be paid not to oversample and care has to be paid not to overemphasize certain characteristics to the detriment of others (for example low spatial frequencies when using Fourrier sampling can be corrected when using algorithms such as Filtered Back-Projection (FBP) or Weighted Back-Projection (WBPJ)). Nowadays, the Simultaneous Iterative Reconstruction Technique (SIRT) is a preferred choice for this purpose [Kübel et al. [2010]].

As was shown, BF-TEM tomography for example is suitable for amorphous samples, where contrast due to mass-thickness is dominant. For crystalline mate-

rials, where images are strongly influenced by diffraction contrast, it is less suited. Comparable limitations exist also for other TEM-based techniques, which do not always meet the projection requirement, that a recorded signal must be a monotonic function of the contrast-raising physical properties of the sample. Progress was made in this respect by resorting to Incoherent Bright Field STEM tomography (IBF-STEM), where the HAADF-STEM technique allows to suppress diffraction contrast in the images recorded (for further details regarding STEM and HAADF, see below) [Li et al. [2013]].

Sample Preparation

As described in a previous section, samples for the TEM are mounted on small circular grids or sample holders. For fine particles, grids or meshes are preferred because of the bigger retention of sample matter. These meshes can be scaled to suit the sample material and are commonly covered with an additional coating to further improve sample retention. For this purpose, various forms of carbon support films have been developed, of which amorphous carbon films, lacey carbon films, graphene oxide or graphene are common candidates (see Figure 2.12).

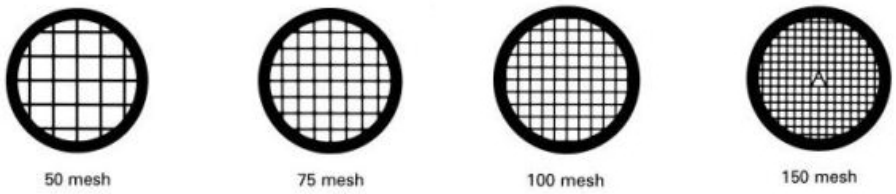

Figure 2.12: *A set of TEM support grids. The grids come in different mesh sizes, the higher the mesh number, the tighter the mesh. From [Agar Scientific [2014]]*

Should the sample be made out of larger, solid constructs, as is the case for much of the semiconductor research, the sample needs to be sufficiently thinned down to allow penetration of the electron beam and must be mounted on special sample holders. For specimen preparation from nano-powders, as was the case for the synthesised materials, a small amount of the powder is dispersed in ethanol and deposited drop-by-drop onto the grid. Care has to be taken not to over- or under-load the grid. The grid was then dried to ensure the removal of all volatile contaminants and placed in a designated sample holder (as previously discussed for the preparation of SEM samples).

2.1.3 Scanning Transmission Electron Microscopy

Experimental Set-up

It is possible to combine the properties of the scanning electron microscope with those of the transmission electron microscope. The result is the scanning transmission electron microscope, which, in principle, works the same way as a standard transmission electron microscope.

The electron beam is generated using an electron source as described in the last section. It is subsequently condensed using a condenser lens system and subjected to any installed corrector systems. Instead of passing a broad beam straight through the sample, as is the case for TEMs, the beam is focussed into a spot on the sample. The spot is then moved across the sample in a raster fashion, similar to the operation of a SEM. This is achieved using a series of electrostatic deflectors above and below the sample, which first scan the beam across the sample and then return the beam to its initial central-beam state. The signal (the transmitted electrons) is subsequently collected by an electron detector, which translates the image into an electron image (see Figure 2.13).

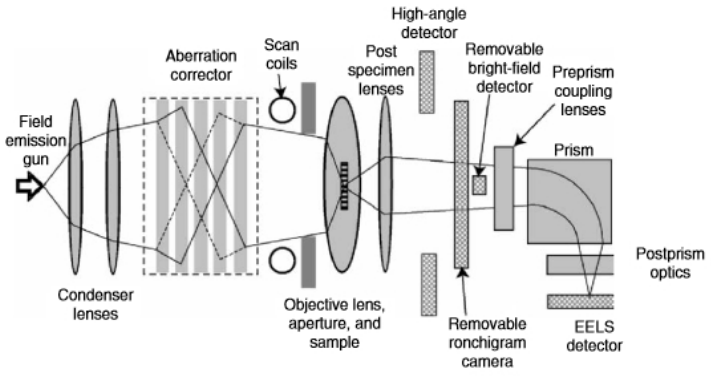

Figure 2.13: *A cut-out section of a scanning transmission electron microscope showing its main features, including correctors and various detectors, such as High-Angle Annular Dark Field (HAADF), Dark Field (DF), Bright Field (BF) and Electron Energy-Loss Spectroscopy (EELS). From [Pennycook et al. [2007]]*

Image Formation

While several different types of signals can be obtained via STEM, only the four most commonly used techniques will be discussed: Bright Field, Dark Field and Characteristic X-Rays.

Bright Field (BF) Imaging

Bright field imaging in a STEM works very similar to bright field imaging in the TEM. The beam is directed onto the sample, but while the entire parallel beam passes through the sample and is collected to form the image in the TEM, the beam is focussed down into a point probe during STEM BF mode, which is then raster-scanned over the sample and collected after transmission to form an image pixel by pixel. The detector sits, as can be seen in Figure 2.13, on the central axis of the electron column below the sample.

Annular Dark Field (ADF) Imaging

Dark field imaging in the STEM makes use of an electron detector, which has an annular shape. This detector is placed down-beam from the sample and is placed around the axis of the main beam. This allows for the collection of the scattered electrons within the capture angle of the detector (however, not all scattered electrons fall within that angle, depending for example on camera length (distance between detector and specimen) and convergence angle of the incident beam [Williams and Carter [2009]]), while still permitting the central beam to pass. This stands in contrast to dark field imaging in the TEM, which uses apertures to selectively permit only certain Bragg scattered beams to pass. By using this dark field set-up in the STEM, it is possible to conduct dark field imaging simultaneous to other techniques, such as EDX, bright field imaging or electron energy-loss spectroscopy (EELS). Bright and dark field images recorded from the same area are shown in Figure 2.14 (and also in Figure 3.15 in Chapter 3).

Standard annular dark field detectors which collect both coherently and incoherently scattered electrons, even if the amount of coherently scattered electrons depends for example on camera length. For example in case of very small camera length, mainly incoherently scattered electrons are being collected by the ADF detectors, so that the resulting image mainly depends on the chemical composition of the sample (Z-Contrast) [Williams and Carter [2009]]. In addition to the standard annular dark field detectors, it is possible to build detectors that only collect incoherently scattered electrons. These are scattered at higher angles than Bragg scattered electrons and therefore special, wider annular detectors are employed. This technique is commonly referred to as high-angle annular dark field (HAADF) imaging, and is more sensitive to Z-contrast than standard ADF [Jesson and Pennycook [1995]].

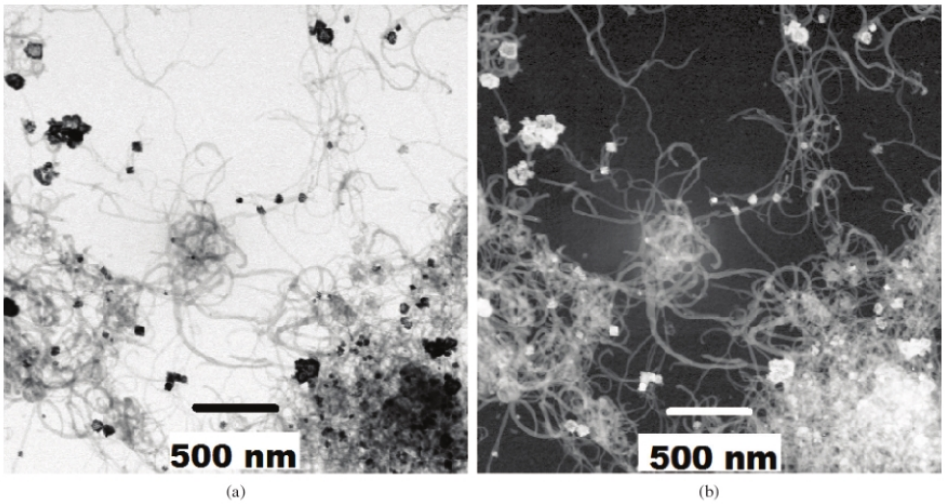

Figure 2.14: *A comparison between bright and dark field images obtained via the STEM. Both images show multi-walled carbon nano-tubes decorated with silver particles. (a) shows the bright field image, while (b) corresponds to the same image taken in annular dark field mode. From [Travessa et al. [2014]]*

Characteristic X-Rays (EDX)

This technique, also known as energy dispersive x-ray spectroscopy has already been discussed in detail in Section 2.1.1 for SEM and the generation process of x-rays is the same. EDX can also be used during TEM investigations, but as no TEM EDX data is presented in this thesis, this technique will not be described in detail here.

2.2 Powder X-Ray Diffraction (XRD)

X-ray powder diffraction is a powerful tool for the investigation of nano-particles. Via the obtained spectrum it is possible to accurately confirm the composition of a selected nano-powder by comparison with standard reference spectra. Furthermore, the peak position and width give an indication of particle size and, potentially, about possible stress and strain in the crystal lattice.

2.2.1 Experimental Set-up

The experimental set-up of a standard x-ray powder diffraction experiment can be seen in Figure 2.15:

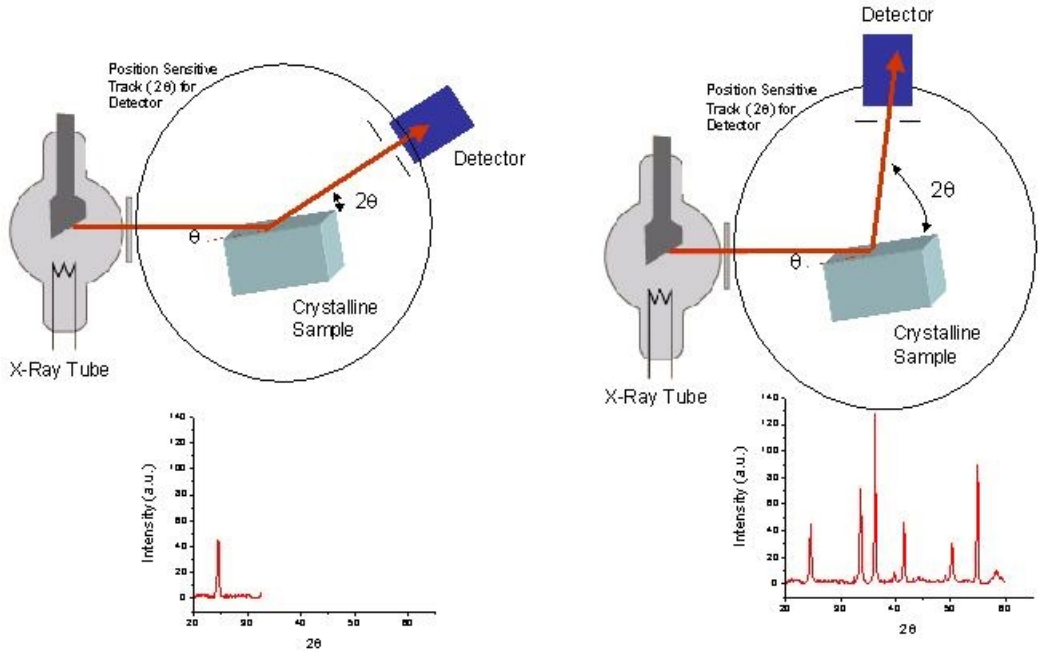

Figure 2.15: *The set-up of an x-ray powder diffraction (XRD) machine. The sample is mounted centrally and illuminated by an x-ray source. Both source and detector can be mounted on movable arms, and are tilted in one plane to obtain the full spectrum of angles. From [Bullen [2008]]*

The set-up can be split into three main sections. The primary section consists of the x-ray source. The generation of x-rays in x-ray powder diffractometers is commonly done using an x-ray tube. The tube is evacuated and contains an anode and a cathode. A high potential is applied between anode and cathode, leading to a beam discharge of electrons between the two. Commonly, this potential is in the range of 30 to 150 kV. As the electrons jump from the cathode and impact on the anode, they release part of their kinetic energy (roughly 1%) as a photon in the x-ray spectrum (bremsstrahlung). The exact emission spectrum depends on both the accelerating voltage and the anode material. These materials can include metals such as copper, molybdenum or cobalt [Klug and Alexander [1974]].

The generated x-rays are then directed onto a sample holder in the centre of the apparatus. Commonly, this is a circular hole filled with a specimen, which has been compressed to create a smooth surface. As the x-rays impact the sample, they are subjected to Bragg scattering in the lattice planes of the specimen, and as a consequence, Bragg-scattered x-ray beams are emitted.

On the far end of the experiment, an x-ray detector is mounted on a movable

platform. By moving the detector in such a way that it covers a range of possible diffraction angles and measuring the counts of detected x-rays, an x-ray spectrum can be collected.

The collected spectrum can then be evaluated in terms of several different parameters. Crystallinity, particle size and strain, bulk modulus and phase transitions can all be investigated this way. In this project, the main interest lay in two types of information obtained this way. The obtained spectra were used to confirm the presence or absence of expected material compounds through a comparison with reference spectra. On the other hand, particle sizes can be investigated using this method. The basis of this is the Scherrer Equation [Holzwarth and Gibson [2011]]:

$$B(2\theta)\cos(\theta) = \frac{\kappa\lambda}{D} \tag{2.19}$$

D represents the size of the particles in the nano-powder, while κ is a shape factor and usually close to unity. λ corresponds to the wavelength of the used x-rays. B is the peak broadening (full width at half maximum) of a specific peak in the spectrum at angle 2θ. It needs to be pointed out that strain in the sample also contributes to the peak broadening, and so Scherrer's Equation must be amended to take this into account [Langford and Wilson [1978]]:

$$B(2\theta)\cos(\theta) = \frac{\kappa\lambda}{D} + \eta\sin(\theta) \tag{2.20}$$

Here, η is a measure for the microstrain in the nano-crystallite, which is caused by non-uniform lattice distortions, faulting, dislocations, antiphase domain boundaries and grain surface relaxation. When plotting $B(2\theta)\cos(\theta)$ against $\sin(\theta)$, the result is a straight line with slope η and intersect $\frac{\kappa\lambda}{D}$. However, as microstrains in the produced nano-powders were not investigated in this thesis, the method for determining microstrain will not be presented here in further detail.

2.3 Surface Area Determination

2.3.1 Isotherms and the Brunauer-Emmett-Teller Method (BET)

In 1938, Stephen Brunauer, P.H. Emmett and Edward Teller introduced a new method of calculating the surface area of a given material using the adsorption isotherms of a given gas on the material [Brunauer et al. [1938]]. Their approach followed a route to derive an expression for multi-molecular adsorption using Langmuir's theory. This technique was used to estimate experimentally the overall surface area per unit mass of the materials under investigation.

Basic Principles

As mentioned above, the general derivation followed a similar route to that taken by Langmuir in his derivation for the case of uni-molecular adsorption. The following is a summary of the derivation performed by Brunauer, Emmett and Teller.

Let S_i represent the surface area covered by i layers of adsorbed gas molecules. In a state of equilibrium, S_0 must remain constant, and thus the rate of adsorption of molecules onto the bare surface must equal the rate of evaporation from the first layer:

$$a_1 * p * S_0 = b_1 * S_1 * exp\left(-\frac{E_1}{RT}\right) \tag{2.21}$$

In this, and in following equations, a_i and b_i are constants, p is the pressure and E_i is the heat of adsorption of the i-th layer of adsorbed gas molecules.

If S_1 is at equilibrium, the evaporation from S_1 and the condensation on the same surface must be equal to the condensation on S_0 and the evaporation from S_2:

$$a_2 * p * S_1 + b_1 * S_1 * exp\left(-\frac{E_1}{RT}\right) = a_1 * p * S_0 + b_2 * S_2 * exp\left(-\frac{E_2}{RT}\right) \tag{2.22}$$

By substituting Equation (2.21) into Equation (2.22), it follows:

$$a_2 * p * S_1 = b_2 * S_2 * exp\left(-\frac{E_2}{RT}\right) \tag{2.23}$$

Extending the same argument to further layers gives:

$$a_i * p * S_{i-1} = b_i * S_i * exp\left(-\frac{E_i}{RT}\right) \tag{2.24}$$

The total surface area A of the sample and the total adsorbed volume v are (with v_0 representing the unit volume of an adsorbed mono-layer of gas per unit area):

$$A = \sum_{i=0}^{\infty} S_i \tag{2.25}$$

$$v = v_0 * \sum_{i=0}^{\infty} i S_i \tag{2.26}$$

Thus, Equation (2.25) and Equation (2.26) give:

$$\frac{v}{A * v_0} = \frac{v}{v_m} = \frac{\sum_{i=0}^{\infty} iS_i}{\sum_{i=0}^{\infty} S_i} \tag{2.27}$$

Here, v_m is the volume of gas adsorbed when the entire adsorbant surface is covered with a complete uni-molecular gas layer. Making two assumptions at this point allows the summations to be carried out. The first assumption is that the heat of adsorption E_i is the same for each layer after the first layer has been adsorbed and that their values are equal to the heat of liquefaction, E_L, of the gas:

$$E_2 = E_3 = ... = E_L \tag{2.28}$$

The second assumption is that the ratio of the constants a_i and b_i is the same for the second and all higher layers. In general, this can be justified using the assumption that the evaporation and condensation properties of the gas molecules are the same as what would be expected for the liquid state:

$$\frac{a_2}{b_2} = \frac{a_3}{b_3} = \frac{a_4}{b_4} = ... = \frac{1}{g} \tag{2.29}$$

This leads to:

$$S_1 = \frac{a_1}{b_1} * p * exp(\frac{E_1}{RT}) * S_0 = y * S_0 \tag{2.30}$$

$$S_2 = \frac{p}{g} * exp(\frac{E_L}{RT}) * S_1 = x * S_1 \tag{2.31}$$

$$S_3 = \frac{p}{g} * exp(\frac{E_L}{RT}) * S_2 = x * S_2 = x^2 * S_1 \tag{2.32}$$

$$S_i = x * S_{i-1} = x^{i-1} * S_1 = y * x^{i-1} * S_0 = \frac{y}{x} * x^i * S_0 = c * x^i * S_0 \tag{2.33}$$

$$c = \frac{y}{x} = \frac{a_1 * g}{b_1} * exp\left(\frac{(E_1 - E_L)}{RT}\right) \tag{2.34}$$

With:

$$y = \frac{a_1}{b_1} * p * \exp(\frac{E_1}{RT}) \tag{2.35}$$

$$x = \frac{p}{g} * \exp(\frac{E_L}{RT}) \tag{2.36}$$

It follows that:

$$\frac{v}{v_m} = \frac{cS_0 \sum_{i=1}^{\infty} ix^i}{S_0 \left[1 + c \sum_{i=1}^{\infty} x^i\right]} \tag{2.37}$$

Provided $0 < x < 1$, the sum in the denominator is simply the sum of a geometric series, which is well-defined and known to be:

$$\sum_{i=1}^{\infty} x^i = \frac{x}{1-x} \tag{2.38}$$

Then it is possible to rewrite the other power series as the derivative of the first, allowing the use of the same approach as above to evaluate the summation:

$$\sum_{i=1}^{\infty} ix^i = x\frac{d}{dx}\sum_{i=1}^{\infty} x^i = x\frac{d}{dx}\frac{x}{1-x} = \frac{x}{(1-x)^2} \tag{2.39}$$

Using Equation (2.38) and Equation (2.39) in Equation (2.37) gives a much more simplified description of v/v_m:

$$\frac{v}{v_m} = \frac{cx}{(1-x)(1-x+cx)} \tag{2.40}$$

If the pressure is allowed to reach the saturation pressure, p_0, then for the case of a free surface, an infinite amount of layers will build up on the surface. Therefore, v must tend to infinity when $p \longrightarrow p_0$. With Equation (2.40) this leads to:

$$\lim_{p \to p_0} x = 1 \tag{2.41}$$

With Equation (2.36), this gives:

$$1 = \frac{p_0}{g} * exp\left(\frac{E_L}{RT}\right) \tag{2.42}$$

Using Equation (2.36) again gives:

$$x = \frac{p}{p_0} \tag{2.43}$$

Substituting this result back into Equation (2.40) and rearranging to solve for v gives:

$$v = \frac{v_m c p}{(p_0 - p)(1 + (c-1)\frac{p}{p_0})} \tag{2.44}$$

This equation gives the standard S-shaped isotherms. However, for testing purposes, it is more convenient to rearrange it into the following form:

$$\frac{p}{v(p_0 - p)} = \frac{1}{v_m c} + \frac{(c-1)}{v_m c}\frac{p}{p_0} \tag{2.45}$$

This equation can be used to evaluate the graph of the straight line obtained by plotting $p/(v(p_0 - p))$ against p/p_0. Thus the gradient G of the slope gives

$$G = \frac{(c-1)}{v_m c} \tag{2.46}$$

while the intercept I of the line with the $p/(v(p_0 - p))$ axis gives

$$I = \frac{1}{v_m c} \tag{2.47}$$

As shown in Brunauer et al. [1938], v_m, the volume of a gas needed for a uni-molecular adsorbed layer, and c, which can be shown to be approximately equal to $exp((E_1 - E_L)/RT)$, can be graphically obtained from graphs as shown in Figure 2.16.

Finally, the value for v_m can then be used to calculate a value for the specific surface area S_{ssa} of the material under investigation using the relationship:

$$S_{ssa} = \frac{Ns}{Va} v_m \tag{2.48}$$

where N is Avogadro's number, s is the adsorption cross-section of the adsorbed gas molecules, V is the molar volume of the gas and a is the mass of the adsorbed gas.

2.3.2 Experimental Set-up

The machine used for the measurement of the isotherm and subsequent BET evaluation was an ASAP 2020 porosimetre. It used a dynamic flow set-up as shown in Figure 2.17. The experiment was split up into two different sections. First, the

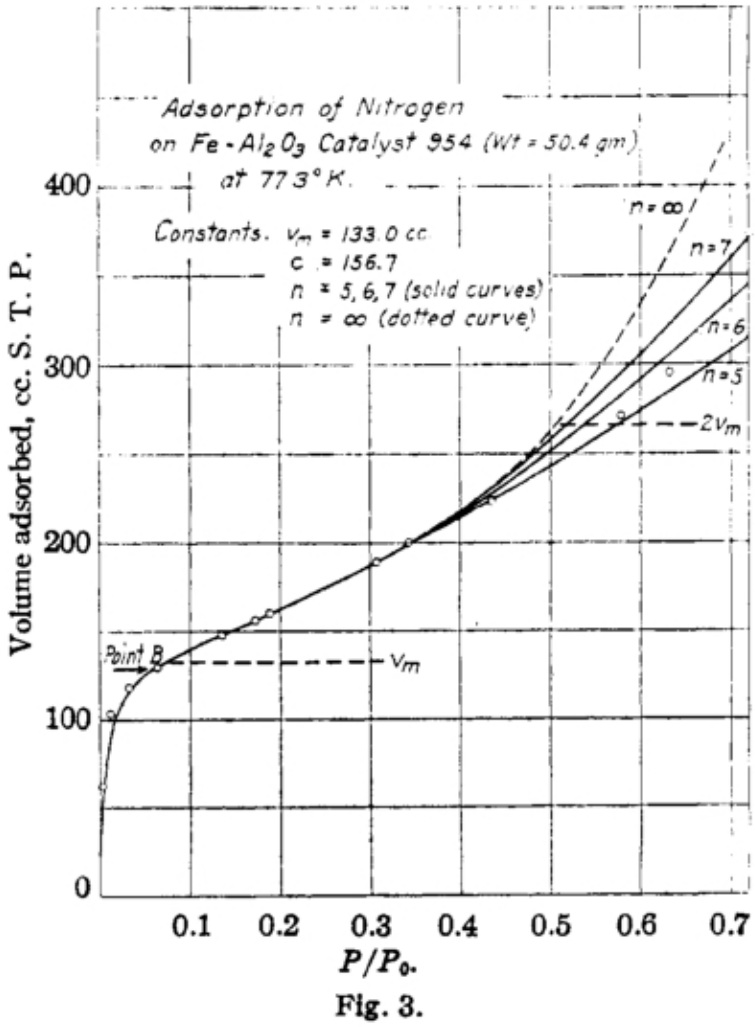

Figure 2.16: *Isotherm/straight plot. From [Brunauer et al. [1938]]*

sample needed to be freed from any previously adsorbed gasses. This step was called *outgassing* and could be achieved through several mechanisms including adsorption-desorption cycling, heating, vacuum exposure and purging with dry non-reactive gasses such as helium.

Once this step was completed, the set-up allowed the machine to collect the isotherm by slowly adding and then removing the adsorption gas. The standard gas used for the adsorption process was nitrogen gas.

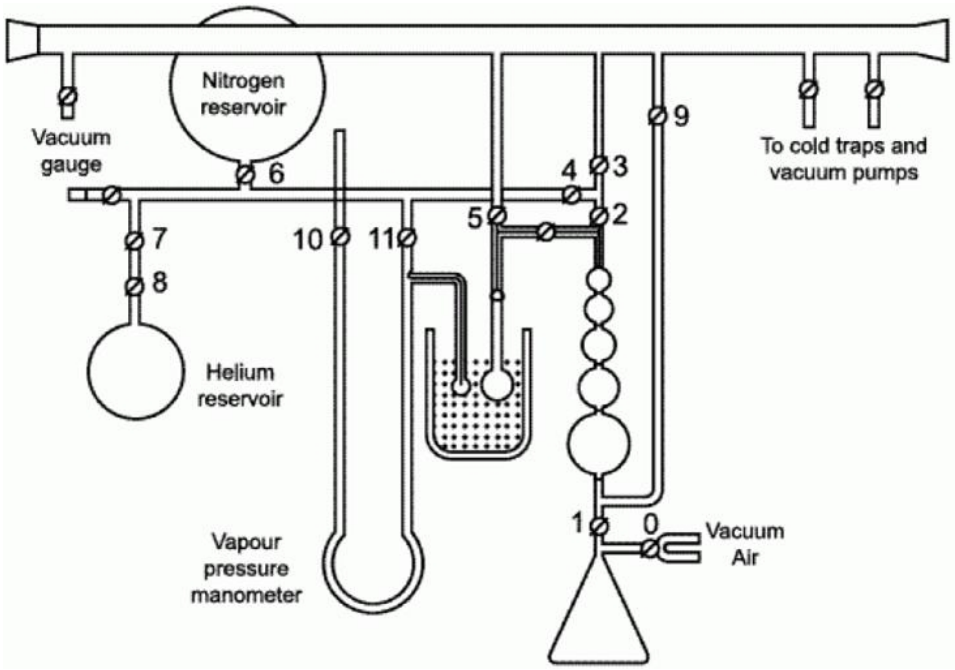

Figure 2.17: *The rough set-up of a dynamic flow method apparatus, which measures the isotherms used in the BET method. The numbers represent different valves in the diagram. From [Particle Analytical [2014]]*

2.4 Electrochemical Analysis

In order to determine the electrochemical properties of an electrode material, several different types of experiments can be conducted. The most common include galvanostatic cycling, cyclic and linear voltammetry, and impedance spectroscopy.

Electrochemical impedance spectroscopy (EIS) has slowly established itself over the last decades as a tool to investigate conductivity and charge-transfer properties, as well as capacity loss mechanisms of lithium ion cells [Zhuang et al. [2012]]. In this project, efforts were focused on galvanostatic cycling and voltammetry measurements, and so EIS will not be discussed further here.

2.4.1 Galvanostatic Cycling

The easiest way to test a battery is to subject it to a charge-discharge cycle and measure the development of the cell voltage as it moves through distinct states of charge or discharge. This is done by constructing a test cell consisting of the electrode to be tested, as well as a standard known electrolyte and counter electrode. The limits of the charge-discharge cycles are set by defining an upper and a lower

cell potential limit. The cell is then connected to a galvanostat, which produces a constant current. This current is subsequently applied to the cell to force either a charge or discharge. At the same time, the cell potential is measured [Campos et al. [2013]]. A sample of a resulting galvanostatic cycling plot is shown in Figure 2.18:

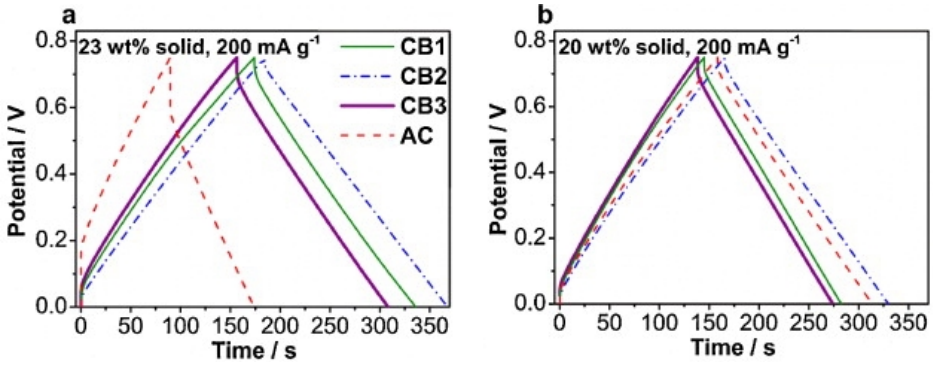

Figure 2.18: *Sample charge-discharge curves as obtained during galvanostatic cycling of a carbon-based electrochemical flow capacitor. From [Campos et al. [2013]]*

By examining the smoothness of the curve, it is possible to check for faults in the electrodes, which become visible as jumps and discontinuities.

A very important property that can be calculated from these graphs is the overall charge capacity of the cell. The stored charge between any two points in time during a charge cycle can simply be calculated by multiplying the time Δt with the current I (as the galvanostat provides a constant current):

$$C(\Delta t, I) = I * \Delta t \tag{2.49}$$

By running the charge cycle to completion, i.e. until the battery potential reaches its user-defined limit, the overall charge capacity can be measured. If this process is carried out in a similar fashion for the discharge cycle, it is possible to determine the amount of retrieved charge. In an ideal case, all stored charge should be retrieved, however, in reality this is not the case. Small amounts of charge are lost over time due to diffusion or chemical re-arrangement within the cell, possibly caused by current-induced cell damage.

By subjecting the same cell to repeated charge-discharge cycles, it is possible to determine the development of the charge capacity as a function of cell use. As common cells degrade over time, the lifetime of the cell is determined by the number of cycles it can confidently complete before overall charge capacity drops below a threshold value. Common cells, such as mobile phone batteries, have got cycle lives

of around 500 cycles, but specialised cells exist that can withstand beyond 10000 cycles [Wilka [2013]].

2.4.2 Cyclic Voltammetry

During cyclic voltammetry, a three-electrode set-up is used. Apart from the usual working and counter electrode, a reference electrode is introduced, the purpose of which is to ensure good potential control between the working and counter electrode [Hickling [1942]]. To operate a three electrode set-up and to ensure a good potential control, a special instrument called a potentiostat is used [Bard and Faulkner [2000]].

During a cyclic voltammetry experiment, the potential between the two active electrodes (working and counter) is very tightly controlled. Two voltage limits are set, after which the voltage is ramped at a steady gradient between both limits. The measured quantity is the current that develops between both electrodes. The cycle between lower-upper-lower voltage limits can be repeated as often as desired. When it is only carried out once, it is commonly referred to as linear sweep voltammetry.

By observing the current between working and counter electrode, it is possible to investigate the electrochemical properties of a substance in solution and reactions taking place on the electrode surfaces. Thus, for investigating the electrochemical properties of a novel electrode material, it is possible to use a cyclic voltammogram to determine what reactions take place by looking for specific peaks in the current. A sample voltammogram is shown in Figure 2.19.

Furthermore, Nernst's Equation gives an expression for the cell potential E [Wahl [2005]]:

$$E = E^{0'} - \frac{RT}{nF}\ln(Q) \tag{2.50}$$

$E^{0'}$ – Formal electrode potential [V]
R – Ideal gas constant [J/(K*mol)]
T – Temperature [K]
n – Number of moles of transfered charge carriers
F – Faraday's constant [Coulomb/mol]
Q – Reaction quotient

$E^{0'}$ is directly measurable from the cyclic voltammogram. It can be approximated as the average value between the potential E_{max} at the point of maximum

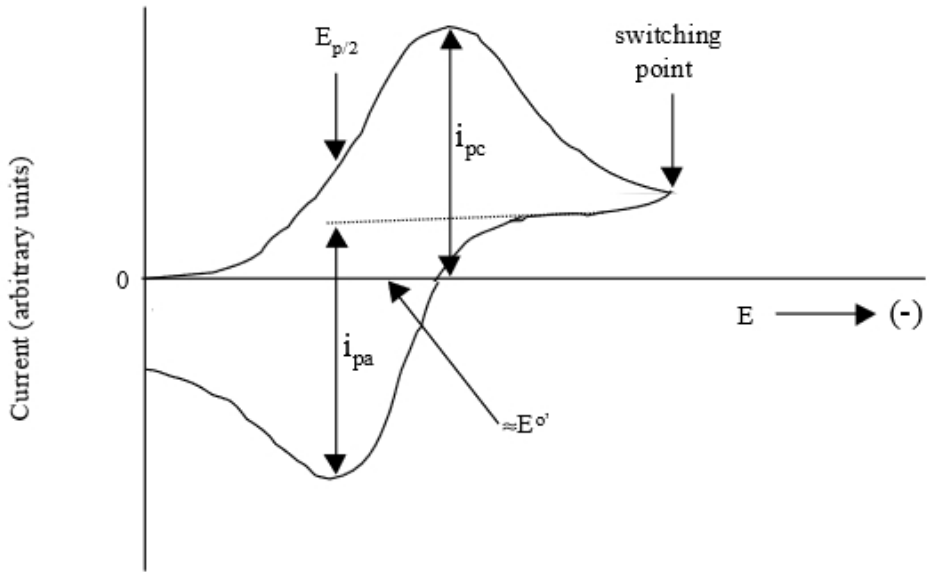

Figure 2.19: *An example of a single cycle as obtained through cyclic voltammetry. More complex electrode chemistries show more current peaks, which can be attributed to different cell reactions taking place. The value of $E^{0'}$ can easily be determined in this case. From [Severin [1999]]*

current and the potential E_{min} at the point of minimum current:

$$E^{0'} = \frac{E_{max} - E_{min}}{2} \tag{2.51}$$

It is also possible to calculate the equilibrium constant κ of the electrochemical cell by considering the equilibrium at room temperature with E = 0V and Q = κ by using Equation (2.50):

$$\log_{10}\kappa = \frac{nE^{0'}}{59.2mV} \text{ at T} = 25°\text{C} = 298\text{K} \tag{2.52}$$

2.5 Synthesis Techniques

A brief introduction will be given to two techniques used in the synthesis, the hydrothermal synthesis and the method of gas production using a Kipps apparatus. However, as both methods were tweaked and adapted during the project, a more detailed description is given at the beginning of the relevant chapters.

2.5.1 Hydrothermal Synthesis

A hydrothermal or solvothermal synthesis is the process by which both high vapour pressures and temperatures are exploited to cause nano-crystal growth directly from a solution of reactants in either water (hydro-) or other solvents (solvo-). Here, initially a solution of two or more reactants in a liquid medium is produced. The solution is then filled into a pressure-resistant vessel, often referred to as an autoclave or hydrothermal bomb. The outer material of the autoclave is often stainless steel due to its material strength, while an inner sleeve contains the actual solution. This inner sleeve is made out of inert material that will not participate in the reactions taking place inside the autoclave. During this project, an inner sleeve made from teflon was used. The autoclave is then sealed shut and inserted into a furnace or oven. It is common practice to equip the autoclave with an emergency pressure release valve to prevent it from accidentally reaching critical inner pressures, which could lead to an explosion. The entire autoclave is then heated. The increased temperature has both the effect of accelerating or enabling certain reactions within the autoclave, as well as causing an increase in internal pressure. The combination of high temperatures and pressures causes the crystallisation of a large number of nano-scale crystals directly from the liquid medium [Byrappa and Yoshimura [2012]]. These were then further used in this project for characterisation and electrode production.

2.5.2 The Kipps Apparatus

The Kipps apparatus is a multi-chambered reaction vessel designed for a self-limiting production of specific gases (see Figure 2.20). It consists of three separate glass chambers that are place on top of each other. The top chamber acts as a reservoir for an acid and is directly connected to the bottom chamber, completely bypassing the central chamber. Therefore, the acid is free to flow, assisted by gravity, from the top to the bottom chamber. The bottom chamber also serves as a reservoir for the acid, which collects the liquid and slowly fills as the top chamber empties. The bottom chamber, however, is connected at its top to the second chamber, and so it is possible for the acid to eventually move into the second chamber once the bottom chamber is completely filled. The central chamber contains a material capable of reacting with the acid under production of the desired gas, such as iron sulfide in the case of hydrochloric acid when producing hydrogen sulfide gas. A permeable stopper prevents the solid from dropping into the lower chamber, while still allowing the acid to rise. A single valve in the second chamber provides the only exit for the

produced gas. By sealing the valve shut, gas production continues in the central chamber, causing the pressure to rise, which eventually causes the acid to be pushed back into the bottom and, from there, into the top chamber. Thereby the reaction separates the two reactants physically, stopping the reaction until the valve is opened again [Darling [2013]].

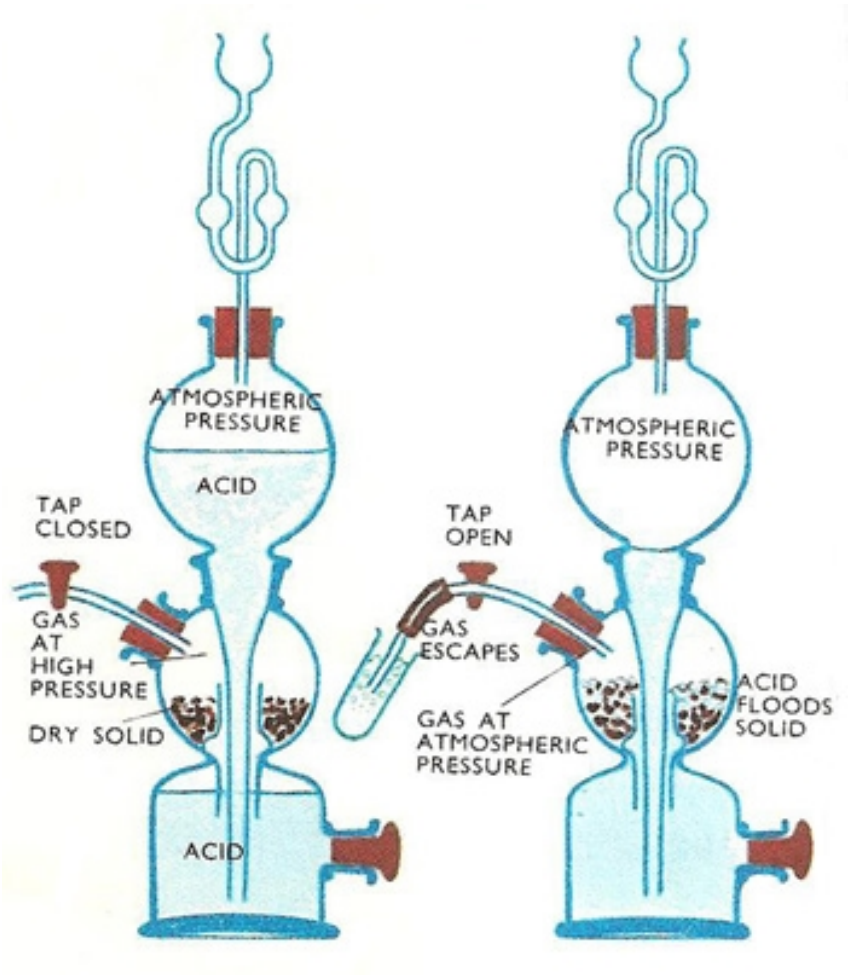

Figure 2.20: *A schematic diagram of a Kipp's apparatus. The reaction in the centre is moderated by the release of hydrogen sulfide gas, and automatically shuts itself off by pushing the acid out of the chamber if the valve remains closed. From [Darling [2013]].*

This method of gas production has the advantage of self-limiting the production to just the amount of gas needed, while providing a cheap and facile alternative to purchasing gas cylinders. For these reasons this method was chosen in this project.

Chapter 3

Material Synthesis and Morphological Characterisation of SnS_2

As has been discussed in the literature review (see Chapter 1), a great variety of different SnS_2 nano-structures have already been synthesised under controlled conditions and their morphologies characterised. In an attempt to enhance and optimise these nano-structures in regard to their lithium ion storage properties, several novel structures were synthesised. Their synthesis will be introduced in this chapter and their morphological properties investigated.

3.1 Material Synthesis

The synthesis followed a solvothermal approach, similar to the one described in Hai et al. [2001]. A mixture of tin(IV) chloride hyd. and thioacetamide was dissolved in pure ethanol. During the dissolution, tin(IV) chloride hyd. separated into two ions and water:

$$SnCl_4 \cdot 4H_2O \xrightarrow{ethanol} Sn^{4+} + 4Cl^- + 4H_2O \tag{3.1}$$

The solution was then inserted into an autoclave and heated for a predefined time at a set temperature (for a breakdown of each discussed morphology, see Section 3.3.1). The standard synthesis parameters (see Table 3.1) used for this project were based on a dwell time of 10 hours at 70°C, which were determined via trial-and-error during the course of the project and produced the highest concentration of nano-worm structures, the morphology this project focused on, as discussed in a

later section.

Parameter Name	Parameter Value
Mass of Thioacetamide	90mg
Mass of Tin(IV) chloride hyd.	190mg
Volume of Ethanol	40ml
Dwell Temperature	70°C
Temperature ramp rate	5°C per minute
Dwell Time	10 hours
Pressure inside the autoclave	≈ 1.9 bar
Precipitate colour	Orange-Brown
Number of washing cycles with pure Ethanol	4 cycles
Drying Temperature	60°C
Drying Time	4-6 hours
Final Yield	Approx. 30-35mg powder yield

Table 3.1: *A breakdown of a sample procedure for a typical synthesis set-up.*

Under the influence of heat, thioacetamide reacted with the released water (see Equation (3.1)) to produce dihydrogen sulfide, which acted as the sulfur source for the sulfidisation process needed for the creation of tin disulfide. The reaction scheme was as follows:

$$CH_3CSNH_2 + H_2O \longrightarrow CH_3CONH_2 + H_2S \tag{3.2}$$

The dihydrogen sulfide, still in solution, reacted readily with the active tin ions under the creation of tin disulfide. Other combinations of tin and sulfur, such as tin monosulfide (SnS) and ditin trisulfide (Sn_2S_3), could have also been synthesised, but were shown to be absent in the reaction products using several techniques (see Section 3.2). The reaction path for the final step in the synthesis was:

$$Sn^{4+} + 2H_2S \longrightarrow SnS_2 + 4H^+ \tag{3.3}$$

This led to a combined reaction equation for the entire process, which was also used to calculate the required ratio of the different reactant materials:

$$SnCl_4 \cdot 4H_2O + 2CH_3CSNH_2 \longrightarrow SnS_2 + 2CH_3CONH_2 + 4H^+ + 4Cl^- + 2H_2O \tag{3.4}$$

Two main observations could be made based on this equation. First, the molar ratio between the two reactants should be close to 1:2 to allow for a full reaction. In practice, the synthesis was run with a slight surplus of thioacetamide to ensure a full consumption of the tin(IV) chloride hyd., which would otherwise remain as a contaminant in the final product. Second, as all reaction products apart from tin disulfide remained dissolved, the final product could be purified through repeated washing with ethanol and distilled water. As can be seen in Figure 3.1, reactant ratios must be chosen carefully to ensure the right product is obtained. During this project, the mass of thioacetamide and tin(IV) chloride was chosen so that the ratio of Sn:S was roughly 1:2, thereby ensuring the production of SnS_2 for all but the highest temperatures.

By allowing the reaction to take place in an autoclave (a pressure vessel as depicted in Figure 3.2) and under raised temperatures, and therefore pressure, the reaction product was forced to nucleate rapidly from solution. The pressure inside the autoclave at varying temperatures can be approximated using Antoine's Equation [Antoine [1888]]:

$$log_{10}(P(T)) = A - \left(\frac{B}{T + C}\right) \tag{3.5}$$

Here, P(T) is the vapour pressure (in bar) at a given temperature T (in Kelvin), and A, B and C are material-dependent coefficients. The pressure inside the vessel between room temperature and 90°C is shown in Figure 3.3. For ethanol at 70°C=T_{70}, the coefficients A, B and C are [NIST [2011]]:

$$A = 5.24677$$
$$B = 1598.673$$
$$C = -46.424$$

$$log_{10}(P(T_{70})) = 5.24677 - \left(\frac{1598.673}{343.15 - 46.424}\right) = -0.1409 \tag{3.6}$$

$$\Rightarrow P(T_{70}) = 10^{-0.1409}\ bar = 0.7229\ bar \tag{3.7}$$

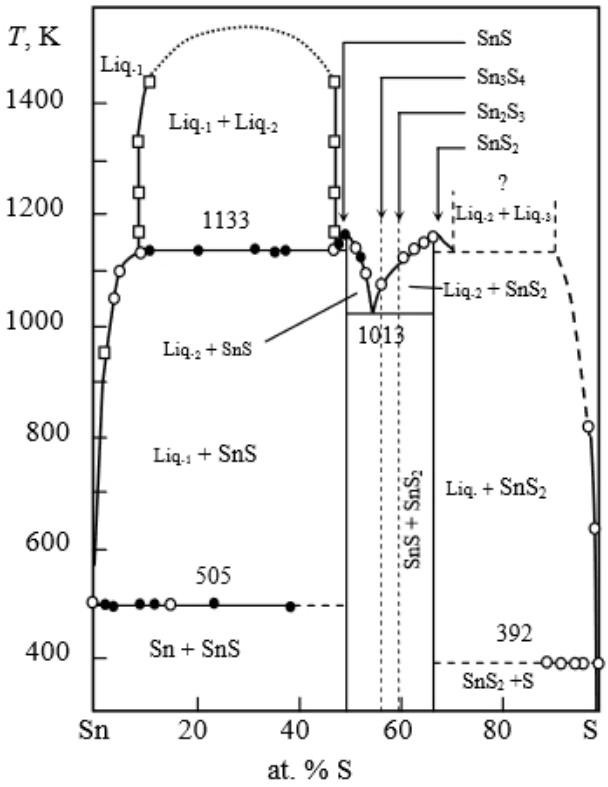

Figure 3.1: *A phase diagram for the Sn - S system. By choosing the composition of reactants in an appropriate manner, it is possible to restrict the product type accordingly. Work done during this project was chosen to fall at roughly 66% sulfur, ensuring the product to be SnS_2. From [Bletskan [2005]]*

As the autoclave was only filled up to 80% of its total volume, a small cushion of atmospheric air remained upon sealing of the vessel. When heating the autoclave, the partial pressure of this cushion of air rose to [Halliday et al. [2009]]:

$$P_{air} = \frac{RT}{V_m} = \frac{8.314 \frac{J}{mol\ K}\ 343.15K}{24.465 \frac{l}{mol}} = 116.61\ kPa \approx 1.17\ bar \tag{3.8}$$

Therefore, the total pressure inside the autoclave at 70 °C was the sum of the vapour pressure of ethanol and the increased pressure of air, 1.89bar.

The rise in pressure had the effect that the resulting SnS_2 particle size was very small with dimensions in the realm of nano-particles (and up to micrometres under the right conditions, for example by lengthening the dwell time or increasing the reaction temperature). A small partial product loss occurred through precipitation and adhesion on the autoclave walls. This reduced the overall output, but

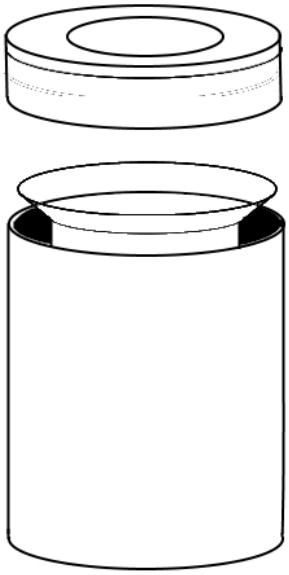

Figure 3.2: *A schematic of the utilised pressure vessel. The vessel had an inner volume of 40 ml. The inner sleeve was made of Teflon. All other components were made of stainless steel.*

the losses were negligible, as it was possible to remove material sticking to the walls by sonication. The main product losses occurred during the several washing phases, where up to 60% could be lost. After the heating phase, the autoclave was allowed to return to room temperature naturally. The sample, tin disulfide in form of a yellow-brown sediment in the reaction solution, was removed and subjected to several washing cycles with pure ethanol. After a final drying process at $60°C$ under vacuum, the yellow-brown powder was ready for further analysis.

3.2 Elemental Analysis

After a positive comparison of the colour of the produced material with the reported colour in academic literature [Gaudin and Hamlyn [1938]], the next step was to establish the elemental composition of the sample using a range of x-ray based analytical techniques. The examination based on colour was always undertaken under the same illumination conditions inside the same fume hood and simply served as an initial test to verify the production process had not been contaminated. For example, in the case of a copper contamination, the product would be dark purple to almost black. Testing for colour was done via comparison to verified samples and was not meant to be a proof of the presence of SnS_2.

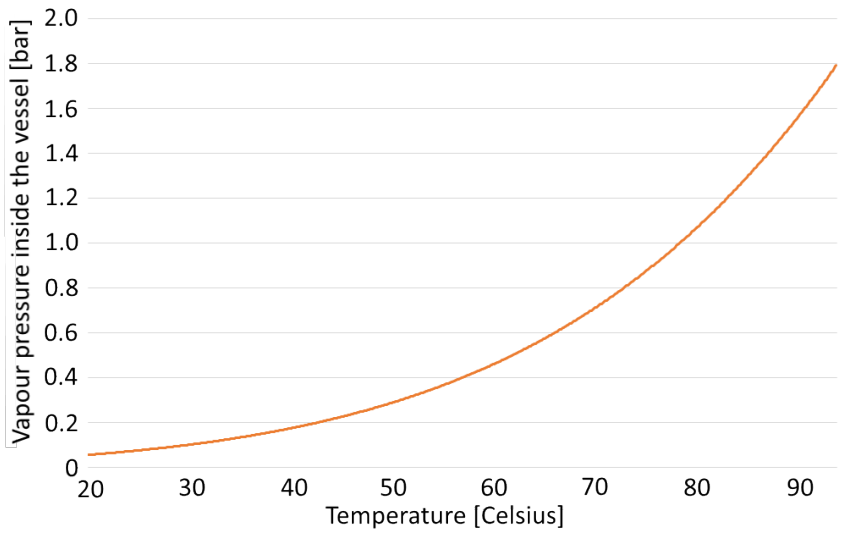

Figure 3.3: *Plot of the vapour pressure inside the autoclave vessel for the temperature range from 20 °C to 93 °C.*

3.2.1 Elemental Composition Analysis via Energy Dispersive X-Ray Spectroscopy

Energy dispersive x-ray spectroscopy was carried out on both scanning and transmission electron microscopes using an Oxford Instruments X-Max^N X-ray detector (Silicon Drift Detector) during TEM or a standard, nitrogen-cooled EDAX system during SEM. Monte Carlo simulations utilising the CASINO software package were used to determine the appropriate conditions to allow the use of this technique. It was found that 10 - 20 keV for EDX using the SEM is adequate, as illustrated for 200 electrons in Figure 3.4.

Spectra were collected for each sample of SnS_2 produced. An example spectrum collected on the SEM is shown in Figure 3.5. In each collected spectrum, the dominant single sulfur peak is clearly discernible, as well as the characteristic three peaks for tin. Other peaks may stem from further elements in the sample including silicon, carbon, aluminium, copper, oxygen and chlorine. Silicon peaks were commonly very pronounced for EDX experiments carried out under the SEM, as the samples were mounted on silicon wafer surfaces. Carbon peaks could be present either because of the sample support, which was a sticky carbon film in the case of the SEM or carbon support film in the case of the TEM, or because of general carbon contamination, stemming from reaction by-products or hydrocarbons added during the handling process. Aluminium peaks were also frequently found following that aluminium was used as a sample support inside the SEM. The same held for

the presence of copper in the case of the TEM, which uses copper grids as sample supports. Both oxygen and chlorine stemmed from incomplete washing processes and could be eliminated with a full cleaning process.

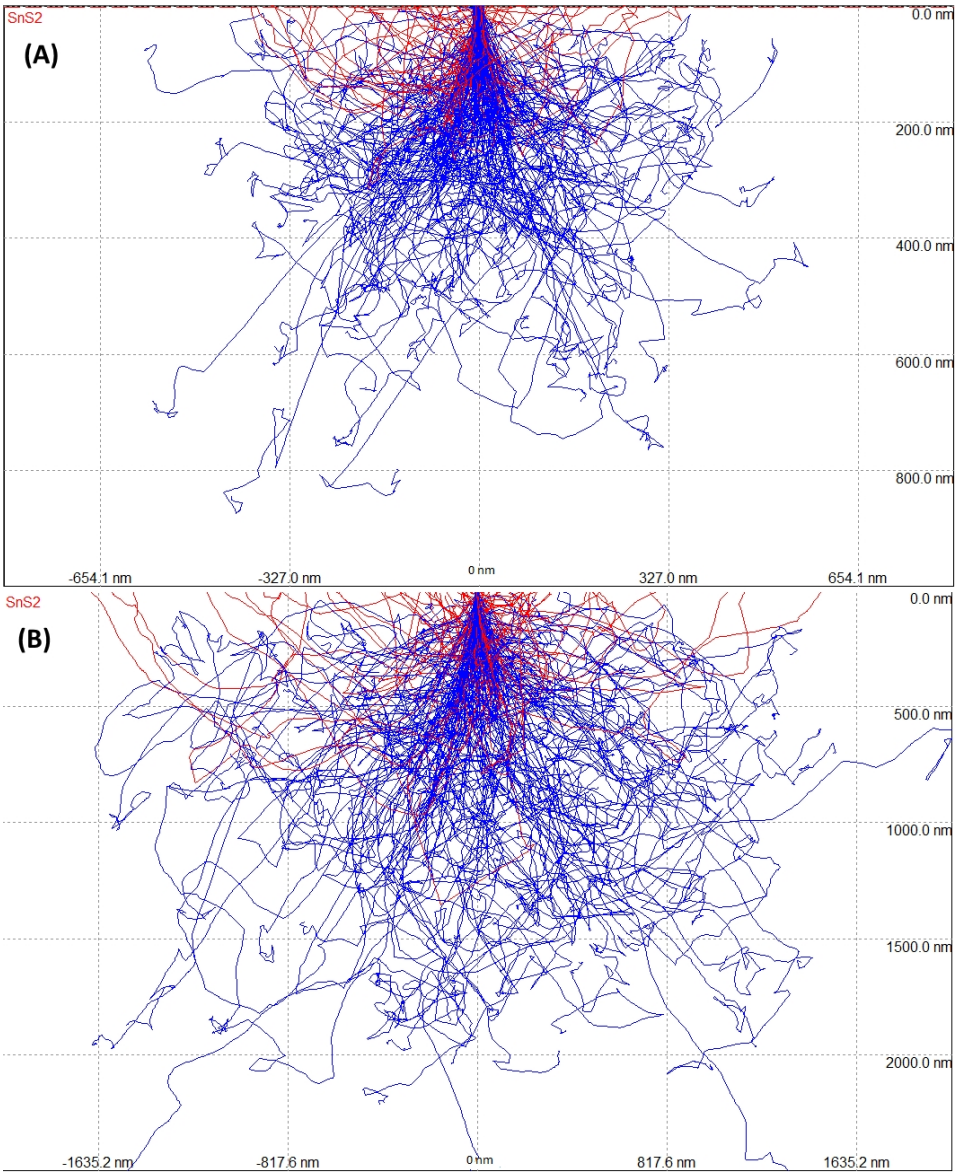

Figure 3.4: *Monte Carlo simulations for 10 keV (A) and 20 keV (B) including maximum penetration depth and maximum return signal depth. Red lines mark electron trajectories of electrons that leave the sample before absorption, while blue lines represent electrons that are eventually absorbed by the material.*

The results obtained through EDX spectroscopy were used for the quantifi-

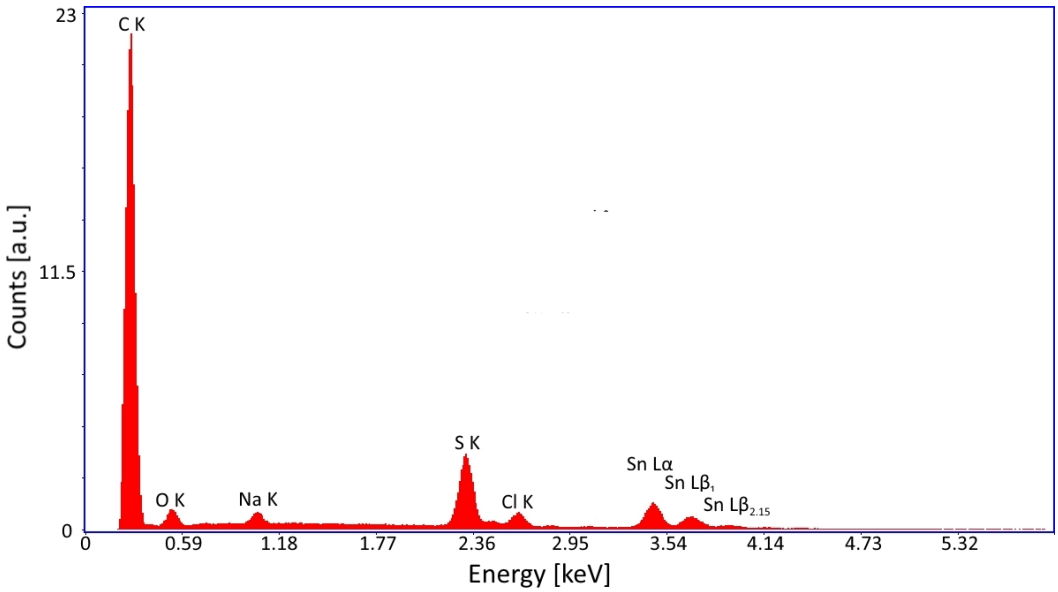

Figure 3.5: *A sample SEM EDAX spectrum as obtained from the SnS_2 material. The peaks for tin and sulfur are clear and strong. The strong carbon peak is due to the carbon substrate, and chlorine and oxygen are contaminants from the synthesis. Sodium is an external contaminant.*

cation of the elemental ratios present in the various samples produced and the global atomic ratio of tin to sulfur was always reliably close to the optimal value of 1:2, thus suggesting a high tin disulfide content.

3.2.2 Elemental Localisation via Elemental Mapping

Using the scanning ability of both the SEM and STEM, it is possible to use an EDX detector with elemental mapping software to characterise elemental localisation within the prepared materials. This allowed to quickly determine the location of clusters of elements in the various samples examined. As described in Chapter 2, an elemental spectrum was collected for each pixel in the final map to determine the elements present at this location. A sample of these maps are shown in Figure 3.6:

Figure 3.6 shows the analysis of a worm-type structure in the sample (see Section 3.3.1) for 10 keV electrons. The sample was between 150 nm (for single worms) to several microns (for clustered material) thick. Silicon was the major contaminant or background material and was well-confined to the space outside the structure. Both tin and sulfur were present as expected and made up the worm-like particles. It needs to be pointed out that no lumps or areas of unexpectedly high concentration were visible, indicating a homogeneous distribution of both elements

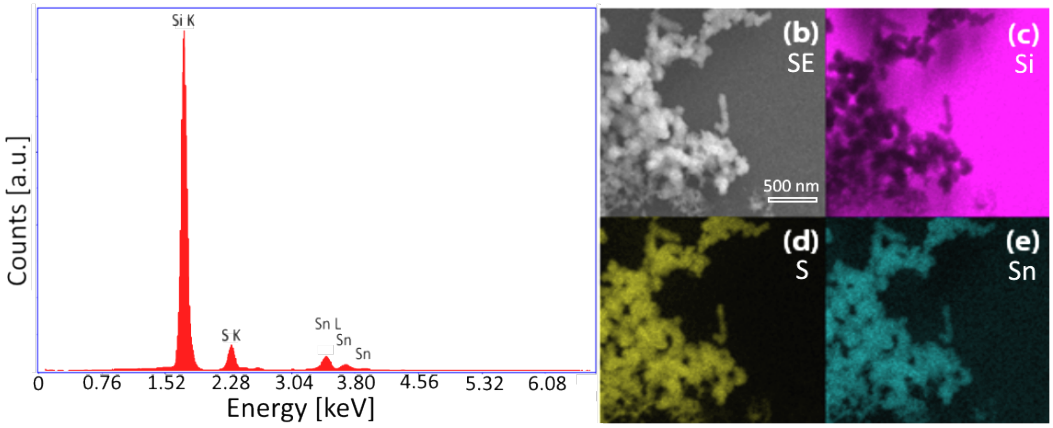

Figure 3.6: *A sample spectrum (**a**) obtained via SEM (at 10 keV). The sample area under investigation can be seen in the electron image (**b**) and contains purely nano-worm type morphologies (for more details, see Section 3.3.1). The peaks indicate the presence of Si (**c**) (Si stems from the sample support), S (**d**) and Sn (**e**). Quantification resulted in a ratio of Sn:S of 36:64, which is in good accordance to the expected value of 1:2.*

throughout the particles.

3.2.3 Elemental Fingerprinting via X-Ray Powder Diffraction

Throughout the samples tested, it was possible to determine that the structures contained both tin and sulfur. Both elements were present in a rough global ratio of 1:2 as obtained via EDX (see Figure 3.6) and there were no signs of high concentration clusters of either element found in the particles. This suggested the presence of tin disulfide as the most commonly present material type. To confirm this, x-ray powder diffraction patterns were also collected, as can be seen in Figure 3.7, which presents a collected sample spectrum of the nano-worms and provides a comparison to the bulk SnS_2 signal.

It was possible to match up the peaks in the analysed samples with the respective peaks from the bulk structure of SnS_2. Noteworthy is the fact that all identified peaks had been broadened, which was consistent with what would be expected from small particle sizes. Furthermore, it is worth pointing out that there was a change in relative peak intensities, indicating preferential lattice planes in the sample. Several of the higher angle peaks are barely or not visible anymore. This is largely due to a smearing out of peaks at higher angles, with the exception of a few preferential peaks, such as the [210] or [211] peaks.

Using Scherrer's Formula to determine particle sizes and strains, it was pos-

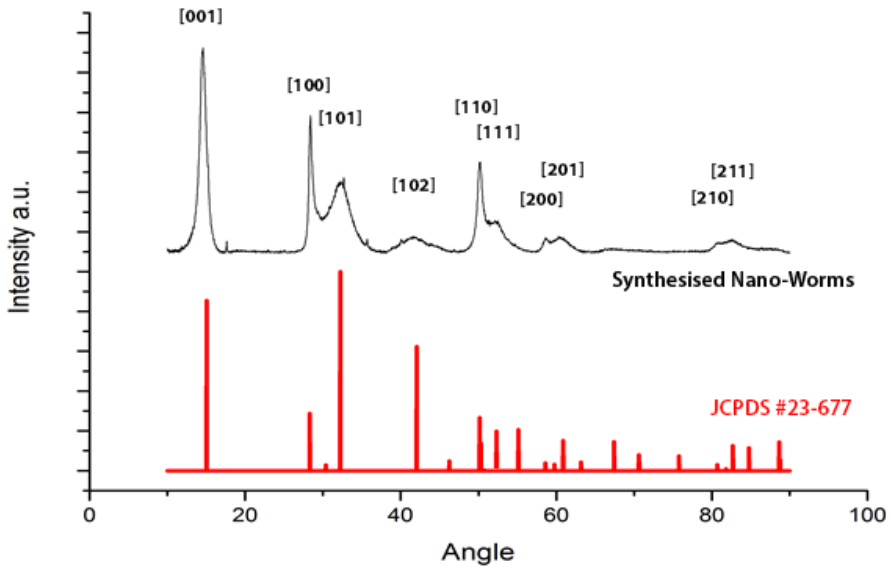

Figure 3.7: *An XRD spectrum taken from a worm-type sample and compared to the bulk signal of SnS_2 (JCPDS #23-677). Signal peaks are labelled with their bulk counterpart lattice designations. As expected, peak broadening did occur, suggesting a small particle size. Furthermore, a shift in peak intensities seems to suggest a preferential growth pattern, favouring certain lattice planes.*

sible to make an estimate of the average particle size. κ was estimated to be 0.94 based on the original reference, while λ was 0.154056 nm, the K_α wavelength of copper. Taking the [001] peak, $B(2\theta)$ is approximately 1.11°. This gives a particle size of 7.55 nm and a strain of 0.0354. Further peaks give particle size estimates of the same order of magnitude. As can be seen in later sections, the actual particles present, however, are of significantly bigger sizes, suggesting these larger particles are made up of several smaller sub-particles with their own crystallite orientation. The exact crystallite orientations and their distributions within each morphology were not determined during this project.

3.3 Morphological Characterisation of SnS_2 Nanostructures

The primary difference between the synthesised material and SnS_2 as described in literature so far, lay in its morphologies. The different types of morphologies of SnS_2 as synthesised are introduced in this section.

3.3.1 Topological Analysis via Electron Microscopy

As the produced SnS_2 particles were too small to be resolved using optical microscopy, the primary tool to investigate their morphological properties was the scanning electron microscope. Several different morphologies were observed in the samples using this technique.

In general, several competing morphologies were simultaneously present in a sample (as can be seen in Figure 3.8, which shows a combination of both thick and thin SnS_2 nano-worms, as well as a nano-flower). By fine-tuning the synthesis parameters, it was possible to create conditions favouring certain morphologies.

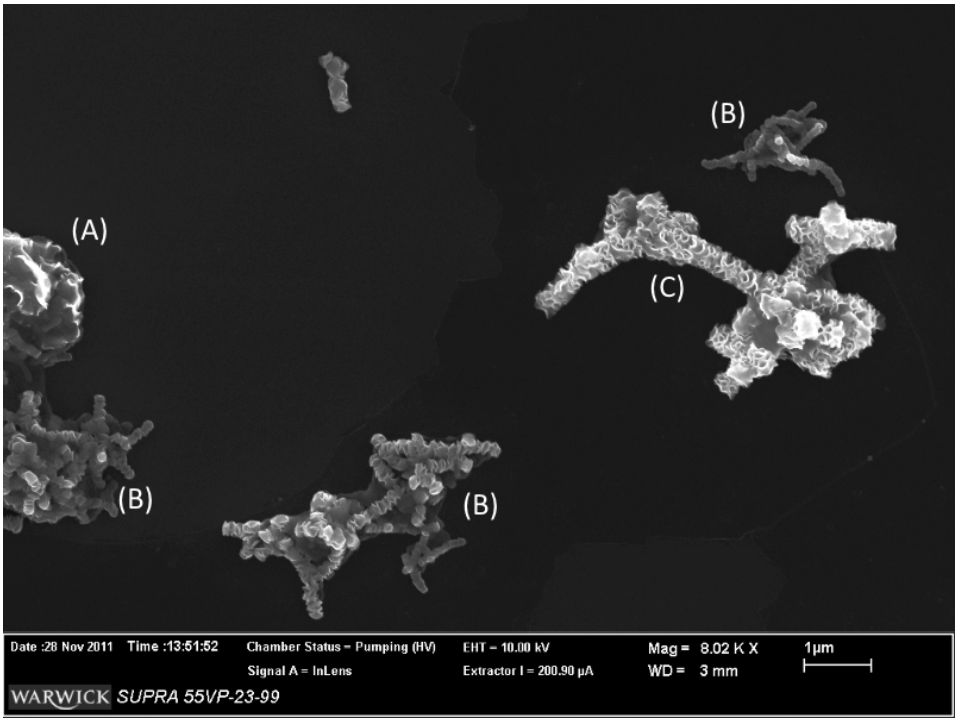

Figure 3.8: *A general image showing all three main morphologies that were encountered. On the centre left hand side, half a nano-flower is visible (A), while both thin (B) and thick (C) nano-worms form small clusters in the main body of the image.*

To verify the structure, the layer spacings could be checked using TEM images. The observed layer spacing needs to correspond with the theoretical value of 0.59 nm. Further tests to exactly determine the elemental composition were then undertaken to confirm the result. An image showing the layer spacings is presented in Figure 3.9:

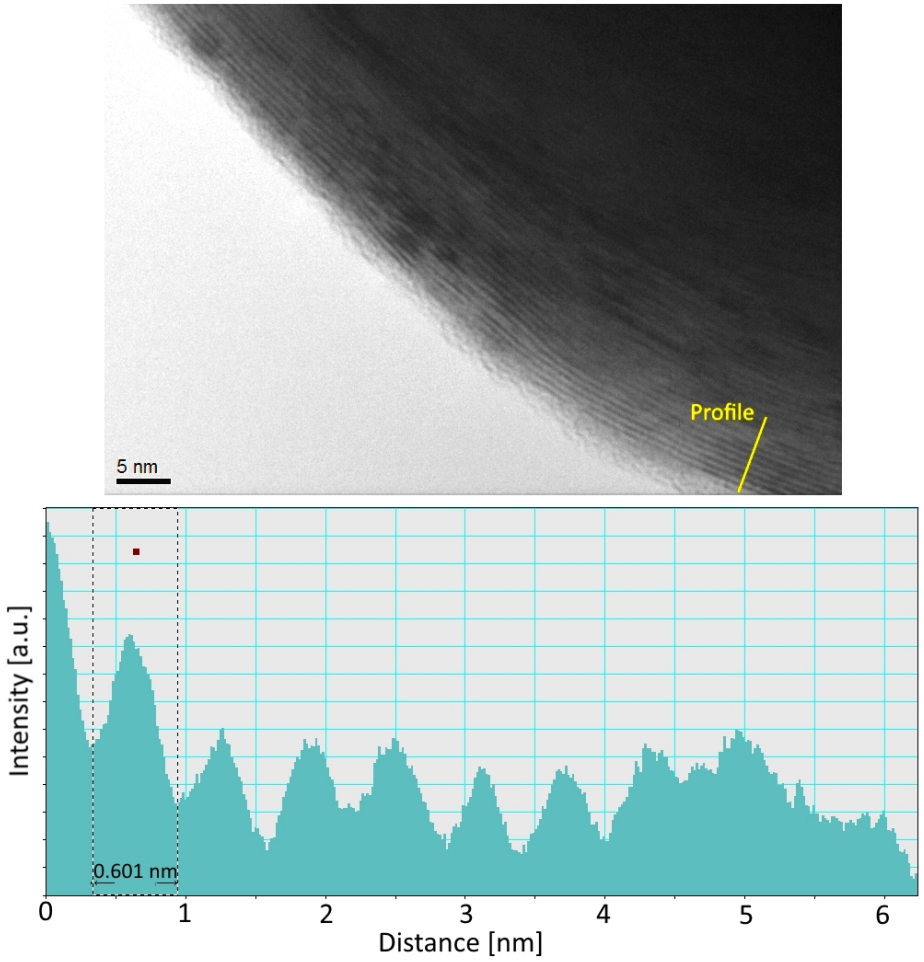

Figure 3.9: *A transmission electron microscopy image showing the layered structure of SnS_2. The observed layer spacings can be used as an initial identification method. SnS_2 has a layer spacing of 0.59 nm, which is in good correspondence with the measured value of 0.601 nm here. Note that the layers follow the topology of the structure and therefore are not straight as one would expect in a rigid crystal lattice.*

SnS_2 Nano-Flowers

Larger, flower-like structures were observed in the synthesised material. The nano-flower-type morphology, as also described in Ke et al. [2009], consisted of large, microscopic structures, typically spheroids or ovoids. The synthesis performed by Ke et al., which differed in the initial reactants compared to those used in this project, used additives in the form of surfactants to promote nano-flower production. No additives were used during this project and possible contamination from leeching elements from the autoclave walls was excluded by re-drilling the entire set-up at

the beginning of the project to ensure clean surfaces. The produced nano-flowers varied from just 800 nm up to several micrometres in diameter and were of much lower density compared to bulk material due to their petal-like sheets. Even though the petals seemed to intersect only rarely, the appearance was that they shared a common origin in the centre of the structure, or a common axis in the case of ovoids. A representative nano-flower grown during this project is shown in Figure 3.10. Here, a single nano-flower can be seen in the centre of the image. As typical for this morphology, the diameter is upwards of 1200 nm. The flower is resting on a layer of flower-like SnS_2 nano-sheets, which will be described later. The higher position of the nano-flower accounts for the increase of intensity. TEM images, such as the image presented in Figure 3.11, were taken to investigate the internal structure of these particles, but they proved to be too thick to resolve sufficiently under the TEM.

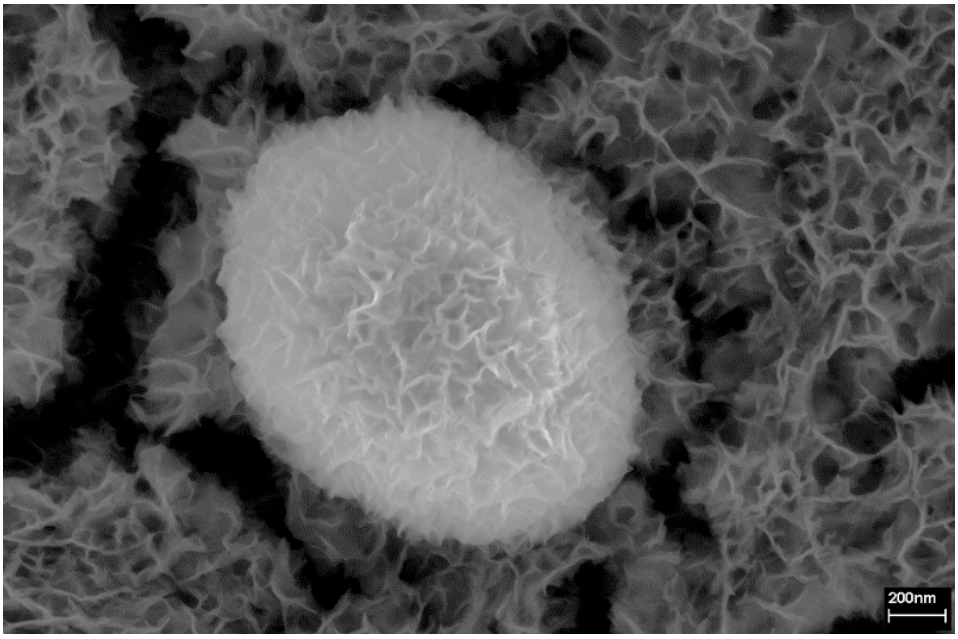

Figure 3.10: *Image of a typical SnS_2 nano-flower. Specimens can grow to be several micrometres across and can have varying petal density, this case being an example for a very high density.*

The synthesis parameters used for the production of SnS_2 nano-flowers are summarized in Table 3.2. These parameters vary from the standard procedure (see Table 3.1) only in terms of a longer dwell time, which has been increased from 10 to 15 hours, and a higher dwell temperature of 200°C instead of the previously used 70°C, which seemed to promote the development of these larger structures.

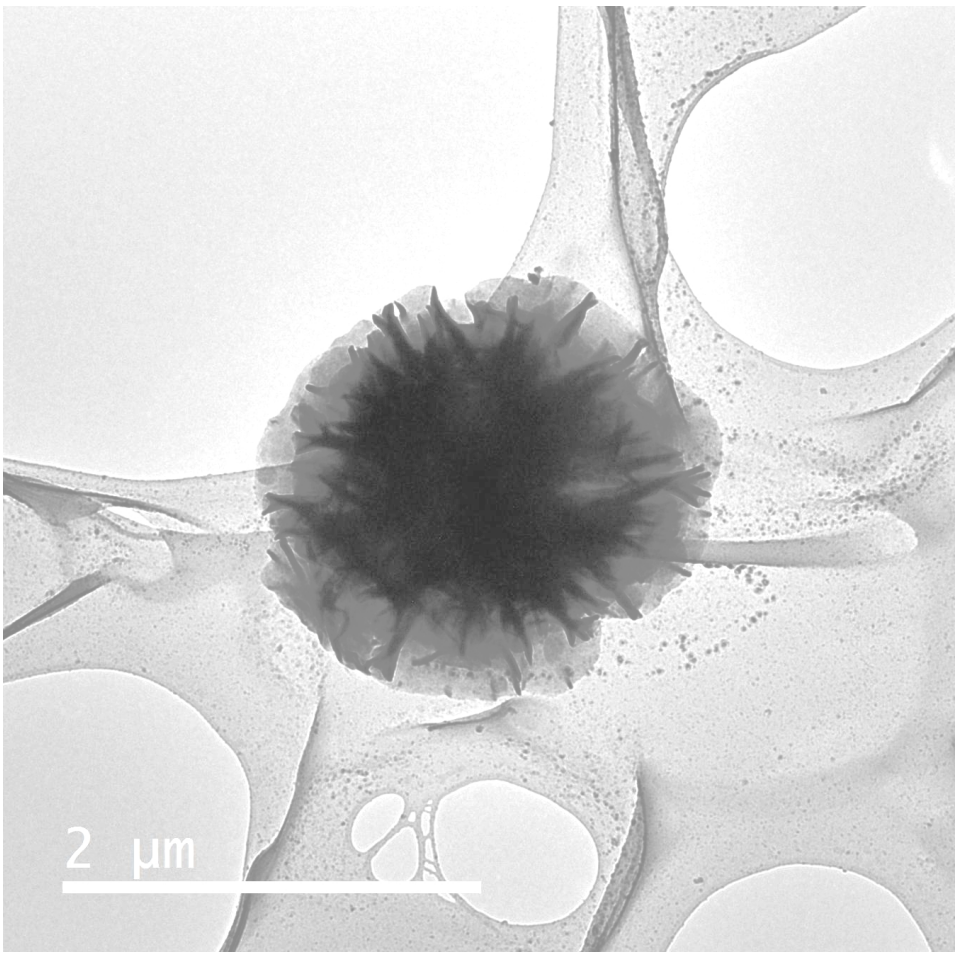

Figure 3.11: *This image shows a single SnS_2 nano-flower particle. As these particles are relatively large, around 2 µm in this case, imaging of their interior structure is not possible.*

A brief study into the growth mechanism of nano-flowers was conducted to verify the growth mechanism detailed in Liu et al. [2010a], but the obtained data in this project wasn't conclusive enough to confirm their results. Liu et al. proposed that nano-flower growth occurs in three separate stages. A first growth of solid nucleation cores is followed by a stage of secondary, petal-producing growth. During the third stage, aggregated nano-flowers increase in size and separate. During the experiments conducted in the scope of this project, no solid nucleation cores were observed and separation of fully grown nano-flowers was often also not seen.

Parameter Name	Parameter Value
Mass of Thioacetamide	90mg
Mass of Tin(IV) chloride hyd.	190mg
Volume of Ethanol	40ml
Dwell Temperature	200°C
Temperature ramp rate	5°C per minute
Dwell Time	15 hours
Pressure inside the autoclave	≈ 31 bar
Precipitate colour	Orange-Brown
Number of washing cycles with pure Ethanol	4 cycles
Drying Temperature	60°C
Drying Time	4-6 hours
Final Yield	30-35mg

Table 3.2: *A typical synthesis set-up for the production of nano-flowers. Note that in comparison to Table 3.1, the dwell time was increased to 15 hours and the dwell temperature had been raised to 200° C.*

As nano-flowers had already been investigated in detail in the literature, both in terms of their morphology [Ke et al. [2009]] and their lithium ion storage capacities [Liu et al. [2010a]], they were not at the focus of this project and instead served as a control system.

Thin-Type Nano-Worms

Two types of worm-like SnS_2 nano-structures could be found in the SnS_2 samples. The first of these were long, thin structures, composed of stacked sheets of SnS_2. Each sheet had a similar shape to either a 3D Gaussian distribution or a spherical section and had a diameter between 200 nm and 600 nm (see Figure 3.13 and Figure 3.16) The sheets demonstrated a high degree of homogeneity in terms of their shape and dimension. The stacking seemed to follow a coaxial system and any curvature in the overall nano-worm seemed to be caused by a smooth bending of the structure. In none of the examined samples was it possible to find intact nano-worms that contained kinks. Branching between thin nano-worms was also not visible (see Figure 3.12 and Figure 3.13 for reference). The length of each nano-worm was different and could vary from as low as several hundreds of nanometres

up to several micrometres. A sample containing thin-type nano-worms is shown in Figure 3.12.

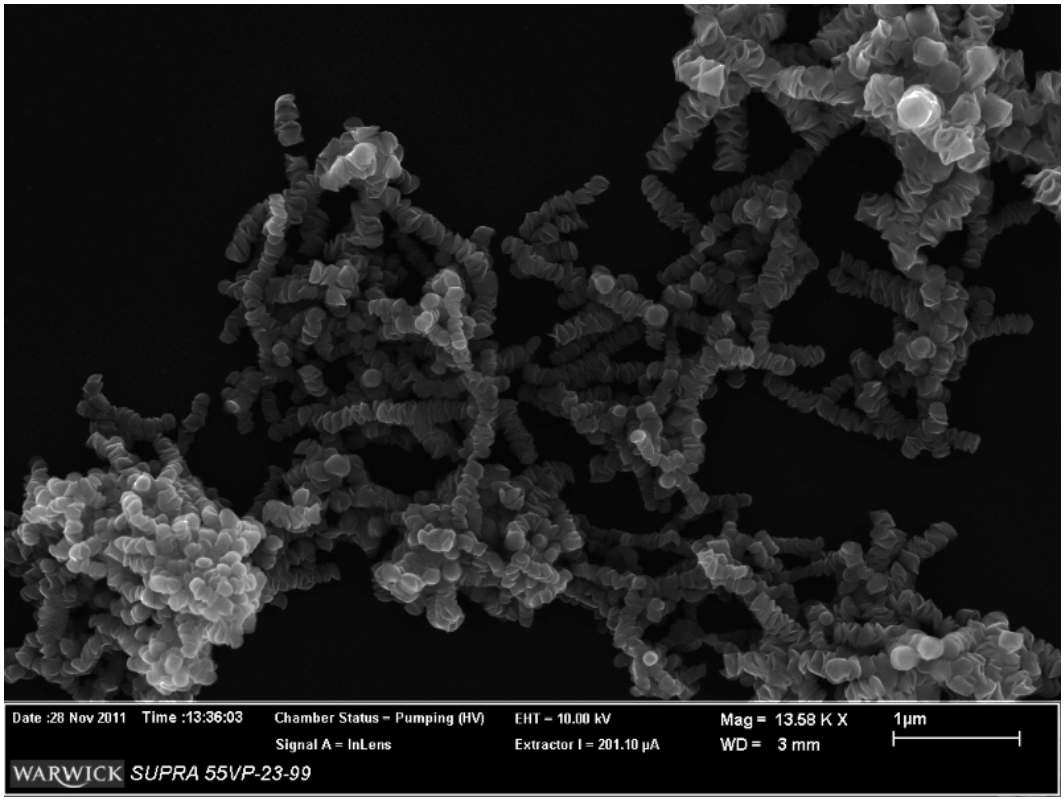

Figure 3.12: *A synthesised sample of SnS_2 containing a large amount of thin-type nano-worms. Nano-worm lengths varied heavily throughout the sample, while diameters ranged from around 200 nm to 300 nm.*

TEM images were very valuable in investigating the interior of the nano-worm morphology. As can be seen in Figure 3.13, the think-type nano-worms have a solid interior free from holes and gaps. However, this also made a direct resolution of the interior difficult under the TEM. In the following discussions, FIB (Focused Ion Beam) techniques were considered, but not pursued further as there were concerns with altering the structure, breaking of delicate features and and general contamination via re-deposition of material. Instead, in separate discussions with microtomy experts, a possible route via microtomy was explored. However, in a short lab experiment, the resin had difficulty in penetrating all the gaps and therefore wouldn't have helped with the support of the delicate nano-worms, making microtomy also unsuitable.

The synthesis parameters for this type of morphology are summarised in

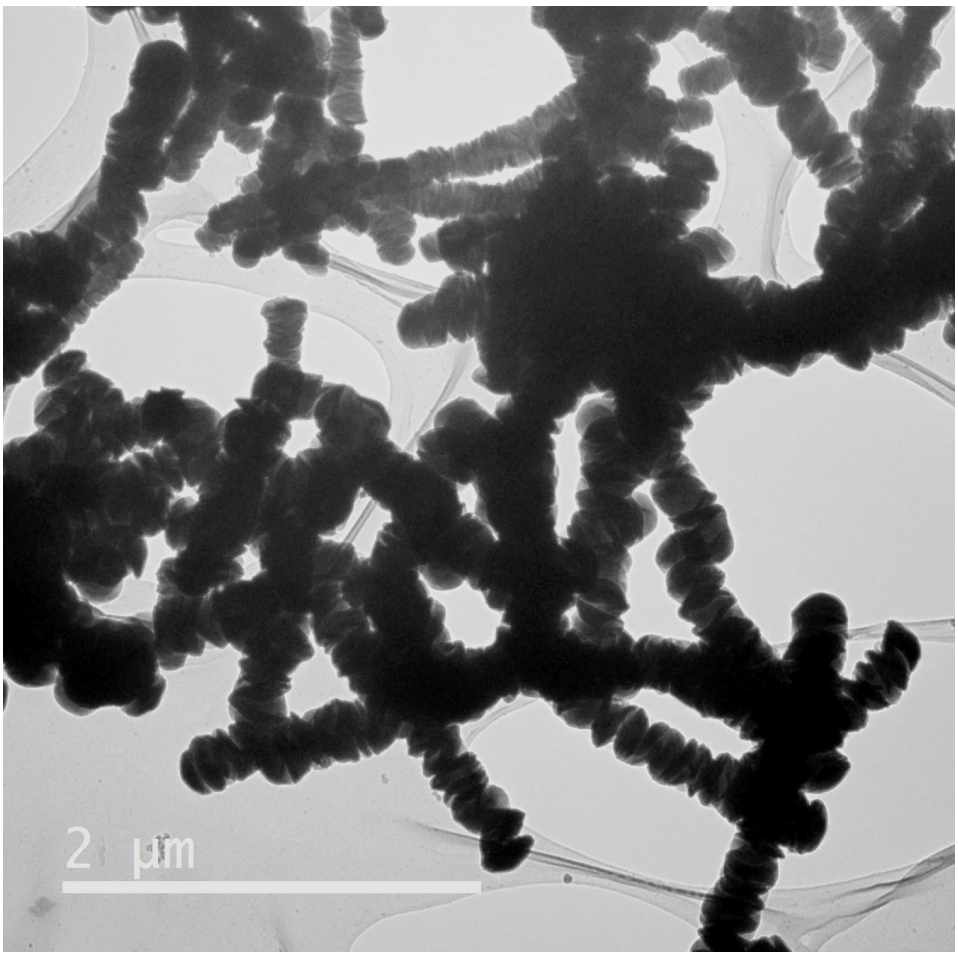

Figure 3.13: *A TEM image showing a cluster of thin-type nano-worms. These structures were dense with few openings within the worms themselves. This is in strong contrast to a second type of nano-worm introduced later.*

Table 3.1, which were the standard parameters laid out previously, as the nano-worms were the central morphology of the investigation. It should be noted that the dwell time had an impact on the equilibrium between thin- and thick-type nano-worms, as longer dwell times favoured the thicker-type worms. This was shown using a short growth study later in the chapter (see Section 3.3.3).

As all other encountered morphologies, apart from the thick- and thin-type nano-worms, have already been investigated in the literature in terms of their physical characterisation and lithium ion storage, the project was focused on these two new nano-structures. Due to their wire-like shape, it was believed that these nano-worms would have enhanced connectivity properties within electrodes, while benefitting from resistance to volume changes due to their ability to grow and shrink

effectively. They also provide a theoretically higher packing ratio than the nano-flowers due to their geometry.

Thick-Type Nano-Worms

The main difference of this morphology to the thin-type worms came in the form of the dimensions. While thin-type worms had a diameter between 200 and 600 nm, thick-type worms could achieve diameters bigger than 600 nm to well above 1 μm, usually in the range of 1 to 2 μm. Their component sheets, while still displaying a high degree of homogeneity in terms of stacking and size, were no longer simple caps, but demonstrated a wave-like behaviour. The amplitude of the waves increased the further one moved away from the centre of the sheet. As with the thin-type nano-worms, these structures tended to be quite long and often reached several micrometres in length. A sample image of such a structure can be seen in Figure 3.14 using the SEM and an image obtained via STEM bright and dark field is shown in Figure 3.15.

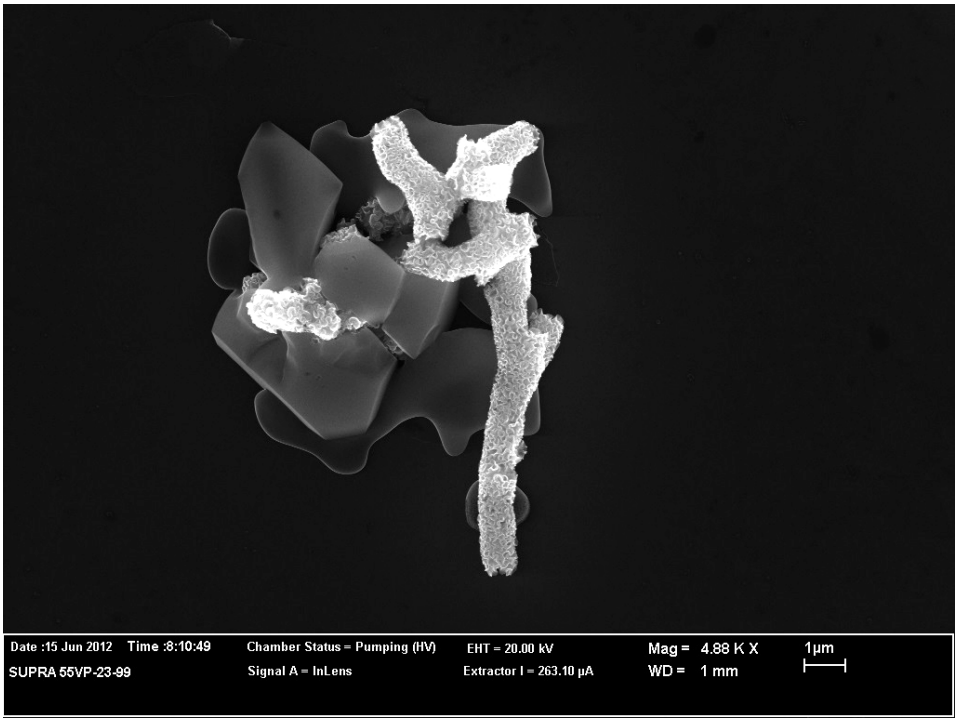

Figure 3.14: *Examples of the thick-type nano-worm morphology. The worms demonstrated homogeneous diameters of around 1 micrometre, and varied in length. The contaminating materials could be attributed to remaining reaction by-products in the sample dispersion.*

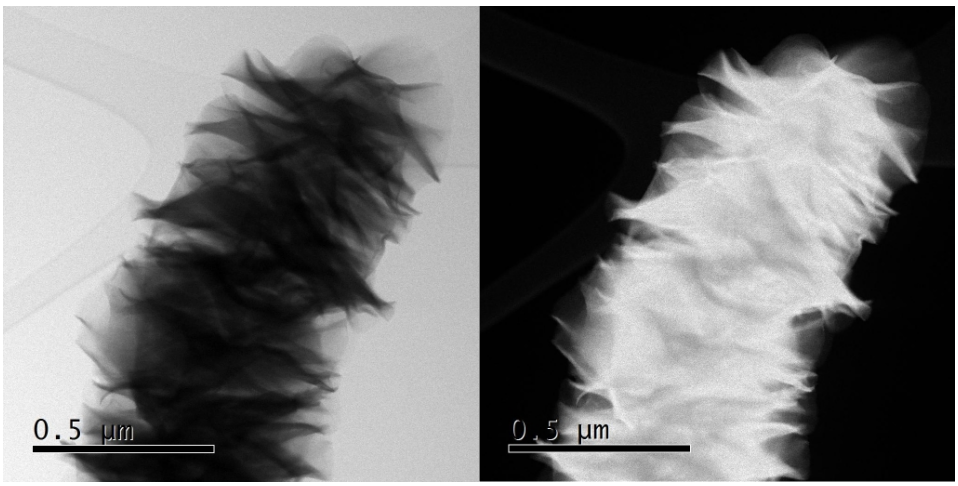

Figure 3.15: *A bright and dark field image of a thick-type SnS_2 nano-worm. The nano-worm has a diameter of roughly 600 nm.*

As mentioned above, the occurrence of this morphology was in combination with thin-type nano-worms and synthesis conditions and parameters were very similar. A shift in the ratio between thin- and thick-type nano-worms could be achieved via a variation in dwell time, as an increase in dwell time led to a favouring of the thick-type morphology. It should be noted, however, that a complete suppression of the production of thin-type nano-worms could not be achieved this way. The summary of the synthesis conditions are listed in Table 3.3. Since, as previously mentioned, the nano-worm morphology is a novel discovery, no previous literature on the topic exist and therefore couldn't provide possible further routes on how to affect the ratio between both worm types.

SnS_2 Nano-Platelets

As a secondary product of the standard synthesis procedure, often small, single sheets of SnS_2 were encountered. These did not arrange themselves into any particular structure, but formed small chaotic piles in between the main, larger structures or along the edges of bigger clusters instead. They were generally shaped in the form of segments of thin-type worms, with diameters of a few 100 nm. They showed the characteristic dome-like shape encountered in some of the other morphologies, with dome heights varying from nearly flat to in between 50 nm to 100 nm, as can be seen in Figure 3.16. It was possible to measure the outer dimensions of these structures via SEM, as these particles often got stuck on their side between bigger particles, making a direct measurement of both diameter and height possible. The platelets

Parameter Name	Parameter Value
Mass of Thioacetamide	90mg
Mass of Tin(IV) chloride hyd.	190mg
Volume of Ethanol	40ml
Dwell Temperature	70°C
Temperature ramp rate	5°C per minute
Dwell Time	15 hours
Pressure inside the autoclave	≈ 1.9 bar
Precipitate colour	Orange-Brown
Number of washing cycles with pure Ethanol	4 cycles
Drying Temperature	60°C
Drying Time	4-6 hours
Final Yield	30-35mg

Table 3.3: *A typical synthesis set-up for the production of thick-type nano-worms.*

were observed in all samples as a minor side-product. Conditions that correspond to the synthesis yielding visible concentrations of these are given in Table 3.4.

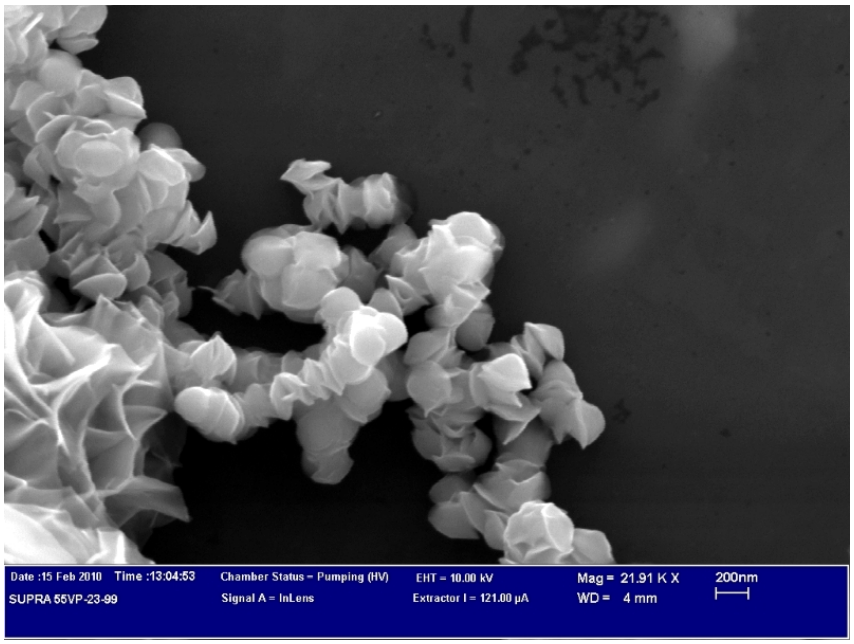

Figure 3.16: *Examples of the SnS_2 nano-platelet morphology. Particle diameters ranged from 200 nm to 250 nm. The platelets were usually found near the edge of larger structures, in this case a large SnS_2 nano-flower in the bottom left hand corner of the image.*

Parameter Name	Parameter Value
Mass of Thioacetamide	90mg
Mass of Tin(IV) chloride hyd.	190mg
Volume of Ethanol	40ml
Dwell Temperature	70-200°C
Temperature ramp rate	5°C per minute
Dwell Time	10-15 hours
Pressure inside the autoclave	≈ 1.9 - 31 bar
Precipitate colour	Orange-Brown
Number of washing cycles with pure Ethanol	4 cycles
Drying Temperature	60°C
Drying Time	4-6 hours
Final Yield	Undetermined due to difficulties in obtaining a pure sample.

Table 3.4: *Synthesis conditions which produced the nano-platelet morphology. Nano-platelets seemed to be a secondary product in all performed syntheses and their synthesis parameters covered a large range of values.*

SnS_2 Flower-Type Sheets

As the yield of each synthesis of SnS_2 was relatively low, a stockpile of samples was produced and stored in ethanol to allow quick access to larger quantities of the sample material. When flower-type SnS_2 was stored this way in glass sample vials, the vials were covered by a transparent yellow-orange coating from the inside. The process was slow, taking several weeks/months to produce a visible coating (with a more pronounced coating taking longer), with a fine discolouration of the glass being visible after 14 days and a solid, discernible film appearing after 4 weeks (however, depending on the synthesis conditions, this may take up to 12 weeks). To examine this secondary product and to investigate the storage properties of the samples, sections of the coating were carefully floated off the vials and transferred to a silicon substrate. The samples were then examined via SEM, and the coating was found to be of seemingly homogeneous thickness over large sections. The coating itself was composed of structures similar to that observed in SnS_2 nano-flowers, but spread out across the sample substrate as can be seen in Figure 3.17. The observed cracking either resulted from the transfer and drying process, or was caused by

the evaporation of ethanol trapped beneath the sheet during illumination with the electron beam. The overview of the synthesis conditions for this type of morphology can be seen in Table 3.5.

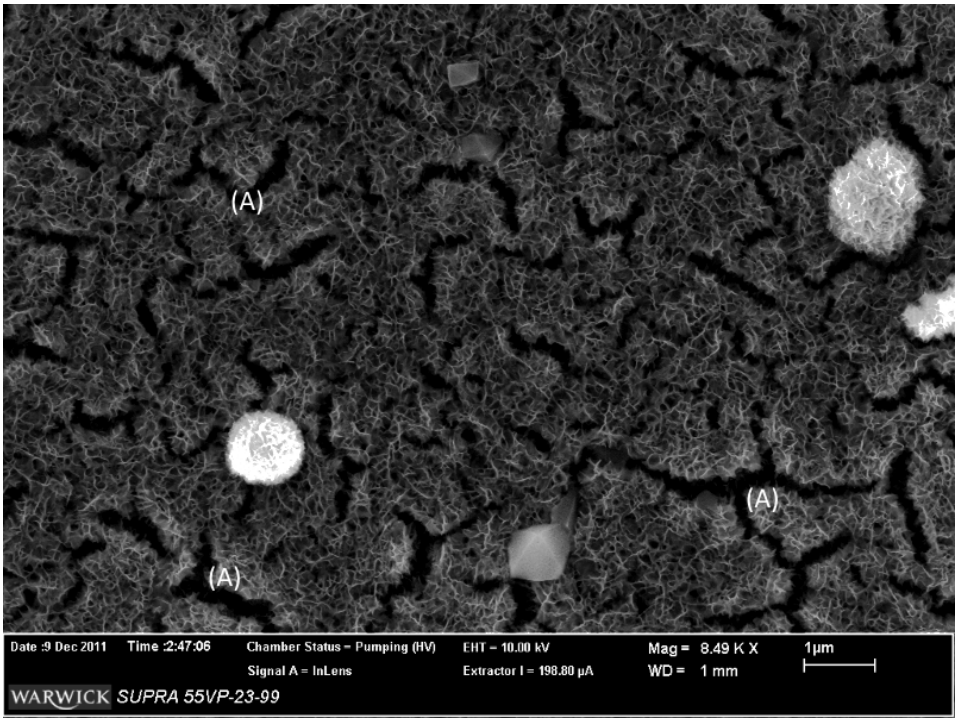

Figure 3.17: *A cracked (see (A) for examples of such cracks) SnS_2 sheet on a silicon wafer substrate. The structure of the cracks suggested the cause to be contraction during the drying process. A few SnS_2 nano-flowers can be seen resting on top of the film. The homogeneous contrast suggested a relatively similar thickness of the film throughout, but unfortunately no direct measurement of this thickness was possible in these images, as attempts to align the film correctly for such a measurement did not succeed.*

A higher magnification image can be seen in Figure 3.10, where the described nano-flower sits on a sheet as shown in Figure 3.17, highlighting the similarities between the two morphologies.

An attempt was made to grow these sheets directly onto a substrate. Two different types of material were investigated for this reason. First, a glass slide was introduced into the reaction chamber during a typical synthesis. While a small amount of coating growth was indeed noted (see Figure 3.18), it proved to be an inefficient method, as the majority of the material remained in the autoclave. Second, an attempt was made to grow the sheets directly onto copper foil in order to

Parameter Name	Parameter Value
Mass of Thioacetamide	90mg
Mass of Tin(IV) chloride hyd.	190mg
Volume of Ethanol	40ml
Dwell Temperature	Room Temperature
Dwell Time	7 - 70 days
Pressure inside the autoclave	$\approx$ 1 bar
Precipitate colour	Orange-Brown
Number of washing cycles with pure Ethanol	4 cycles
Drying Temperature	60°C
Drying Time	4-6 hours
Special Conditions	Stored in ethanol for prolonged period of time (1-10 weeks)
Final Yield	Highly variable. Very low for the recovery of large sheets, but could reach up to 30mg if the sheet was broken into little segments to peel it off the glass.

Table 3.5: *The synthesis parameters for the unaided growth of the flower-type sheet nano-structure. Samples were produced over several weeks and stored in sealed containers.*

create an easy route towards electrode production and enhanced adhesion properties. While a certain growth did occur, the sheets were heavily contaminated with copper due to the strong reaction between the copper substrate and dihydrogen sulfide. The resulting electrodes had a bluish hue indicative of copper sulfide and not the desired yellow-brown colour of SnS_2.

3.3.2 Statistical Particle Size Analysis

To further investigate the morphological properties of the synthesised structures, particle size analyses were carried out. As SnS_2 nano-flowers [Liu et al. [2010a]] and nano-platelets [Kim et al. [2007]] had already been characterised by other researchers, and being faced with difficulties of severe cracking of the nano-sheet samples, the decision was made to focus efforts on the characterisation of the nano-worm morphologies, which had already been chosen as the main objective of this project. For this reason, a series of SEM micrographs were prepared from samples grown under standard synthesis parameters (see Table 3.1). The samples were dispersed in ethanol and cast onto silicon wafer shards, which were chosen as sample substrate

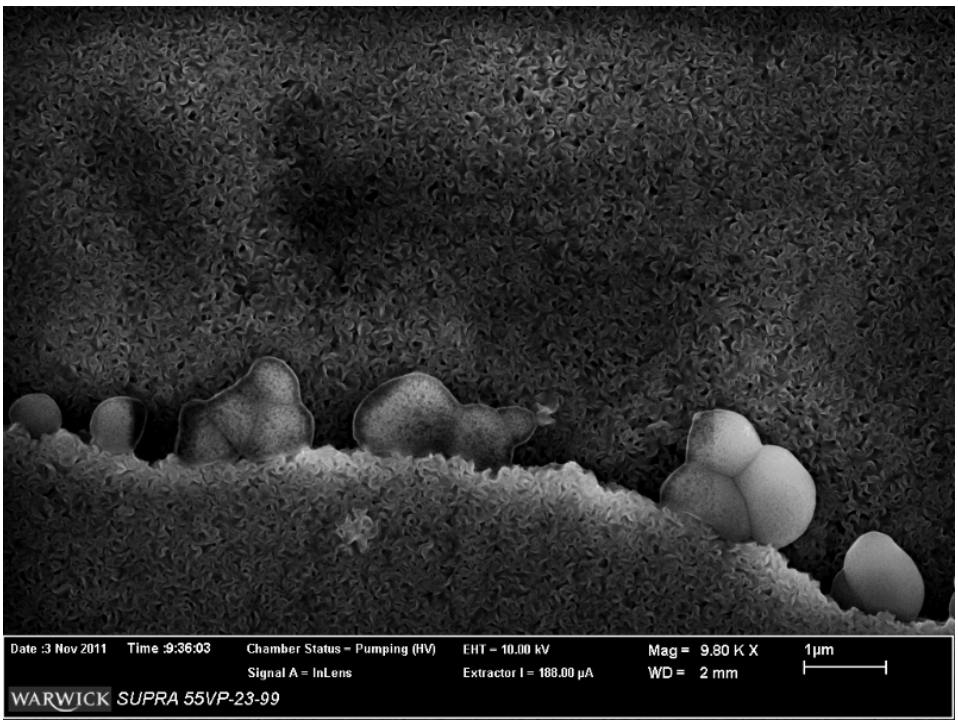

Figure 3.18: *SnS_2 flower-type sheets as grown directly onto glass and then transferred to the SEM. As cracks occurred during the transfer to the SEM, overlapping of sheets was common. The varying contrast as seen in the background sheet suggested the presence of ethanol trapped beneath the sheet, although it withstood illumination with the beam. The bubbles that can be seen along the edge of the sheet are also caused by the trapping of ethanol. When illuminated with the beam, the ethanol evaporates and the bubbles shrink away.*

because of their flatness.

All taken micrographs were checked for flat-lying nano-worms, which were then measured in terms of their length and diameter. The study had to be carried out by hand due to the complex nature of the particles and as common particle recognition software, such as plug-ins for the GATAN Digital Micrograph software, were unable to discern separate particles or produced unreliable results. By dispersing nano-worms very thinly on a silicon wafer, it was possible to count single, flat-lying worms. The dispersing process reduced the development of clusters and dislodged intertwined nano-worms, although it wasn't possible to remove all clusters (as can be seen in Figure 3.19). Branching of worms was not observed.

In total, over 400 different nano-worms were examined by hand and the results recorded. The results of this study are presented in Figure 3.20 and Figure 3.21 as histograms.

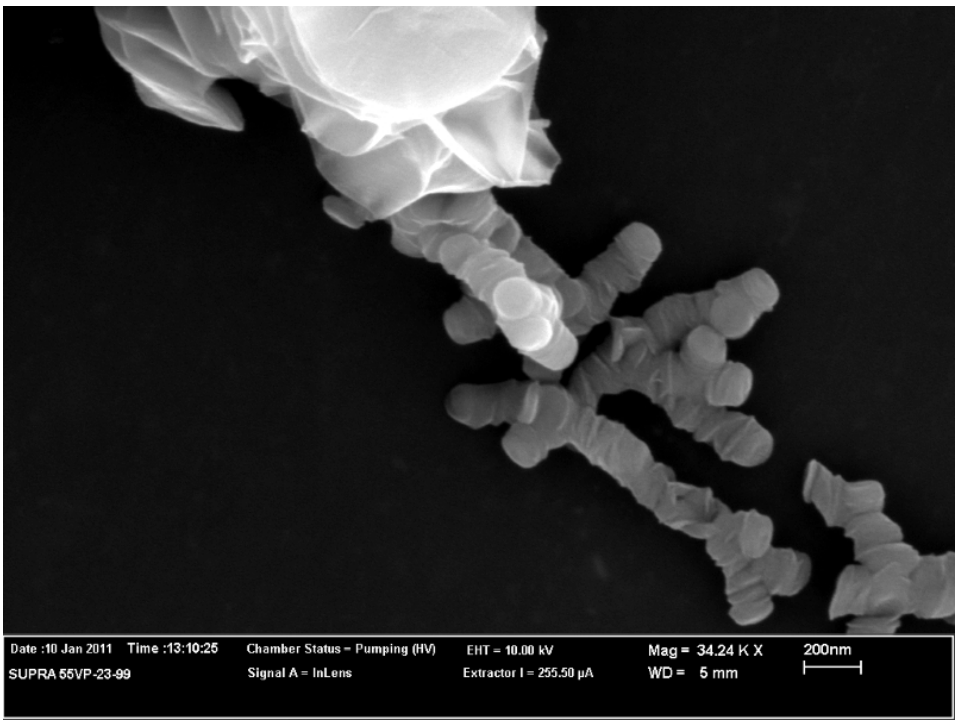

Figure 3.19: *A sample of dispersed SnS_2 nano-worms on silicon. A common difficulty was the eagerness of the particles to clump together even at low concentrations and during slow drying processes.*

The analysis of lengths showed that they followed a heavy-tailed quasi-Gaussian distribution for the synthesis parameters laid out in Table 3.1. The mean length λ_{Length} and its standard deviation σ_{Length} were:

$$\lambda_{Length} = 1124nm \tag{3.9}$$

$$\sigma_{Length} = 352nm \tag{3.10}$$

Similarly, the distribution of diameters also had a heavy-tailed quasi-Gaussian shape with a mean diameter $\lambda_{Diam.}$ and its standard deviation $\sigma_{Diam.}$ of:

$$\lambda_{Diam.} = 226nm \tag{3.11}$$

$$\sigma_{Diam.} = 44nm \tag{3.12}$$

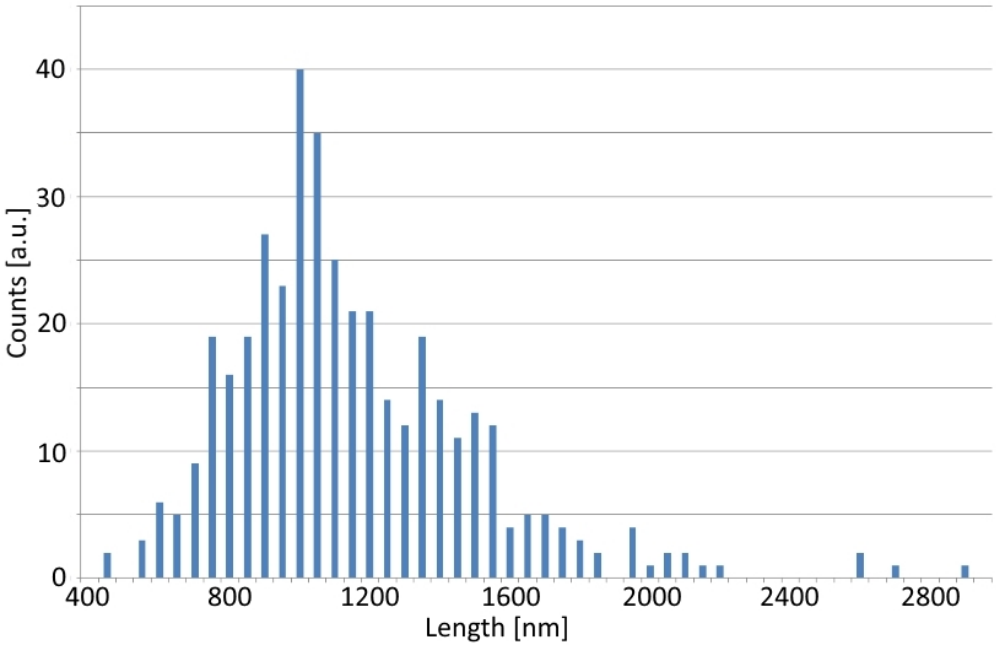

Figure 3.20: *Distribution of lengths of 404 measured nano-worms. As can be seen, the distribution is non-uniform and heavy-tailed quasi-Gaussian.*

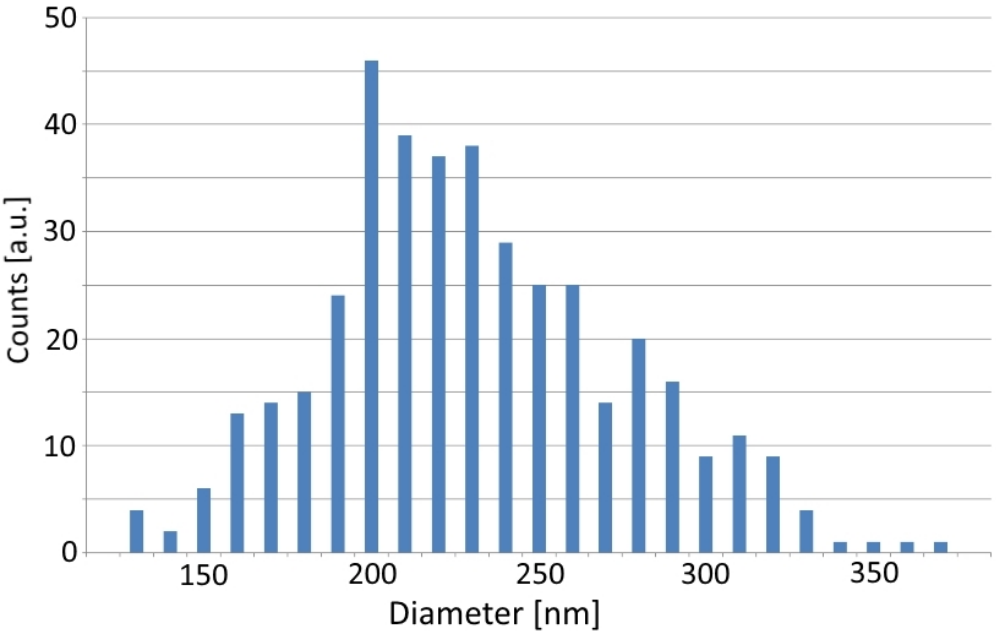

Figure 3.21: *Distribution of diameters of 404 nano-worms. Again, the distribution is non-uniform and heavy-tailed quasi-Gaussian.*

In order to get a sense of the actual particle volume, measured lengths and diameters were combined and the volume of each nano-worm calculated using these values. The results are shown in Figure 3.22. It has to be noted that the calculated volume corresponded to the cylindrical volume enclosing the nano-worm and not the volume taken up by the material composing the structure.

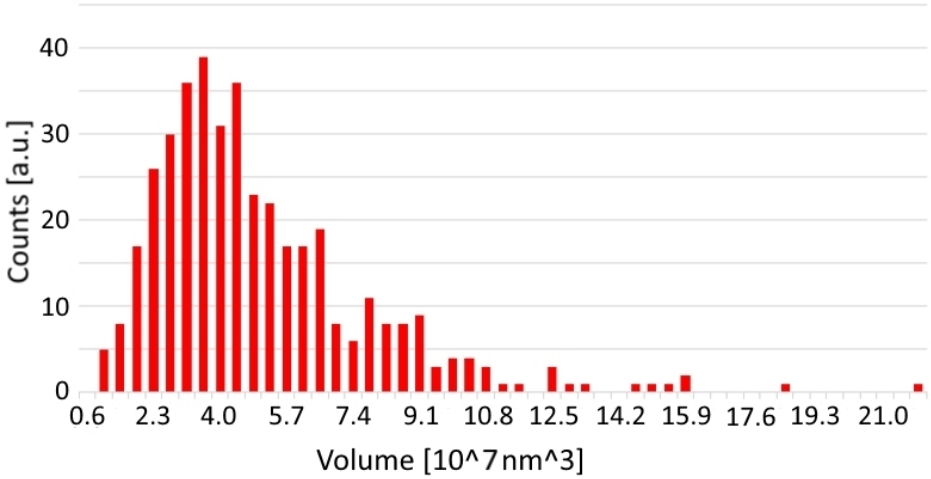

Figure 3.22: *The enclosing volume was calculated for each measured nano-worm. As expected, based on the data obtained for length and diameter, the distribution was again of a heavy-tailed quasi-Gaussian shape.*

As expected, the distribution of the calculated volumes was also of heavy-tailed, quasi-Gaussian nature with a mean volume λ_{Volume} and its standard deviation σ_{Volume} of:

$$\lambda_{Volume} = 4.8 * 10^7 nm^3 \tag{3.13}$$

$$\sigma_{Volume} = 2.8 * 10^7 nm^3 \tag{3.14}$$

These values could have been used to calculate the geometric outer surface area to volume ratio for an average nano-worm, but it is the actual surface area of the nano-worm, which is of interest in regard to a large number of physical properties, such as catalytic or electrochemical properties. However, due to the complex nature of the morphology, it wasn't possible to calculate the total surface area of the nano-worm just by means of SEM imaging. Therefore, an attempt to approximate this ratio was made using computer simulations and will be discussed in a later section (see Section 3.4).

3.3.3 Growth Study of the Formation of Nano-Worms

To better understand the processes behind the formation of the nano-worm morphology, a timed trial was used to investigate the growth mechanism. A sample was prepared using the standard reactant ratios as laid out in Table 3.1. As performing the synthesis at elevated temperature in an autoclave would have led to difficulties in probing the reactant solution, an experiment at room temperature was devised instead. Once every day, a small amount of the contents of the reaction vessel was removed and dried under vacuum. It was then examined under the SEM and the resulting series of images were compared to one another.

After one day of resting, the solution had not yet produced the usual yellow-brown colour and no solid precipitate could be found. When examining the dried solution under the SEM, it was possible to discern elongated thin structures as visible in Figure 3.23, some of which reached lengths of up to 2 microns.

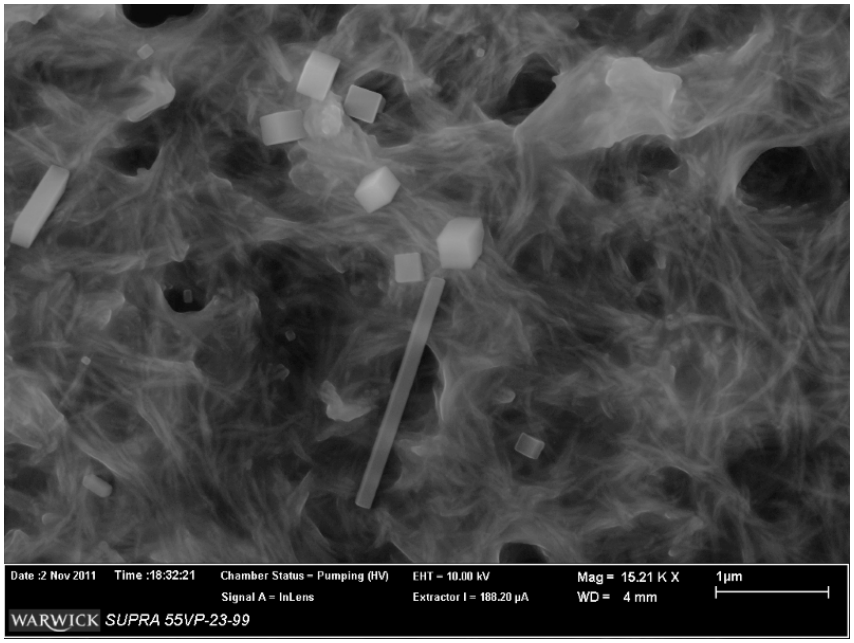

Figure 3.23: *A SEM image of the dried sample of the reaction solution after the first day. A large number of long and thin structures is visible in the image. Additionally, long, cuboid structures can be seen in the image, which are caused by the remaining initial reactants.*

Unfortunately, a high level of contamination could not be avoided, as the nature of the sample did not allow for an effective washing process. This was due to the thin particles being too small to be effectively retained even with nano-

pore filters during the washing process. The observed early formation of long axial structures suggested a primary growth along the axis of the nano-worm.

After leaving the solution to react at room temperature for 4 days, a light, yellow-brown precipitate was visible. Imaging under the SEM, as can be seen in Figure 3.24, revealed the presence of formed worm-like structures, which had shape, length and diameter consistent with thin-type nano-worms. Therefore, this suggested a change from an axial growth to radial growth, which caused an increase of diameter of the particles. Unfortunately, the cleaning cycle still proved to be ineffective and, if conducted, led to a high loss in sample material. The length and flatness of the visible structures suggested that the initial growth had indeed occurred preferentially in axial and not radial direction. Noteworthy was also that the length of the present structures had not significantly increased compared to those observed in the 1-day reaction time sample.

After 7 days, SEM imaging showed that the sample was composed of the usually encountered thin-type nano-worm morphology (see Figure 3.25). The sediment had the expected yellow-brown colour and it was possible to carry out the washing cycles as usual. Noteworthy was the high homogeneity of the sample and without any significant presence of any other competing morphologies.

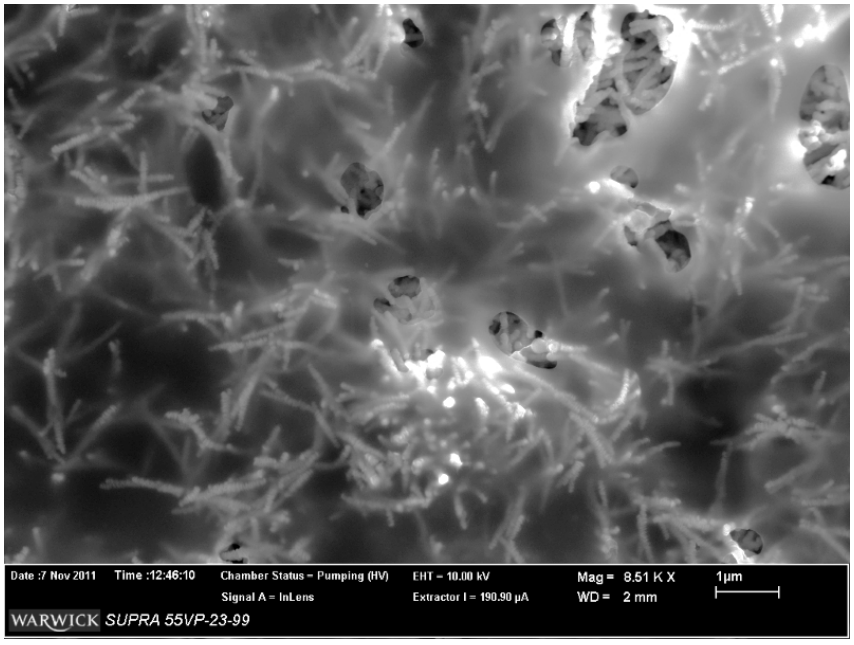

Figure 3.24: *A SEM image of the sample after allowing the reaction to take place over the course of 4 days at room temperature. As the cleaning cycle was too wasteful, only light contamination removal was possible.*

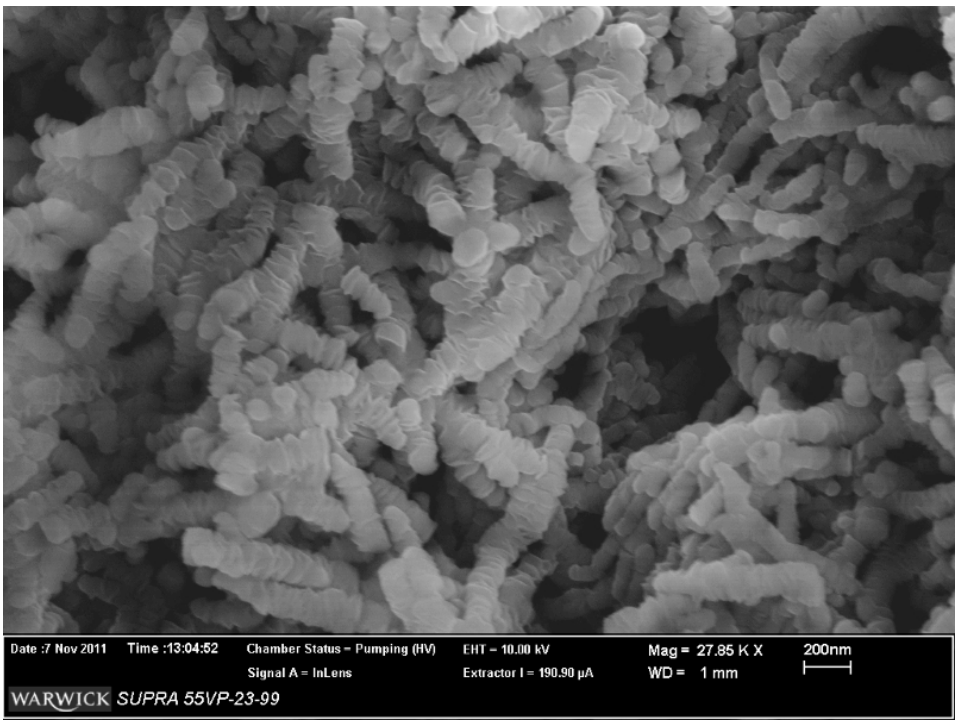

Figure 3.25: *The dried sample, as seen under the SEM, after allowing the reaction to run for 7 days at room temperature. The common nano-worm morphology is now clearly present.*

After 13 days, as can be seen in Figure 3.26, the nano-worms had gained in diameter, but not discernibly in length. The most obvious change occurred in the overall shape of the nano-worms, as can be seen by comparison between the appearance of the nano-worms in Figure 3.25, where the nano-worm perimeters are flat with a circular circumference, and Figure 3.26, where the perimeters show the characteristic frills of the thick nano-worms. In particular the onset of the development of the frill-like structures in nano-worms belonging to the thin-type category strongly suggested a link between the two nano-worms.

Therefore, the study showed that the growth of thin- and thick-type nano-worm morphologies was linked to one another. The initial growth occurred axially through the creation of a thin precursor, which reached lengths of up to 2 microns. Over the next days, these precursors grew in diameter as the continued synthesis caused the creation of additional SnS_2. After 7 days, they took the shape of the usual thin-type nano-worms as encountered after the typical synthesis (as can be seen in Table 3.1). These then slowly grew further in diameter, but under the creation of the frilly outer perimeter encountered in thick-type nano-worms. As these samples

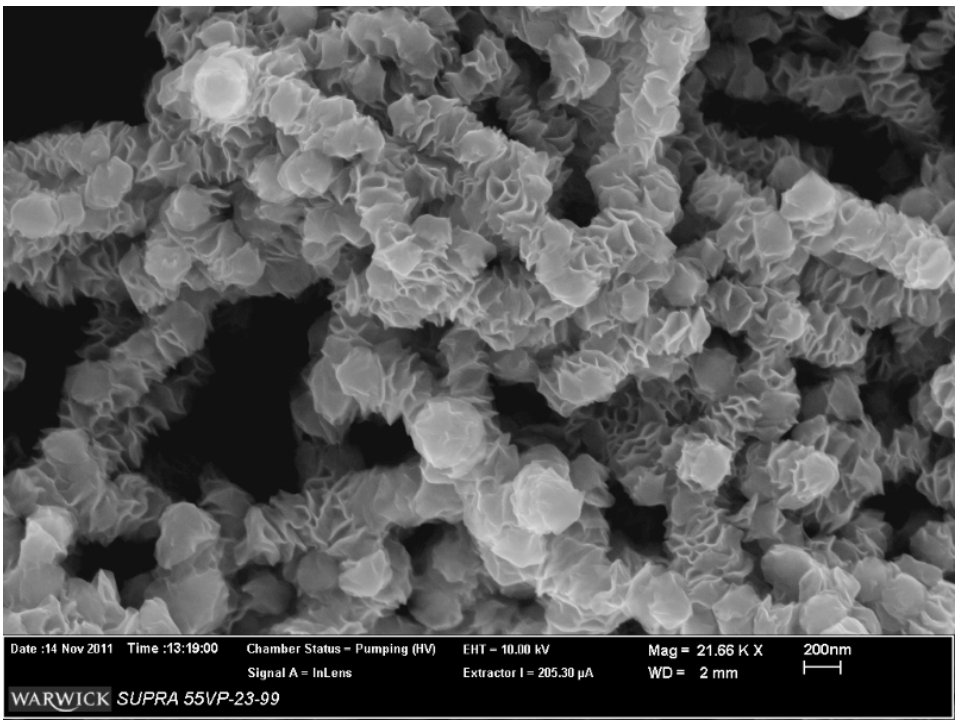

Figure 3.26: *A SEM image of the washed reaction products taken after 13 days of reaction time.*

grew at room temperature, it should be noted that under higher temperatures, the creation of, and transition between, the nano-worm morphologies would have occurred at a higher speed.

3.3.4 3D Morphological Analysis via Electron Tomography

To further deepen the understanding of the 3D set-up of the worm-type morphologies, a standard electron tomography investigation was undertaken using a 2100 JEOL transmission electron microscope. The aim was to obtain a 3D computer-reconstructed model based on a series of tilted images of the sample morphology. A series of tilt images were obtained from a thick-type nano-worm using a single tilt holder between the angles of +70 degrees and -70 degrees with a 1 degree step. The resultant 141 HAADF STEM images were then reconstructed using SIRT. Unfortunately, the reconstruction algorithm failed for our nanoarticles, possibly due to the high complexity of the particles.

However, it was decided to further pursue this experiment and to send a set of samples to Prof. Dr. Matthew Weyland at the Monash University in Melbourne, Australia, a well known expert in the field of electron tomography. The sample

sent included three prepared lacey-carbon grids containing thick-type nano-worms at varying particle densities. Prof. Weyland used his expertise to successfully generate 3D representations of the particles. For this, 75 HAADF STEM images were recorded between the angles of +74 degrees and -74 degrees using a 2 degree step on a FEI Titan 'Cubed' 80-300 at 300keV. The algorithms used for the reconstruction were both SIRT (40 iterations) and IBF, as discussed in Chapter 2. The results were a set of ADF electron tomography reconstructions, an example of which is shown in Figure 3.27.

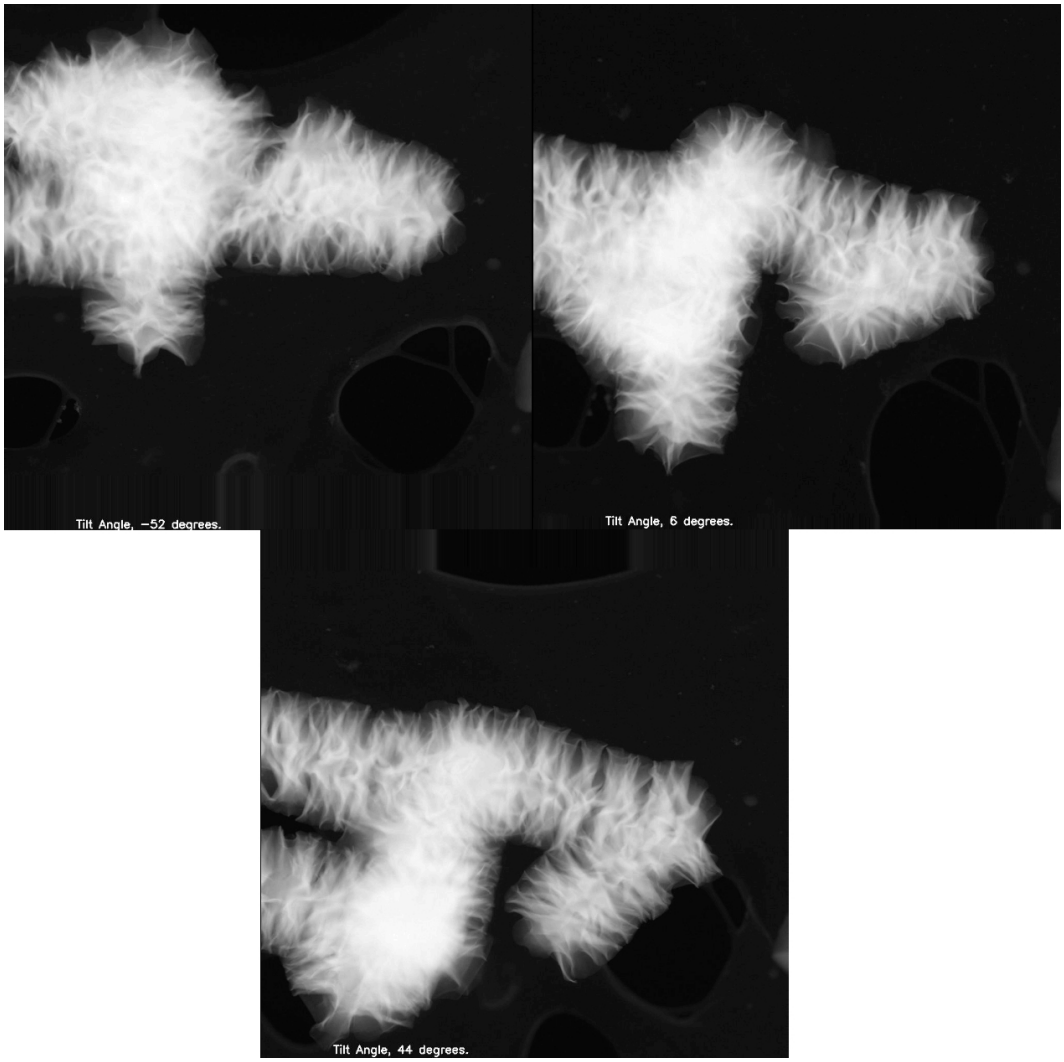

Figure 3.27: *A snapshot of the 3D electron tomography reconstruction of a thick-type SnS_2 nano-worm. The reconstruction was made by Prof. Weyland of Monash University, Australia.*

Annular dark field electron tomography (ADF ET) models were transformed by Prof. Weyland into 3D computer graphical models of the nano-worms. As can be seen in Figure 3.28, each segment was composed of a central, smooth mound, which then flared out into a wave-like skirt around the centre. Furthermore, Figure 3.28 illustrates nicely that the sheets formed a circular cylinder, unlike what had been reported for singular crystalline sheets of SnS_2, which were shown to form hexagonal platelets [Zhai et al. [2011]]. The information gained from these reconstructions was used to refine topological computer models, described in Section 3.4.2. Unfortunately, at the time of writing of this thesis, advanced electron tomography models that allow a slicing and sectioning of the structure to further illuminate the internal structure were still in production and therefore could not be used to calculate the total surface area and investigate the internal structure of the nano-worms.

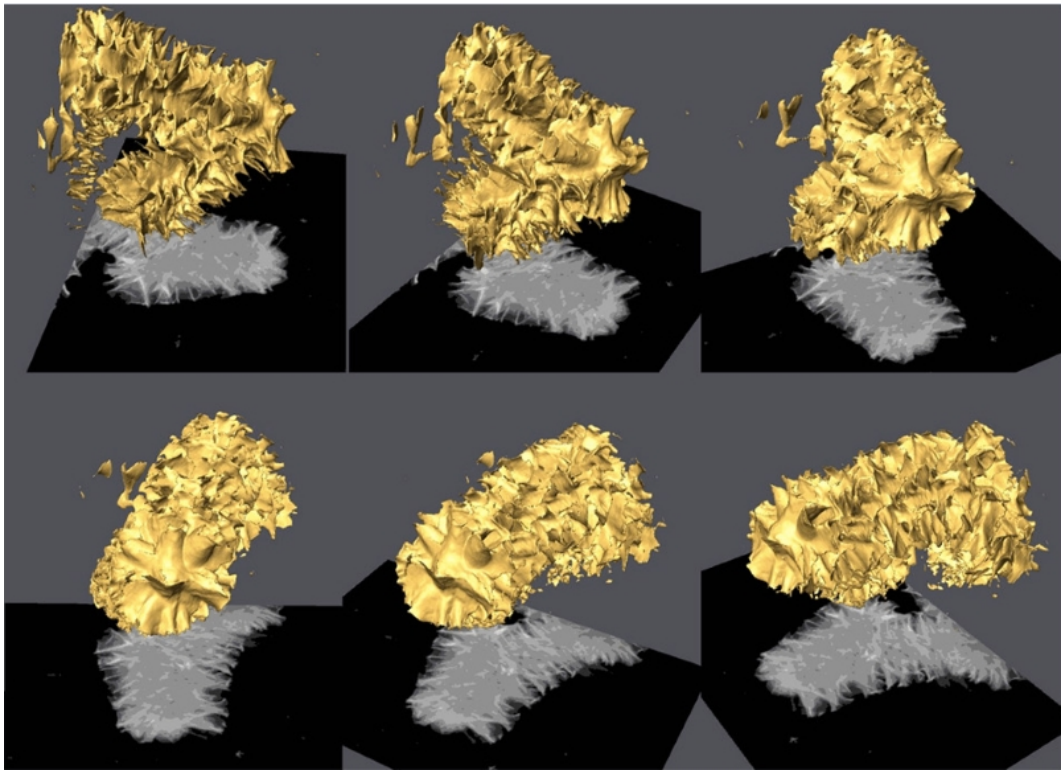

Figure 3.28: *A computer-generated 3D model obtained through electron tomography by Prof. Weyland. The nano-worms formed cylindrical structures, unlike the hexagonal shape reported for singular SnS_2 platelets [Zhai et al. [2011]].*

3.4 Surface Area Determination of SnS_2 Nano-Worms

3.4.1 Surface Area to Volume Ratio Measurement via the Brunauer-Emmett-Teller Method

The next method to determine the surface area of the nano-worm morphology was the Brunauer-Emmett-Teller (BET) method. Since the amount of material synthesised during each synthesis was small, and the error incurred by using BET is inversely linked to the amount of material under investigation, it was necessary to create a sufficiently large stockpile of SnS_2 nano-powder. It was decided to stockpile a total amount of 300 mg of SnS_2, roughly corresponding to 10 synthesis runs. Each batch was independently examined via SEM to ensure that the morphology of the sample was indeed of the worm-type, as seen in Figure 3.29:

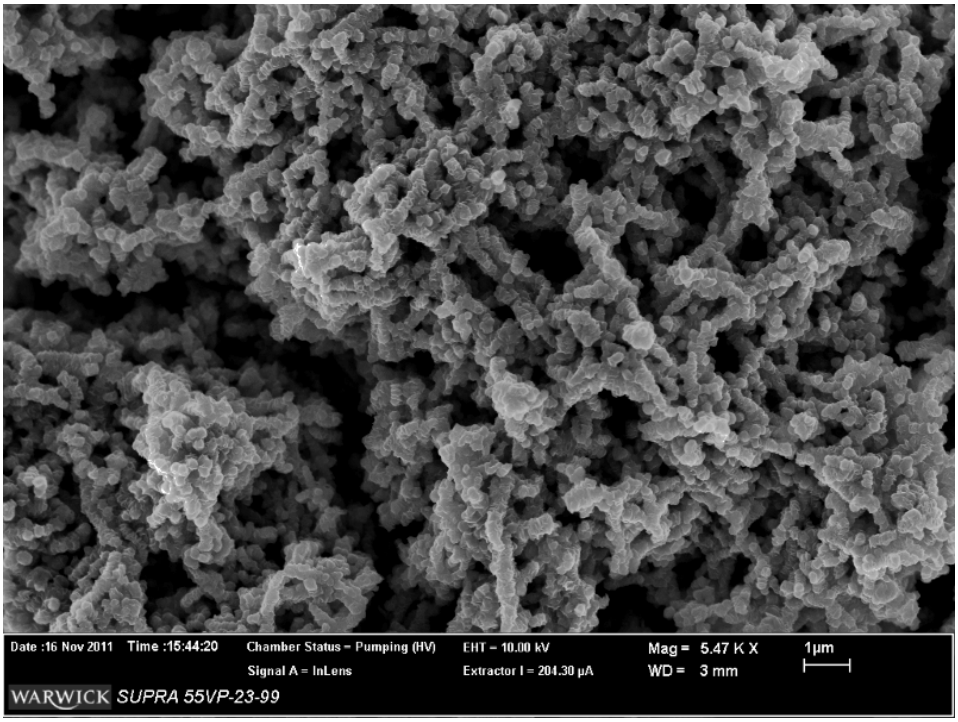

Figure 3.29: *A SEM image representing the morphological composition of the material used in the BET experiments.*

The 10 different batches were washed and combined into a single sample, which was then dried under vacuum at 40°C overnight to remove any remaining volatile contaminants and subsequently subjected to a further decontamination process using liquid helium. Afterwards the helium-cleaned sample was transferred to

the BET measuring apparatus [Micromeritics ASAP 2020 Surface Area and Porosity Analyser]. In order to ensure that each experimental run was performed only on pristine material, each utilized sample was discarded after use.

Upon evaluation of the experimental data obtained through several experiments, it became clear that the material was not suitable for investigation using BET. A sample isotherm collected from the studies is shown in Figure 3.30. As can be observed, the partial pressure plot actually dropped below zero before rising up towards its maximum again. This result would indicate that the sample released, at certain partial pressures, more nitrogen than it had adsorbed, leading to a negative value of adsorbed quantity, which is unphysical. Due to careful cleaning cycles, it was possible to exclude contamination as a possible cause for this and discussions with BET specialists also yielded no satisfactory answer, even when trying to account for micro-pores [Hammond and Conner [2013]]. However, micro-pores had not been observed in the samples via either SEM or TEM. Unfortunately, this phenomenon occurred exactly in the measuring range used for the application of the BET method and thus neither computer- nor man-performed evaluations could provide a sensible value for the surface area that could be linked to observations using other techniques. Despite further efforts to overcome or explain this phenomenon, it was not possible to find a suitable explanation. Consequently, computational methods were chosen to approximate the overall surface area.

3.4.2 Surface Area Modelling of SnS_2 Nano-Worms via Computational Simulation

Atomic Position Approach

The initial approach was to model the structure of SnS_2 nano-worms by looking into specific atomic positions and working up a structural model from there. The basic unit cell for an undisturbed crystal of SnS_2 is well described in literature [Schlüter and Schlüter [1973]] and a sample structure of SnS_2 is shown in Figure 3.31. Based on the information gathered through the statistical size study (as presented in Section 3.3.2), this cell could be expanded to a single-layer square sheet of SnS_2 with a side-length of 600 nm, which was then clipped to produce a circular disk.

This idealistic representation in form of a circular disk was then transformed to take the shape of a SnS_2 nano-worm segment. The aim of this was to generate a computer supported simulation of the structure to highlight the presence of faults, dislocations and strain to account for the overall shape of the morphology and to then provide a base for the calculation of lithium ion intercalation routes and

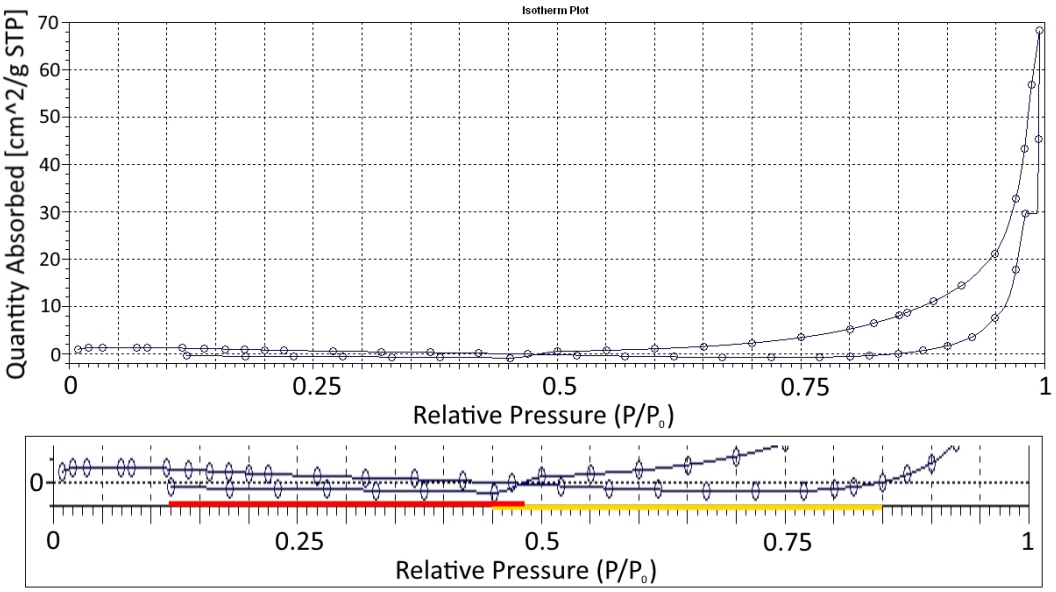

Figure 3.30: *A collected nitrogen-adsorption isotherm for a sample of SnS_2. Noteworthy is that the central-left section of the isotherm, normally used for BET analysis, is dipping below 0, and therefore not exploitable. The enlarged cut-out shows the two sections, red for the release cycle and yellow for the adsorption cycle, where the isotherm drops below 0.*

mechanisms. Molecular dynamics simulations were carried out by a separate group around Elena Bichoutskaia at the University of Nottingham, but were not completed in the time-frame of this project.

For the calculations performed at Warwick, a script using the MATLAB software package was written. Input parameters included the measured diameter of nano-worms and thickness of the disk in the number of molecular layers within the segment. Based on these parameters, the program expanded the SnS_2 unit cell to form a circular disk of the desired diameter and thickness. The atomic positions within this disk were adjusted to give it the shape of a 3D Gaussian distribution around its centre, as depicted in Figure 3.32:

To complete the simulation additional layers were placed on top of the structure, which resulted in a stack of layers (similar to the one in Figure 3.32), each separated by 0.59 nm from its neighbours (distance between tin atoms). By stacking several single layers on top of one another, it is possible to create a single sheet segment of a nano-worm. Nevertheless, there was a drawback to this approach. While it was possible to recreate the global structure of a single hat-like segment, its internal structure was still composed of partially distorted ideal unit cells. To describe the effects of these distortions correctly, further inputs would have been

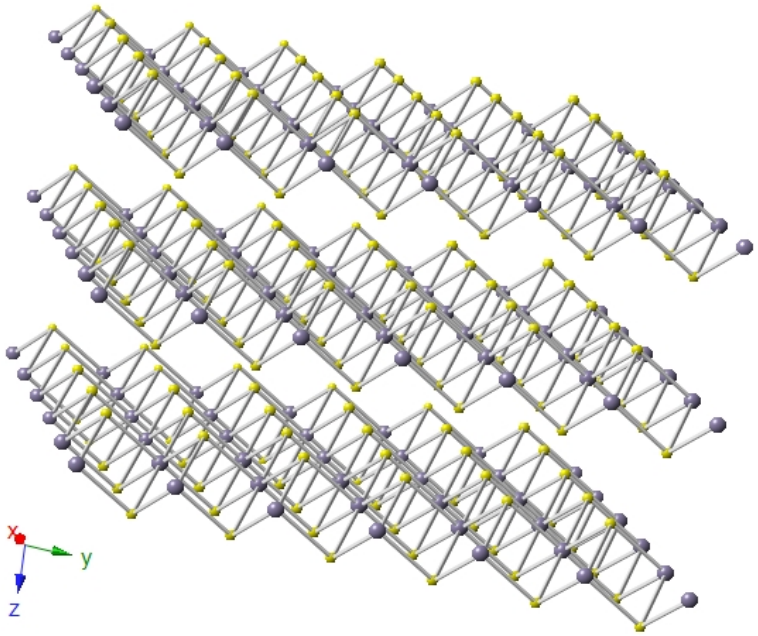

Figure 3.31: *A representation of the atomic positions of tin (purple spheres) and sulfur (yellow spheres) atoms in SnS_2 as produced using [Schlüter and Schlüter [1973]].*

needed to account for the curvature of the structure caused by defects and strain effects. As this information was not available, it was not possible to pursue this approach further.

An additional problem of this approach was that for a full simulation of a hat-like segment with a diameter of 600 nm and containing 15 layers of SnS_2 it was necessary to take a number of atomic lattice positions into consideration in the order of magnitude of 10^7, which made the handling of the respective data files and the necessary calculations using standard software practically impossible. The value of 15 layers was chosen to represent a particularly small sheet thickness. Sheets thicknesses varied from sample to sample, but lay below 60 nm (as can be seen in Figure 3.15 for example), which would correspond to roughly 100 layers based on the layer spacing of 0.59 nm per layer as mentioned above. By choosing this lower value of 15 layers, a lower bound estimate could be established for the contribution of exposed edges to the overall surface area. The thickness does not have an impact on the contribution by the top and bottom surface of the sheet.

In order to circumvent these problems, it was decided to treat each SnS_2 layer as a separate surface, as is described in the next section. Finite element simulations were considered, but not carried out in the time-frame of this project.

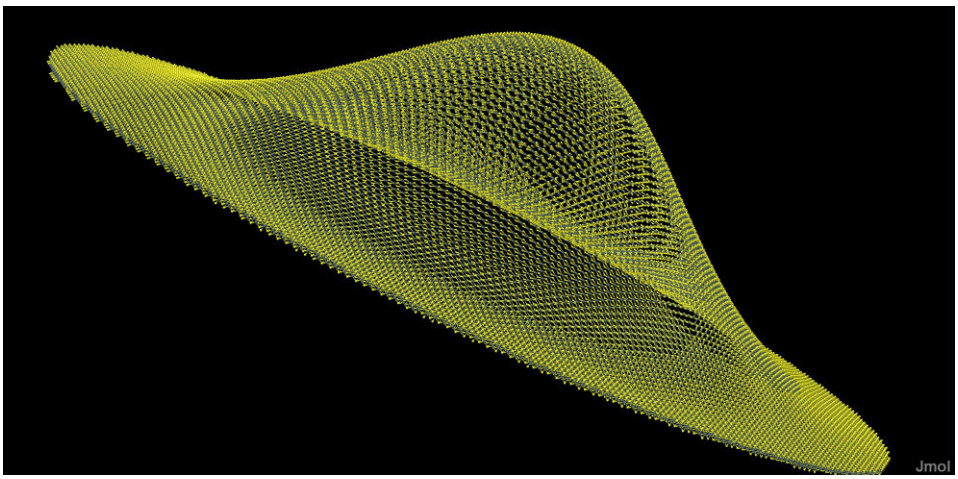

Figure 3.32: *A representation of atomic positions in a circular single layer of SnS_2, modified to take the shape of a 3D Gaussian surface. Atoms coloured in yellow represent sulfur, while tin atoms are shown in purple.*

Topological Approach

The topological mathematical approach to approximate the total surface area of a nano-worm followed a similar route as the atomic position approach described above. It is of particular interest to find a mathematical approximation of the structure, as it not only allows the direct calculation of surface areas and volumes, but also provides a means to mathematically investigate the relation between the topology and the electrochemical properties. It could also be very useful as a means of elucidating the growth mechanism and potential differences that can arise due to variations in the synthesis parameters.

As a first step, a circular plane of radius r_{max} was defined in the X-Y plane of an orthogonal coordinate system and transformed into the shape of a three dimensional Gaussian distribution with height h, as can be seen in Figure 3.33. This made the computational handling of the surface much easier and allowed for full-size models to be handled. Even the simultaneous handling of several surfaces was possible, which allowed for the modelling of not only a single sheet, but a full nano-worm. In this first step, the model was designed to roughly reproduce the overall shape of observed sheets in nano-worms (see for example Figure 3.28), while specific values for the parameters were not yet introduced. In subsequent stages, values obtained through comparison with experimental data were introduced, such as electron tomography and measurements obtained via SEM.

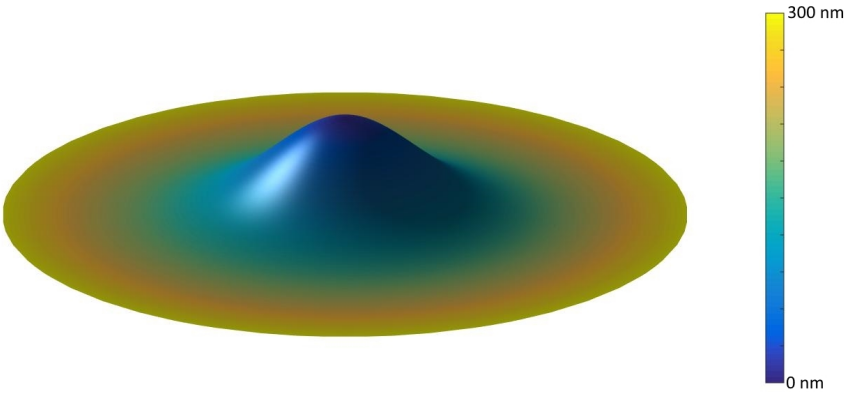

Figure 3.33: *A circular 3D Gaussian distribution with a radius of 300 nm, as used in the topological approach to modelling a nano-worm. The colour scheme represents the distance from the centre in nanometres and was used to facilitate viewing.*

Several further parameters were introduced to enhance the model. As can be seen from the SEM images (see Figure 3.14 and Figure 3.15) taken of the nano-worms, the structures exhibit a wave-like outer perimeter, similar to frills on a skirt. To model this, a displacement Δz of data points in the z-direction was applied. This displacement was a modified sine wave with periodic boundary conditions to allow the wave to close in on itself. Further, the amplitude of the wave was made dependent on the distance of the data point to the centre of the disc r. The values of the amplitude ranged from 0 nm to a user-specified value A_{amp}. The displacement Δz perpendicular to the X-Y plane was thus given by:

$$\Delta z(r(x,y),\Phi(x,y)) = A_{amp} * \frac{r(x,y)}{r_{max}} * sin(\Phi(x,y) * 2 * q) \tag{3.15}$$

Here, q was a parameter set by the user and governed the number of peaks in the amplitude of the wave. Φ was the rotation angle of the point around the z-axis and ensured that the sine wave was always periodic and had no discontinuities along the perimeter of the surface.

A further parameter introduced in the model was an off-set r_{off}. As observed in the nano-worms (for example see Figure 3.28), the displacement Δz occurred along the outer perimeter of the nano-sheets, but it dropped from its maximal value at the perimeter to 0 nm before the centre of the sheet was reached. As a consequence, it became necessary to define the radius at which the model began to include the displacement Δz from its original 3D Gaussian shape. r_{off}/r_{max} was manually chosen for each simulation to allow for slight variations in the off-set

parameter for separate sheets, and usual values were found to lie in the range of 0.3-0.4 by trial and error. If chosen appropriately, the model described objects/shapes as shown in Figure 3.34. It was now possible to rewrite Equation (3.15) as:

$$\Phi = \Phi(x, y) \tag{3.16}$$

$$r = r(x, y) \tag{3.17}$$

$$\Delta z(r, \Phi) = A_{amp} * \frac{r}{r_{max}} * sin(\Phi * 2 * q) * max\{\frac{(r - r_{off}}{r_{max} - r_{off}}; 0\} \tag{3.18}$$

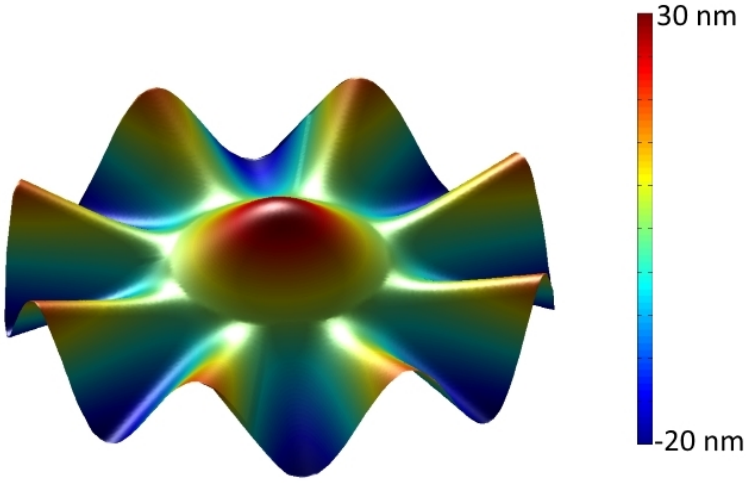

Figure 3.34: *A modelled SnS_2 surface after inclusion of all separate parameters. The colour scale here was used for ease of viewing and represents the displacement from the X-Y plane in nanometres.*

Using the results from images obtained through electron microscopy, it was possible to determine a set of parameters, which fitted the model to observed structures. Particularly good fits were achieved when making comparisons using the data obtained via electron tomography, as can be seen in Figure 3.28.

Based on this, an attempt was made to model a full nano-worm. To do this, several of these modified Gaussian surfaces were stacked on top of each other. A distance of 60 nm between adjacent sheets was chosen based on experimental data, but variations in these distances occurred naturally without having a significant influence on the overall surface area in the model. This value was not obtained via a direct measurement via TEM, as TEM was not able to resolve the inner structure

and distances within the worms as can be seen in Figure 3.15, but instead via a manual process of trial and error based on comparison between simulated worms and the data obtained from electron tomography. As can be seen in Figure 3.25, the central sheets sit very closely together, often touching their neighbours. However, in Figure 3.26, wide gaps appear between the sheets as they continue to grow. Future work could help to further elucidate the exact stacking mechanism, in particular in regard to how each surface touches its neighbours.

In order to calculate the overall surface area of each nano-worm, it was necessary to calculate the surface area of each component sheet. As this would have been computationally very intensive, the approach used the assumption that each sheet can be replaced by a template sheet, with a surface area of the average area of the actual sheets and a representative shape. To approximate reality, a phase shift S_{rot} was introduced, which rotated each sheet slightly. This modified Equation (3.18) to:

$$\Phi = \Phi(x, y) \tag{3.19}$$

$$r = r(x, y) \tag{3.20}$$

$$\Delta z(r, \Phi) = A_{amp} * \frac{r}{r_{max}} * sin(\Phi * 2 * q + S_{rot}) * max\{\frac{(r - r_{off}}{r_{max} - r_{off}}; 0\} \tag{3.21}$$

In the code, S_{rot} was calculated in a random fashion and limited appropriately to ensure that no overlap between neighbouring sheets occurred. The effective rotation resultant from this lay in the range of 50 - 100 milliradian. By additionally randomly shifting the centre of each consecutive sheet by small amounts of a few nanometres in the x-y plane, the model came even closer to matching real structures. The final result is shown in Figure 3.35.

The result of the simulation could now be used to match a full nano-worm as observed with electron tomography to a simulated counterpart. The result of this can be seen in Figure 3.36:

The model as described so far, did not yet account for the individual thickness of each sheet, which still needed to be taken into consideration. This had two main reasons. First, it provided an additional surface area and therefore needed to be included. Second, this surface area was of a different nature as it consisted of open edges of the SnS_2 layers as opposed the closed surfaces on the top and bottom of the segments. This could have an impact on its physical properties (in particular with regards to the intercalation properties of lithium ions into the structure) and thus also needed to be considered.

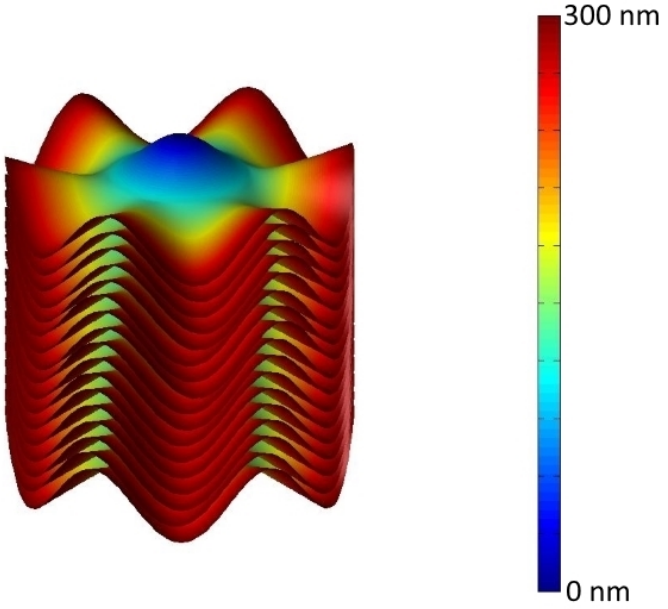

Figure 3.35: *The full nano-worm simulation using all parameters with a small rotational phase shift S_{rot}. The colour scheme corresponds to the distance from the central axis in nanometres.*

To do this, a parameter t was introduced to represent the thickness of each sheet in numbers of SnS_2 layers. While it is technically possible to have a single sheet of SnS_2, this was never observed during our experiments. As discussed in the previous section, sheet thicknesses varied from sample to sample, but never exceeded 60 nm. Similar to the previous approach, it was possible to estimate a lower bound by choosing a low value for t, which was kept at 15 layers as for the atomic position approach. The separation between layers was taken to be the theoretical value as discussed in Schlüter and Schlüter [1973].

After having chosen all parameters accordingly, based on trial and error with the aim to best replicate TEM and SEM results, the model was used to calculate the overall surface area of a nano-worm.

First, the length of the structure's perimeter needed to be determined. Starting point for this was that for any given arc of a function $y = f(x)$, the length of this arc between $x = a$ and $x = b$ can be calculated using the following equation [Bronstein and Semendjajew [1984]]:

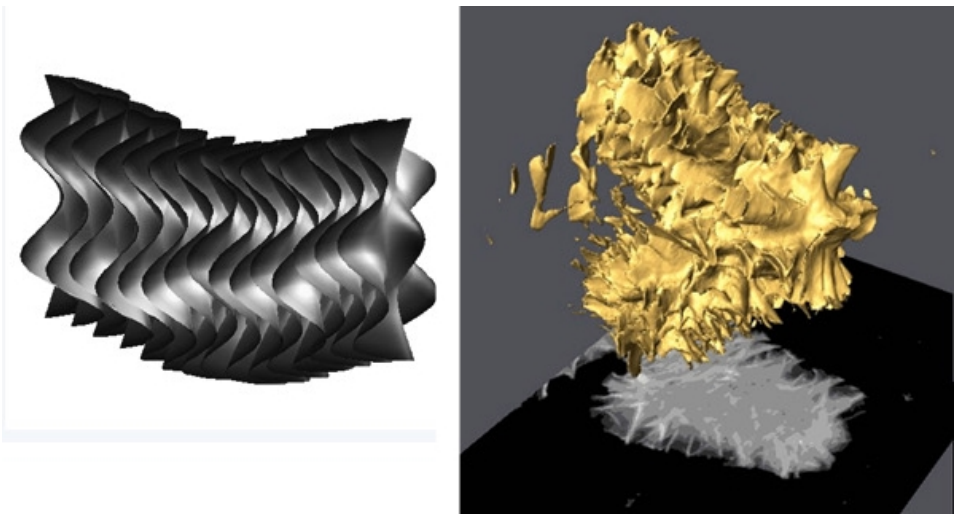

Figure 3.36: *A comparison between a simulated and an observed SnS_2 nano-worm.*

$$length_{arc} = \int_a^b \sqrt{1 + \left(\frac{dy}{dx}\right)^2}\, dx \tag{3.22}$$

By subdividing the interval from a to b into sufficiently small steps, the integral in Equation (3.22) could be replaced by a finite sum, whereby allowing the calculation of an approximation of the length of a complex curve numerically. The precision of the calculation increased with the number of increasingly smaller steps used. In the calculations steps of $\Delta x = 0.01$ nm were used compared to common interval lengths for (a, b) in the range of hundreds of nanometres, which were sufficiently small to expect good values for the perimeter calculation. Multiplying the arc length value by the thickness of the segments was a good measure for the surface area around the sides of the nano-sheet structures.

The calculation of the top and bottom surfaces of each segment was done by covering the surface with small triangles generated by using an algorithm based on Delauney triangulation [Lee and Schachter [1980]], which used all known data points on the surface to construct such triangles between all neighbouring points. By calculating the surface area of all these triangles, this algorithm was used to approximate the overall surface area of the complex 3D surface of the SnS_2 nano-worm morphology.

The results of this simulation, together with a listing of all relevant user-set parameters are shown in Table 3.6.

Parameter	Parameter Value
Nano-worm radius r_{max}	300nm
Height of Gaussian h	90nm
Number of SnS_2 sheet segments	15
Distance between adjacent sheets	60nm
'Curl' parameter q	3
Maximum 'curl' amplitude A_{amp}	20nm
Off-set parameter $\frac{r-r_{off}}{r_{max}-r_{off}}$	0.4 (120 nm)
Segment thickness t	15 layers
Calculated surface area (top and bottom)	9.96 x$10^6 nm^2$
Calculated surface area (thickness)	3.24 x$10^5 nm^2$
Calculated total surface area	1.03 x$10^7 nm^2$

Table 3.6: *A breakdown of simulation parameters and the calculated total surface area.*

The simulated structure is shown in Figure 3.37 for reference:

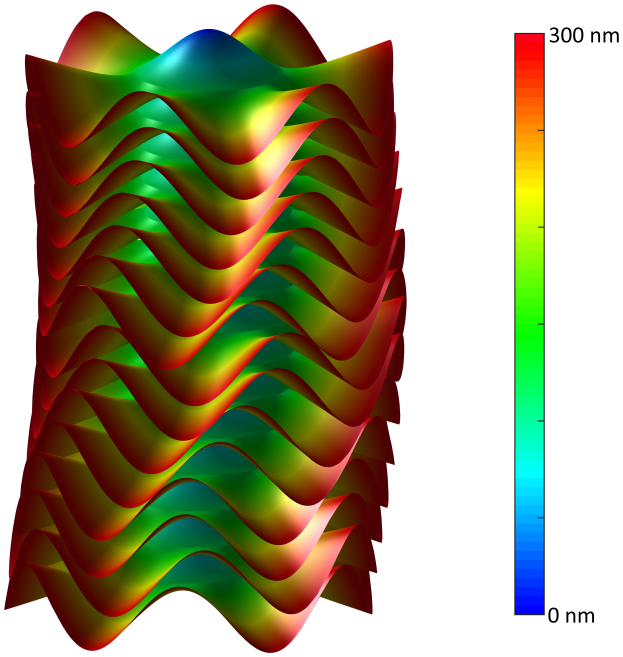

Figure 3.37: *The result of a full simulation of a nano-worm, including slight bending and segment rotation. The colours indicate the distance from the worm axis.*

By having a mathematical model of the nano-worms, it will be possible to differentiate between different types of nano-worms based on their surface areas. Furthermore, it will allow the investigation of variations in growth parameters leading to increased frill development or wider sheet spacings, and will allow a mechanism to directly compare the structure to other SnS_2 nano-structures. In particular by matching variations in synthesis parameters and variations in the adapted models, it will be possible to link specific synthesis conditions to particular growth features. A further advantage of having a mathematical model of the structure is to investigate optimal packing arrangements for nano-worms leading to a potential enhancement of electrode performance in terms of connectivity and storage density. It may also be used to investigate the effect of volume variations during electrochemical cycling.

As the nano-worm structures (which were later processed into electrodes for lithium ion batteries) often arranged themselves chaotically in a sample, it was difficult to derive a consistent value for the overall surface area in a specific sample volume. It was, however, possible to calculate an estimate of a theoretical maximal value based on the following four main assumptions:

1. Each worm was considered to be a representation of an average-sized worm.
2. Each worm was considered to be a hard cylinder for the purposes of packing it in a given sample volume.
3. Each cylinder was long enough to fill the length of the entire sample volume.
4. All cylinders were stacked parallel to each other and obeyed the rules of optimal hexagonal packing. (see Figure 3.38)

The cylinder cross-section could now be used to calculate the overall number of cylinders in a given sample volume. Optimal close packing has got a coverage density of (assuming large volumes to ignore edge effects) [Chang and Wang [2010]]:

$$\eta_{hex} = \frac{\sqrt{3}}{6}\pi = 0.906899... \tag{3.23}$$

For a diameter of 600 nm per worm cylinder, which corresponded to the values measured in the samples of thick nano-worms, this gave a cross-sectional area of approximately $2.83 * 10^5$ nm^2. Therefore, thin and flat cross-sectional layers of sample material contained $N_{worms} = 3.21{*}10^{12}$ different nano-worm cross-sections per square metre.

For the parameters listed in Table 3.6, the number of constituent segments for each nano-worm with a length of 1 m could be calculated using:

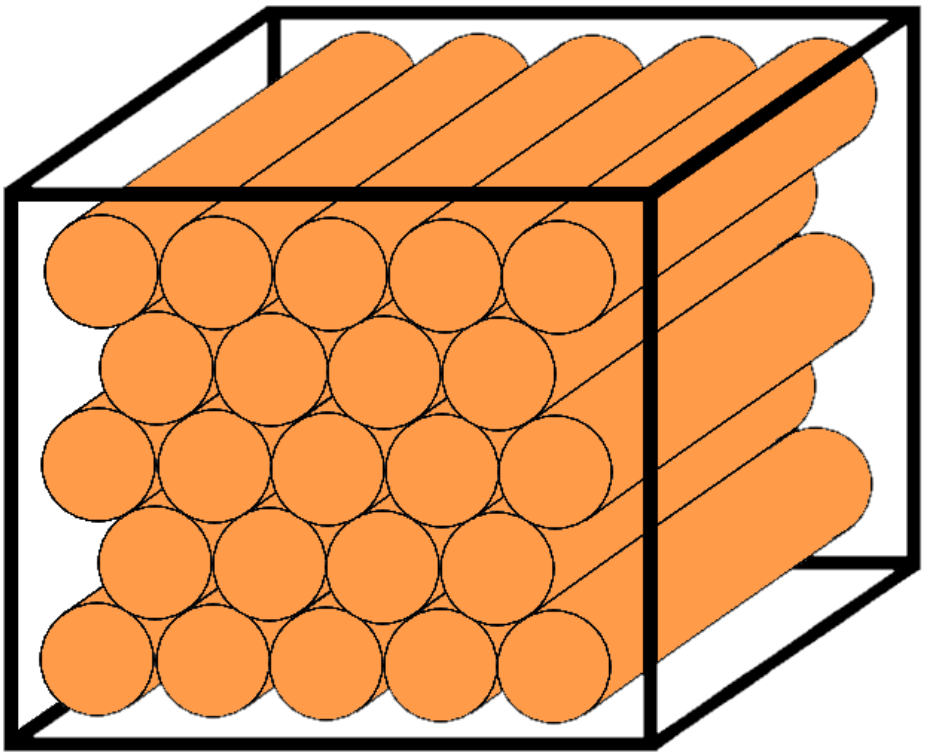

Figure 3.38: *Idealised hexagonal packing of SnS_2 nano-worm cylinders in a closed volume.*

$$N_{segment} = \frac{10^9 - 60}{90} = 1.11 * 10^7 \tag{3.24}$$

Each segment made a contribution of $7.06 * 10^5$ nm^2 to the overall surface area, of which $2.16 * 10^4$ nm^2 was due to the exposed edges around the perimeter of the structure. Thus, the overall area of this 1 m long nano-worm was:

$$S_{Tot} = 7.06 * 10^5 * 1.11 * 10^7 nm^2 = 7.84 * 10^12 nm^2 = 7.84 * 10^{-6} m^2 \tag{3.25}$$

This allowed the calculation of the value of the surface area to volume ratio $(S/V)_{worms}$ for this particular kind of morphology:

$$\begin{aligned} \left(\frac{S}{V}\right)_{worms} &= \frac{S_{Tot} * N_{worms}}{1m^3} \\ &= \frac{2.52 * 10^7 m^2}{m^3} \end{aligned} \tag{3.26}$$

It should be kept in mind that this value was based on an idealised arrangement of idealised SnS_2 nano-worms and will therefore not be reflected fully in reality. As the nano-worms usually arrange themselves chaotically and exhibit a variable diameter, the true value for each sample may be slightly different, but should still be of the same order of magnitude.

To put this value into context, it was compared to the surface area to volume ratio of other materials. Commercially available Super P Carbon Black (which was used for electrode manufacture) had a surface area of 62 m^2/g and a density of 160 kg/m^3. Therefore, the surface area to volume ratio was:

$$\begin{aligned}\left(\frac{S}{V}\right)_{SuperP} &= 62000\frac{m^2}{kg} * 160\frac{kg}{m^3} \\ &= \frac{9.92 * 10^6 m^2}{m^3}\end{aligned} \tag{3.27}$$

Thus, a sample of SnS_2 nano-worms with an average diameter of 600 nm had a surface area to volume ratio roughly in the same order of magnitude as that of commercially available Super P Carbon Black.

This concluded the work on the physical characterisation of the synthesised SnS_2 nano-particles. The next part of the work was the electrochemical testing of these nano-particles.

Chapter 4

Electrochemical Properties of SnS_2

The basic electrochemistry of a cell containing tin disulfide and lithium was well-known thanks to the wealth of research conducted on the system.

The cell reaction at the lithium electrode was:

$$\mathrm{Li} \leftrightarrow \mathrm{Li}^+ + \mathrm{e}^- \tag{4.1}$$

Thus, for each mole of lithium atoms in the electrode, it was possible to release one mole of electrons. This gave a theoretical charge capacity of 3860 mAh/g for lithium [Fauteux and Koksbang [1993]].

The reaction occurring at the opposite electrode was slightly more complex as it was split into two separate steps, one reversible and one irreversible. Upon the first charge, the transported lithium reacted with both the tin and the sulfur:

$$SnS_2 + 4Li^+ + 4e^- \rightarrow Sn + 2Li_2S \tag{4.2}$$

$$Sn + xLi^+ + xe^- \leftrightarrow Li_xSn \text{ where } (0 < x < 4.4) \tag{4.3}$$

The first reaction was irreversible. The lithium ions used up by it contributed to the construction of a Li_2S structural matrix that held the tin atoms in place. The second reaction was reversible and was the reaction that enabled the cell to store and release energy.

The theoretical maximum charge capacity of the cell during the first charge cycle could be calculated by considering an electron transfer of 8.4 electrons per molecule of SnS_2:

$$C_{0,theo} = \frac{8.4 * 6.022 * 10^{23} * 1.6 * 10^{-19}}{182.81} \frac{As}{g} \approx 1230 \frac{mAh}{g} \tag{4.4}$$

Likewise, the theoretical maximal charge capacity of every ith consecutive cycle could be calculated by assuming a maximal electron transfer of 4.4 electrons per molecule of SnS_2:

$$C_{i,theo} = \frac{4.4 * 6.022 * 10^{23} * 1.6 * 10^{-19}}{182.81} \frac{As}{g} \approx 644 \frac{mAh}{g} \tag{4.5}$$

As mentioned in Chapter 1, modern SnS_2 electrodes could come very close to reaching this reversible value.

4.1 Initial Testing

The initial tests of the synthesised SnS_2 nano-powders were performed using a Swagelok-based cell system, as is briefly described below.

4.1.1 Electrode Manufacture

After having synthesised the active SnS_2 electrode material, it was washed repeatedly using ethanol to remove all reaction by-products. It was then subjected to a brief SEM analysis to determine the prevalent SnS_2 morphologies and to check for any significant contamination. If no contamination could be observed via EDS, the sample was deemed to be of a satisfying purity, as, for example, the sample shown in Figure 4.1, and it was dried overnight under vacuum at 60 °C and then introduced into an argon-filled glove-box, where it underwent a final drying process to ensure that no trapped water molecules remained in the sample.

A drawback of using powders in electrodes as opposed to bulk material was that powders can suffer from connectivity issues between neighbouring grains. It was therefore a standard procedure to mix a powdered active material with a conduction enhancer to ensure good conduction throughout the electrode. Ideally, the conduction enhancer should have a minimal influence on the chemistry within the cell. The most commonly utilised material in electrode manufacture for lithium ion batteries was carbon black. Carbon black are small, amorphous particles of conductive carbon that settle in between the bigger nano-particles of SnS_2 and thereby provide an electric connection between them. Super P Carbon Black as supplied by Alfa Aesar was used during this project.

Structural integrity was another big issue for powder-based electrodes as nano-particles were free to move and only held in place by their friction against one

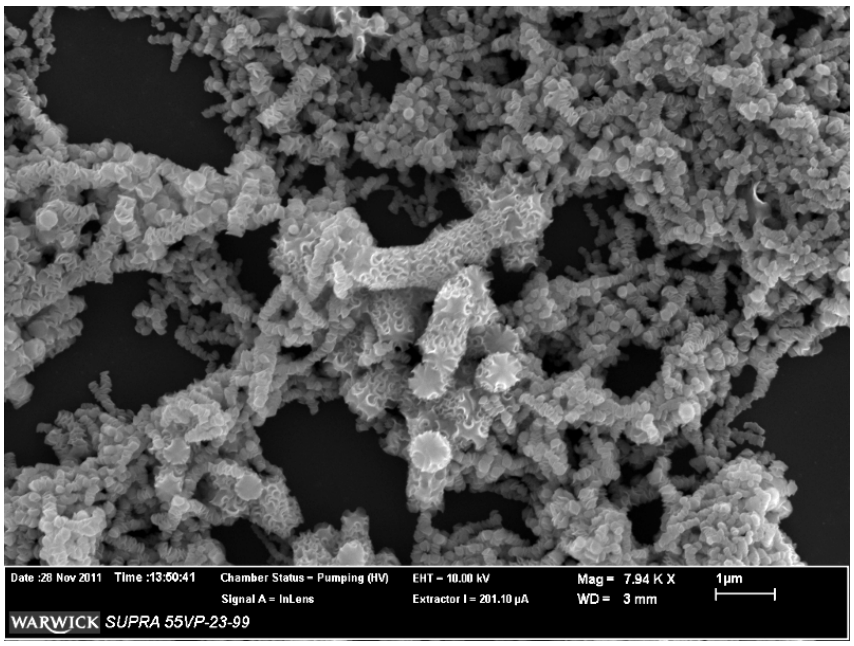

Figure 4.1: *A SEM image of a nano-worm sample as used in electrode manufacture. The pre-dominant morphology were the nano-worms, including both thin- and thick-type worms.*

another. In a dried electrode, this might have provided enough structural stability to maintain a cohesive structure, but the use of liquid electrolytes could lower the friction between the particles and therefore cause the electrode to disintegrate quickly. This problem was further exacerbated by volume changes of the nano-particles within the active material during cell cycling, causing movement within the electrode. The easiest solution to this problem was to use a glue or binder. However, the glue had to have several important properties. As the conduction enhancer mentioned above, it had to be non-reactive and was not allowed to interfere with the internal cell chemistry. Furthermore, it had to be sufficiently flexible to allow the SnS_2 nano-particles to grow and shrink without losing hold of them, and it had to be ensured that the electrode remained sufficiently porous to allow easy lithium diffusion into the bulk. Finally, the glue had to be resistant to the strong organic solvents that constituted the carrier liquid of the battery electrolyte. The choice of material as binder was polyvinylidene fluoride (PVDF), which was a highly non-reactive thermoplastic polymer and had seen widespread use in lithium ion cells. The PVDF used in this project was supplied by Sigma Aldrich (average molecular weight of 534,000 by GPC, powder).

All materials were placed inside an argon-filled glove-box to ensure the ex-

clusion of water and were mixed using a small mortar and pestle to break up clumps of powder. In the process, special care had to be taken to ensure that the active material morphologies were not ground up or destroyed. After mixing the yellow (SnS_2), black (carbon black) and white (PVDF) powders, the result was a dark grey, sticky powder with a homogeneous colour distribution. The ratios between the active material, binder and conduction enhancer varied widely in the literature, but the active material normally accounted for more than 50% of the final product, while binder and conduction enhancer made up the difference in equal amounts. A ratio between the three components that is widely used is 70:15:15 by weight (SnS_2 : carbon black : PVDF), which was also adopted as the standard in this project. A breakdown of this is illustrated in Table 4.1.

Material Name	Chosen Ratio [% w/w]	Weight [mg]
Tin Disulfide (SnS_2)	70%	33 mg
Carbon Black (C)	15%	7.07 mg
Polyvinylidene Fluoride $(C_2H_2F_2)_{poly}$	15%	7.07 mg

Table 4.1: *Breakdown of material weights for an average synthesis yield of 33 mg of SnS_2. The total dry weight of the produced electrode was approximately 47 mg.*

The produced electrode powder needed to be processed into a slurry that could be cast onto a current collector and thinly spread out without the occurrence of gaps or holes. In order to create the slurry, the electrode powder was mixed with an organic solvent, which could be evaporated off after casting. The solvent used for this purpose was N-methyl pyrrolidinone (NMP), which is widely used in electrode fabrication. Further care needed to be taken to ensure that the right amount of solvent was used. When too little of the solvent was used, the electrode was difficult to cast, resulting in severe cracking during the drying phase. Using too much of the solvent caused problems for the creation of electrodes with homogeneous thickness. By trial and error it was possible to establish that 5 to 7 drops from a standard 10 ml laboratory pipette (0.25-0.35 ml) was a sufficiently good amount to use for 50mg of slurry powder. The NMP was supplied by Sigma Aldrich (1-Methyl-2-pyrrolidinone, biotech. grade, >99.5%).

The slurry was then spread over a copper current collector (copper was used as current collector for anodes, while aluminium was used as current collector in casting cathodes). A thin copper foil (99% copper) of 25 μm thickness was used. When the slurry was spread out, special care had to be taken to ensure an even

surface was available to work with, by either a very steady hand or the use of a doctor blade. The copper foil was obtained from Alfa Aesar (Copper foil, 0.025 mm (0.001 in) thick, Puratronic, 99.999% (metal basis)).

Subsequently, the foil and its electrode coating were inserted into a vacuum furnace and dried at 40 °C under vacuum (800 mbar) for at least 4 hours. At higher temperatures or stronger vacuums the drying process proceeded too rapidly, which resulted in cracks in the electrode surface.

Following this last step, the electrode was ready to be used in a test cell once it had been cut to size. The trimmings were used to examine the electrode structure via SEM. An example image of this kind is shown in Figure 4.2. Here, a side-on view of the electrode interface is visible. As can be seen, the addition of both the carbon black and the PVDF have caused the creation of a connected and porous electrode surface.

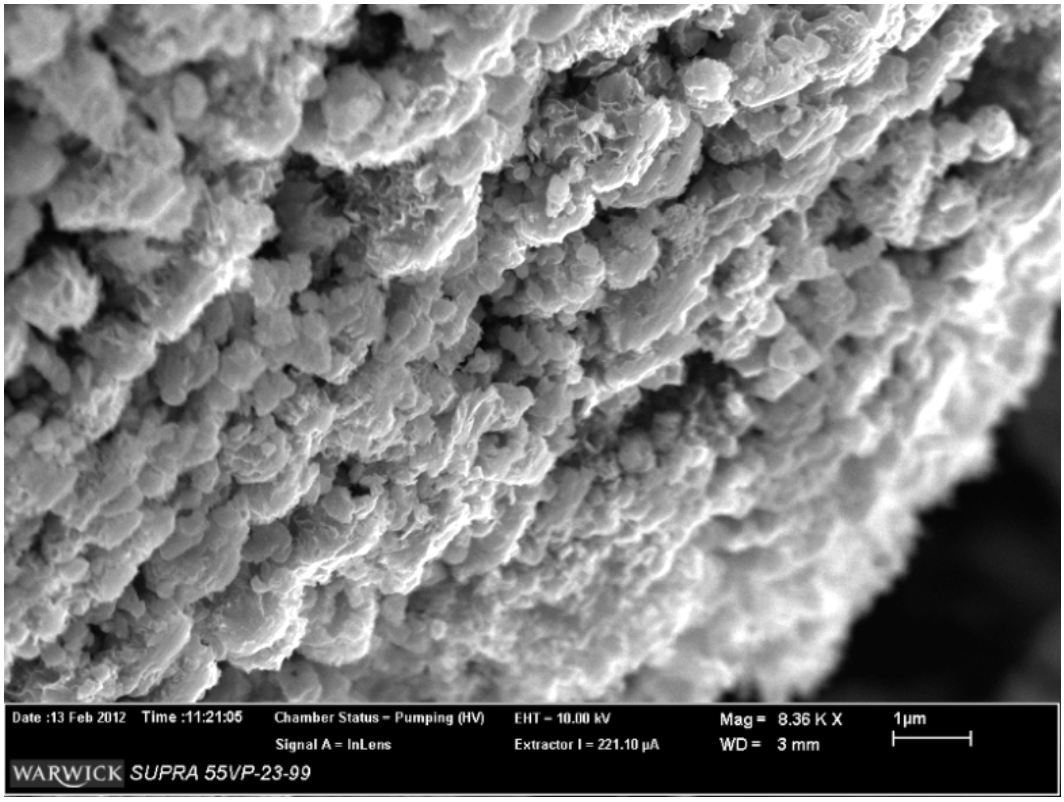

Figure 4.2: *A tilted, side-on view of an electrode surface. Noteworthy was that the bigger SnS_2 nano-worms seemed to have survived the manufacturing process, while the thin-type worms had largely broken up into shorter segments. This, however, did not significantly change the overall surface area of the active material, and should not impact the battery performance.*

4.1.2 Electrolyte Mixing

Based on a comprehensive literature review, as discussed in the introduction section of this project, the choice was made to use lithium hexafluorophosphate $LiPF_6$ as battery cell electrolyte. As carrier solvent for the electrolyte, a combination of ethylene carbonate (EC) and diethyl carbonate (DEC) (the ratio of EC:DEC was set at 1:1 w/w) was chosen. Even though ethylene carbonate was solid at room temperature, the combination with diethyl carbonate created a clear, non-viscous liquid. The overall electrode concentration was set at 1M $LiPF_6$ and the powdered $LiPF_6$ was added to the solvent carrier. Dissolution was slow, but by regular agitation over several hours it was possible to remove any remaining sediments. All three components were obtained commercially from Sigma Aldrich (Lithium hexafluorophosphate, battery grade, >99.99% trace metals basis; Ethylene carbonate, anhydrous, 99%; Diethyl carbonate, anhydrous, >99%).

As electrolytes based on lithium hexafluorophosphate degrade with prolonged storage time [Takami et al. [1992]], it was necessary to mix fresh batches of electrolytes every four weeks. This time interval varies with the storage conditions of the electrolyte. If exposed to heat or direct sunlight, degradation could occur rapidly. Under the right storage conditions, however, degradation is a slow process and accompanied by a change of colour in the electrolyte solution from colourless to various degrees of yellow (from very light yellow to almost orange). If left unstirred, large crystals could be seen to grow, making the continued use of the electrolyte inadvisable (pierced separators and unwanted cell reactions could result from this). By ensuring the production of a fresh batch every four weeks, it was possible to use the electrolyte before colour changes or crystal growth set in.

4.1.3 The Swagelok Test Cell

The first prototype cell for the testing of the electrode material was based on an old design, which relied on a combination of pipe fittings [Muñoz-Rojas et al. [2007]]. In reference to the big supplier of these, this design was often referred to as the 'Swagelok cell'. The cell body consisted of a single piece of pipe with two open ends, which was coated internally by a thin, non-reactive plastic film to isolate the cell electrically from its casing and to prevent any possible reactions between the cell components and the case. All internal components of the cell were mounted in the centre of the pipe and held in place by two big metal plungers, which ensured a good connection between the electrodes. The plungers were kept in place by a set of seals and O-rings to ensure that the cell was completely sealed off from the

ambient environment, and then fixed by a set of heavy duty nuts. Their purpose was to ensure that in case of an internal pressure build-up, the plungers would not explosively leave the cell. Both plungers could be connected to experimental equipment, such as potentiostats or galvanostats. An example of a Swagelok cell is shown in Figure 4.3, which also shows a schematic cross-section of the cell (CE stands for 'Counter Electrode'):

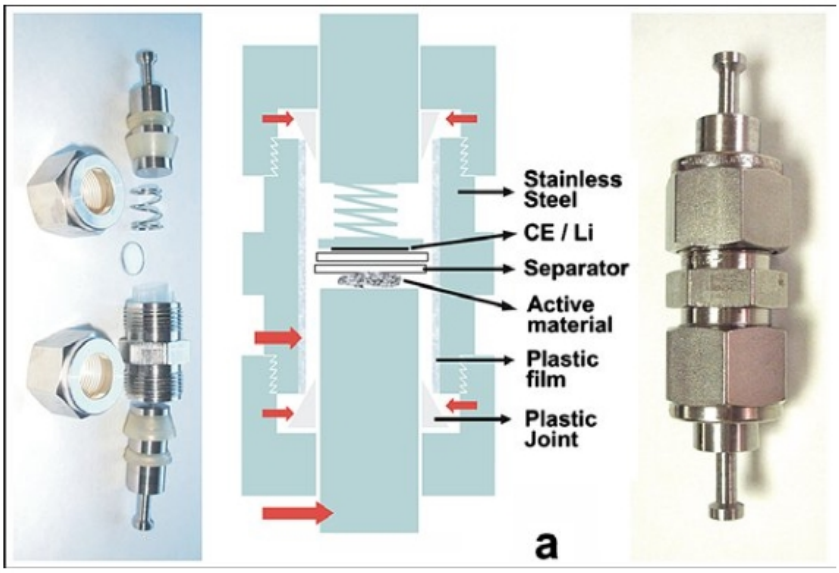

Figure 4.3: *A schematic view of a test cell based on the 'Swagelok' design. Care had to be taken, especially with these metal based cells, that no direct electric connection between the two plungers was possible. CE/Li stands for 'Counter Electrode/Lithium Electrode (as the common counter electrodes in this set-up are lithium electrodes). Adapted from [Muñoz-Rojas et al. [2007]].*

In order to avoid the danger of an internal short-circuit altogether, a Swagelok design based on Teflon instead of stainless steel was chosen, thus making all the parts of the cell casing (apart from the plungers) electrically insulating. The cells (a two-electrode set-up for galvanostatic cycling and a three-electrode set-up for cyclic voltammetry) are shown in Figure 4.4:

The use of Teflon instead of stainless steel made the cells considerably safer to handle, while still providing a sealed, and electrically insulated, environment.

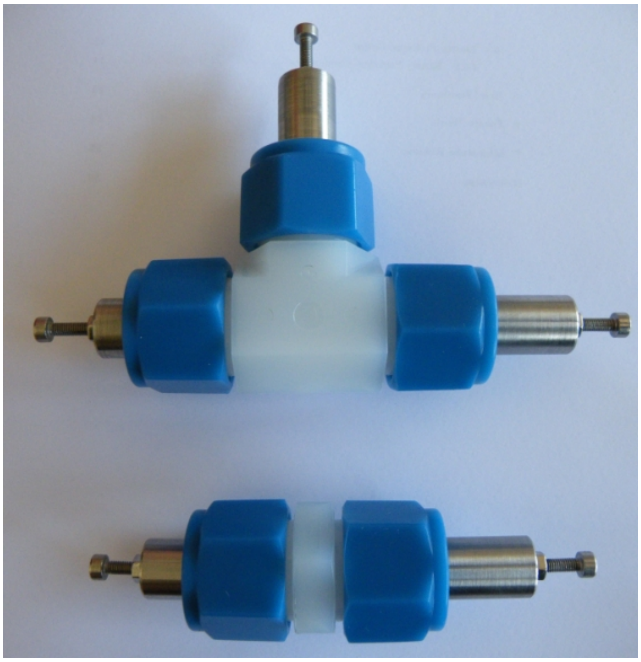

Figure 4.4: *The two Swagelok-type test cells based on Teflon designed for this project.*

4.1.4 Cell Assembly

A cell was assembled in three consequential steps, all of which required execution in a glove-box under the exclusion of water. The first step was to mount the active electrode. For this, the electrode foil, consisting of the copper foil substrate and its electrode slurry coating, was cut to size. The inner diameter of the Teflon Swagelok cells were 9 mm in size, so circular disks of an equal diameter were cut from the foil. Care had to be taken as the electrode slurry proved to be very brittle. The electrode disk was then mounted on one of the metal plungers and covered with an appropriately cut battery separator sheet. For the investigation a Celgard 2400 separator film was used, which was composed of porous polypropylene. Should the cell reach a temperature that could cause it to enter thermal-runaway, the separator would melt, causing the pores to seal shut, whereby insulating both electrodes from each other and shutting the cell down.

The second step was the injection of the electrolyte solution into the test cell. Lithium ion cell electrodes did not need to be submerged in the electrolyte, but required only enough electrolyte to wet the electrodes and separator throughout. Therefore, only a few drops of the electrolyte solution were used during each experiment.

The final step consisted of mounting the counter electrode. Several options

for a cathode counter electrode existed, but a lithium foil of high purity was chosen to keep the cells as simple as possible. Unfortunately, this meant that direct handling of the dangerous metal was not avoidable, which made additional safety measures necessary. The lithium foil was obtained from Alfa Aesar (Lithium foil, 0.75 mm (0.03 in) thick x 19 mm (0.75 in) wide, 99.9% (metal basis)). Once all three components were stacked in the test cell (similar to what can be seen in Figure 4.3), the second plunger was inserted to seal the cell. It was now possible to remove the completed cell from the glove-box and subject it to testing.

4.1.5 First Tests Using the Swagelok Cells

The first tests conducted on the cells were simple charge-discharge cycling runs. As discussed in the literature, limits for the cell potential were chosen based on information from comparable materials (such as the case of Nano-Flowers in [Liu et al. [2010a]]).

The tests themselves were run using a constant current power source. The current was set at a density I_ρ of 200 mA per gram of active electrode material (M_{active}), and so the actually applied current was [Liu et al. [2010a]]:

$$I_{actual} = I_\rho * M_{active} \tag{4.6}$$

As the power source was not equipped with a timer, it was necessary to permanently keep track of time and cell voltage manually, which added a certain element of uncertainty to the experiments. However, the experiments still served as valuable proofs-of-concept. Calibration of the set-up was undertaken using a commercially available LIB of the AA format.

The active electrode weighed 56 mg after subtracting the weight of the copper foil, giving a total weight of 39.2 mg for the present active material in the cell, M_{active}. Using Equation (4.6), the applied current, I_{actual}, was 7.84 mA. The undisturbed potential of the cell was measured to be 3.39 V. The cell was then discharged until its potential reached 0.85 V. The results are presented in Figure 4.5:

An analysis showed that the cell provided a capacity of 129.92 mAh/g in the cell potential range of 3.39 V to 0.85 V vs Li/Li^+, roughly 20% of its theoretical maximum value. While this value was by no means comparable to higher values obtained by other research groups for their morphologies of SnS_2 (see Chapter 1), it still proved that the cell had the potential to store lithium ions.

Throughout the next several experiments, a series of severe shortcomings were discovered with this Swagelok cell design. During cell assembly, the electrically

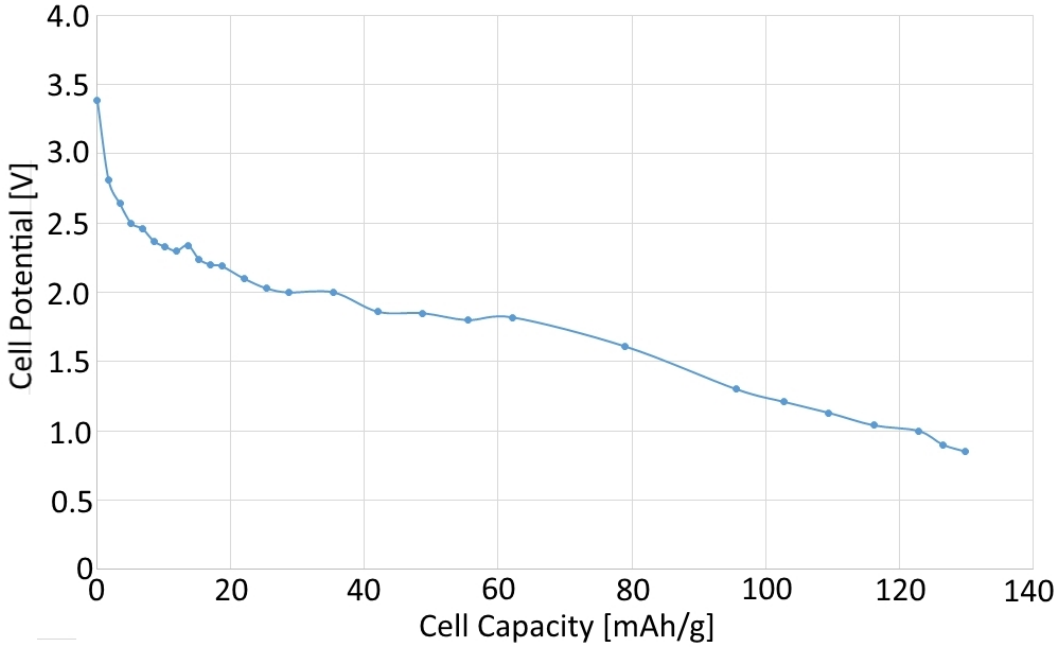

Figure 4.5: *A discharge curve of one of the first test cells built. An accurate collection was difficult, but the cell provided sufficient proof-of-principle to continue this line of research.*

insulating Teflon gained an electrostatic charge that made the electrode mounting process very difficult to complete, as the electrodes were deflected violently. Additionally, it developed a charge leak over time, which caused a significant trickle current and led to self-discharge. Because of these shortcomings, it was decided to move to a more reliable cell system.

4.1.6 Coin Cells

The coin cell system was a big improvement in terms of the handling of the test cells. Cells were manufactured using the same procedure as before, with slightly bigger electrode diameters made possible through larger cell casings. Each cell therefore now primarily consisted of an anode, a cathode, a separator and an electrolyte, as well as a stainless steel top and bottom half of a CR2016 coin cell (see Figure 4.6). The code '2016' corresponded to the actual dimensions of the cell, the first two digits representing the diameter in mm and the last two representing the height of the cell in mm/10. Each cell could be equipped with additional stainless steel spacers in case the height of the electrode stack was not sufficient to fill the case.

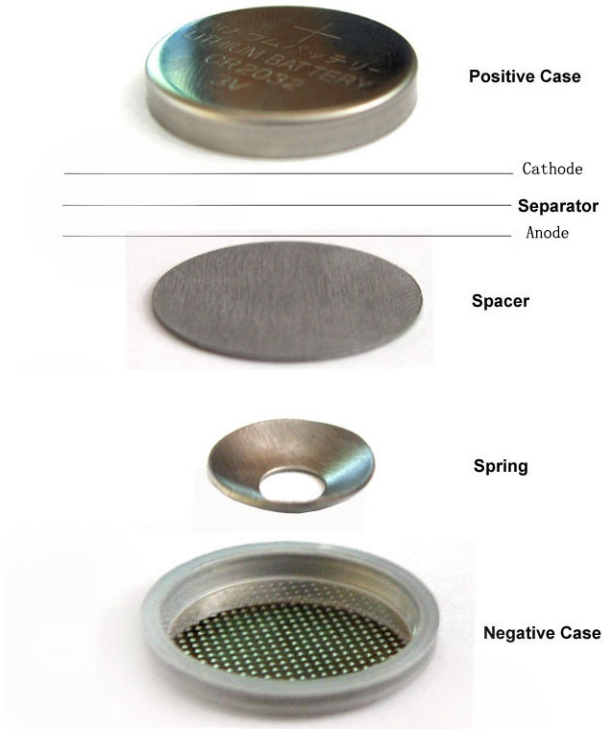

Figure 4.6: *A schematic breakdown of all possible components of a standard CR2032 coin cell, which replaced the Swagelok cell design first used. Due to the thinness of the electrodes, it was later found that CR2016 cells were better suited, which are identical to their CR2032 counterparts, but are of half height. From [MTI Corporation [2013]]*

After cell assembly in a glove-box, the casing was closed and crimped shut using a hydraulic crimping press. The cell was then ready to be removed and tested electrochemically.

4.2 Cyclic Voltammetry (CV)

Cyclic voltammetry was performed on standard CR2016 coin cells consisting of an electrode containing 3 to 12 mg of active material. The counter electrode was made from lithium metal foil and the electrolyte was a 1M $LiPF_6$ solution in an ethylene carbonate - diethyl carbonate mixture (1:1 w/w). Both working and counter electrodes were circular with a diameter of 9 mm, covered by a large sheet of Celgard 2400 separator. The limits of the cell potential during the tests were set at 0.1 V and 2.5 V vs Li/Li^+, based on similar work done on SnS_2 by Liu et al. [2010a].

The voltage was ramped between both limits at a steady rate of 1000 mV/s, as can be seen in Figure 4.7.

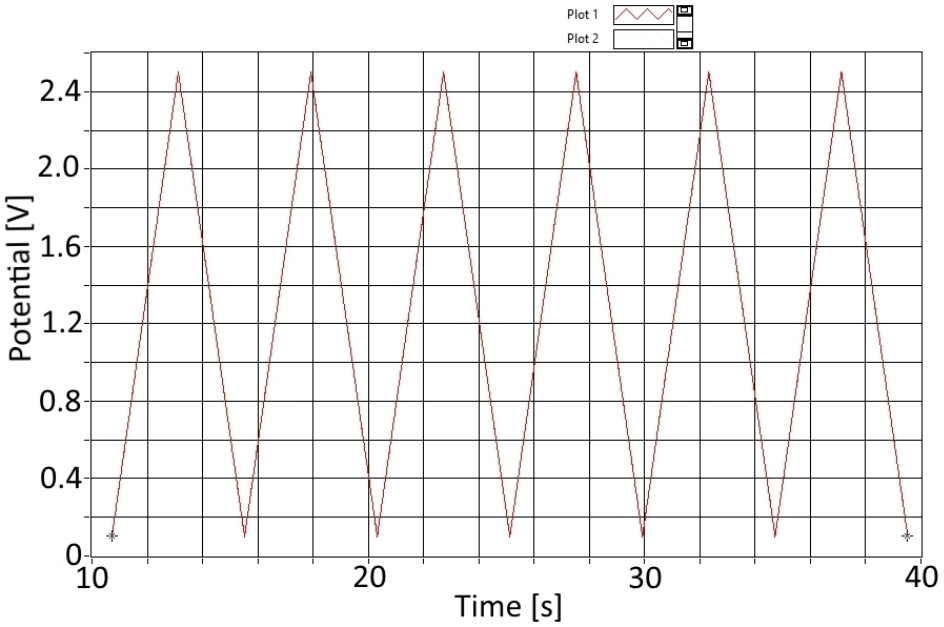

Figure 4.7: *The cell potential as it was ramped over 6 full cycles.*

The response current was measured as the potential was ramped between the two voltage limits and is shown in Figure 4.8 as a function of time:

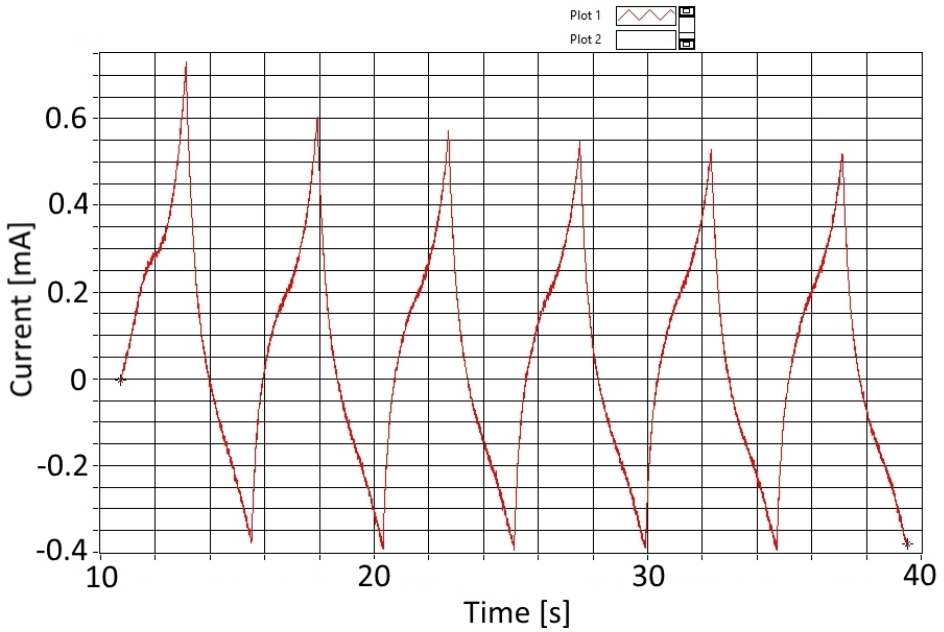

Figure 4.8: *The measured response current as a function of time over the same 6 cycles as shown in Figure 4.7.*

For the test, the total number of cycles was set at 50. A collected voltammogram is shown in Figure 4.9. The cells showed good stability over the entirety of the measurement cycles. The response current was slightly lost among the higher cell potentials, but in the lower range between 0.1 V to 1.4 V, the cells quickly settled on a stable response current. To compare cycle loops in more detail, Figure 4.10 shows only the first and 50th cycle.

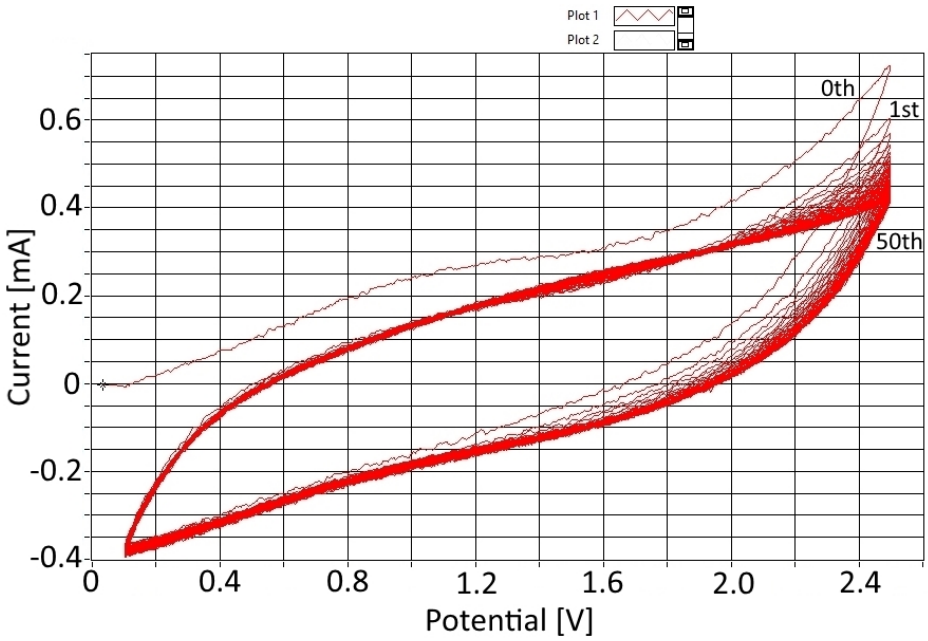

Figure 4.9: *The cells were cycled 50 times and the measured CV loops showed good stability. Especially at lower potentials the cells gave a very stable current response. The cycle numbers are indicated in the figure. The 0th cycle is always different from the others, which is due to cell activation symptoms.*

The first half-cycle, denoted within this project as the 0th cycle, is commonly different from successive cycles. This is due to the cell coming into operation for the first time, called cell activation. During cell activation a number of factors come into play that affect the measurements taken during this cycle, most notably irreversible reactions that consume charge carriers, such as the creation of a Li_2S buffer matrix in the case of SnS_2, or the creation of the Solid-Electrolyte Interphase, which is due to the chemical reduction of the electrolyte carrier solvent.

It should be noted that none of the cycles shown in Figure 4.9 showed any discernible peaks corresponding to specific reactions within the cells. This may have been due to the high speed at which the potential was ramped. This may not have

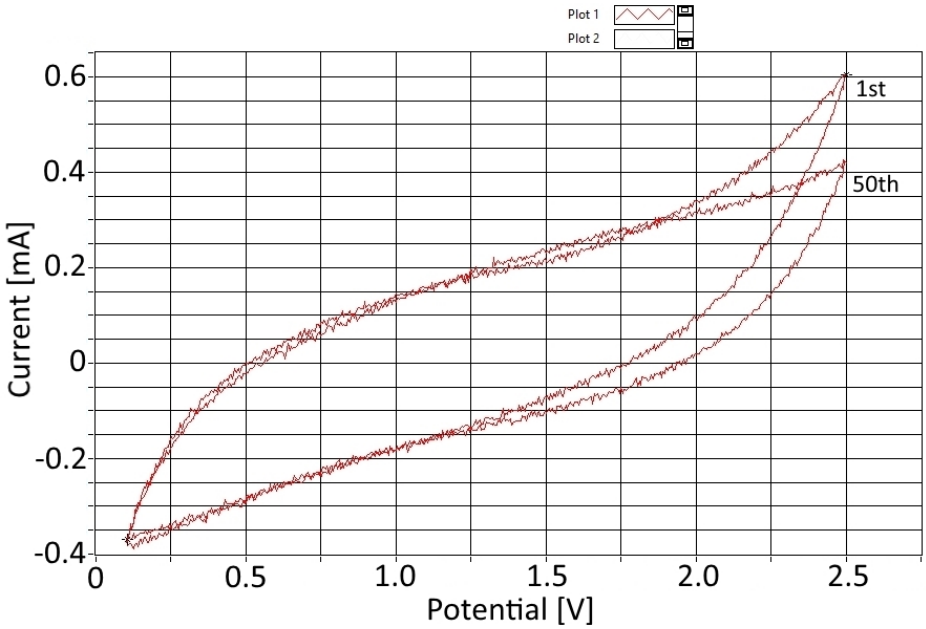

Figure 4.10: *A comparison between the first and last cycle of a test run. While current responses stayed very stable at lower potentials, higher potentials saw a small drop in the induced current. The cycle numbers are indicated in the figure.*

given the cell any time to respond. To investigate this issue, it was decided to collect additional cyclic voltammograms using a voltage ramp of 0.5 mV/s. Cycles obtained this way are shown in Figure 4.11:

By switching to a lower potential ramp speed, it was possible to resolve several peaks that had previously been suppressed. The cathodic peak at around 1.1 V had been reported to correspond to the creation of metallic tin and lithium sulfide [Liu et al. [2010a]]. The neighbouring peaks, however, had not yet been reported and could have possibly corresponded to different stochiometries of Li_2S. There were several additional, temporary smaller peaks in the first anodic scan, such as the ones at around 1.15 V, 1.4 V and 1.9 V, which also hadn't been reported on and have not yet been attributed to a type of cell reaction. Each one of these peaks corresponds to different intra-cell reactions, but similar to the results obtained by Liu et al. [2010a], it was not possible to associate a particular peak to a particular cell reaction. Possible reactions include lithium intercalation in the carbon conduction enhancer or into materials making up the solid electrolyte interphase (SEI). Peaks stemming from the reduction of the electrolyte to form the SEI can be disregarded, as these should only be present in the first and possibly second cycle. After the first scan, two more stable anodic peaks appeared at around 1.3 V and 1.65 V.

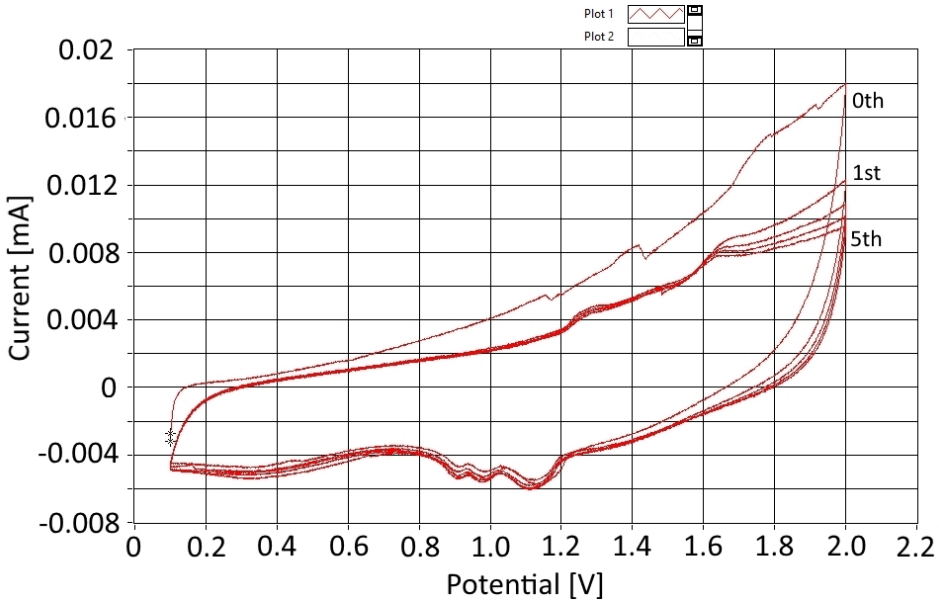

Figure 4.11: *By subjecting cells (identical in construction to the ones used for the experiment shown in Figure 4.9) to a lower voltage gradient, several peaks appeared in both the cathodic and anodic scans. The cycle numbers are indicated in the figure. Again, the 0th cycle is different due to cell activation.*

Most notably, the peaks usually associated [Liu et al. [2010a]] with red-ox reactions leading to lithium intercalation at 0.1 V (cathodic) and 0.6 V (anodic) were not visible.

4.3 Galvanostatic Cycling (GC)

Cells were prepared the same way as for CV described above. Before inserting the active electrodes into the test cells, they were weighed to determine the mass of active SnS_2 material contained within the electrodes. These values were used to determine the level of the charge/discharge current. 300 mAh/g was used as I_ρ in Equation (4.6) to determine the applied current.

Figure 4.12 shows the result of a 5-cycle charge-discharge experiment performed on a test coin cell. The amount of active material was weighed and determined to be 1.96 mg, so a current of 0.6 mA was used (see Equation (4.6)). By integrating the current over the time of a charge or discharge step, and thus via calculating the area of the trapezoids beneath each data point, the total capacity was calculated. In the case presented in Figure 4.12, the first cycle showed a capacity of 90.6 mAh/g, while subsequent cycles showed values in the range of 30 to 35 mAh/g.

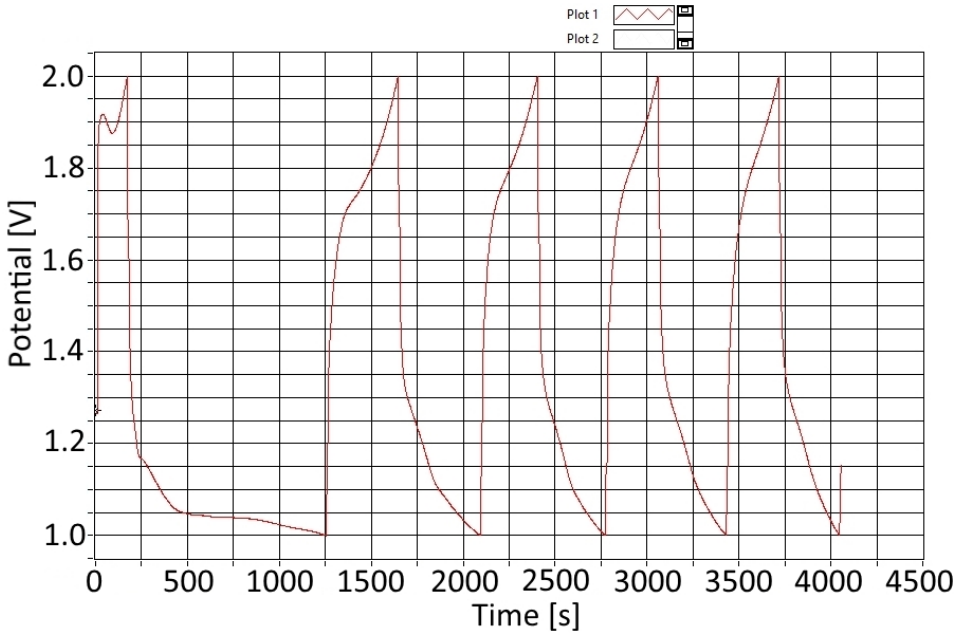

Figure 4.12: *Results of a galvanostatic cycling experiment performed on a test coin cell. The cut-off voltages were chosen to be 1 V and 2 V. Noteworthy was that the first cycle (after setting the cell to 2 V) was considerably longer than the ones following, which accounted for the additional charge transfer (possibly due to irreversible reactions within the cell/cell activation).*

Further experiments were conducted, in particular in regard to operating within a larger potential range. A second set of curves is shown in Figure 4.13. The mass of the active material was measured to be 2.01 mg, allowing for a current level of 0.6 mA to be used, as in the previous experiment shown in Figure 4.12.

By integrating the current over time as above, it was possible to show that the cell had a capacity of 82.6 mAh/g during the first cycle, which is close to the previously calculated value. Subsequent cycles had a significantly reduced capacity in the range of 15 to 20 mAh/g. Unfortunately, a fairly large degree in variation was also observed in subsequent test series and while it was possible to exclude causes such as the cell manufacturing method, it was not possible despite considerable efforts taken to determine the exact cause for these variations.

An attempt was made to open the cycled cells using a disassembly die. However, due to the presence of the liquid electrolyte, the electrodes were very soft and proved to be very difficult to remove from the case and the separator. When drying the cell assemblies to remove the organic carrier solvent, a layer of the lithium salt lithium hexafluorophosphate remained on the electrode surface and could not be

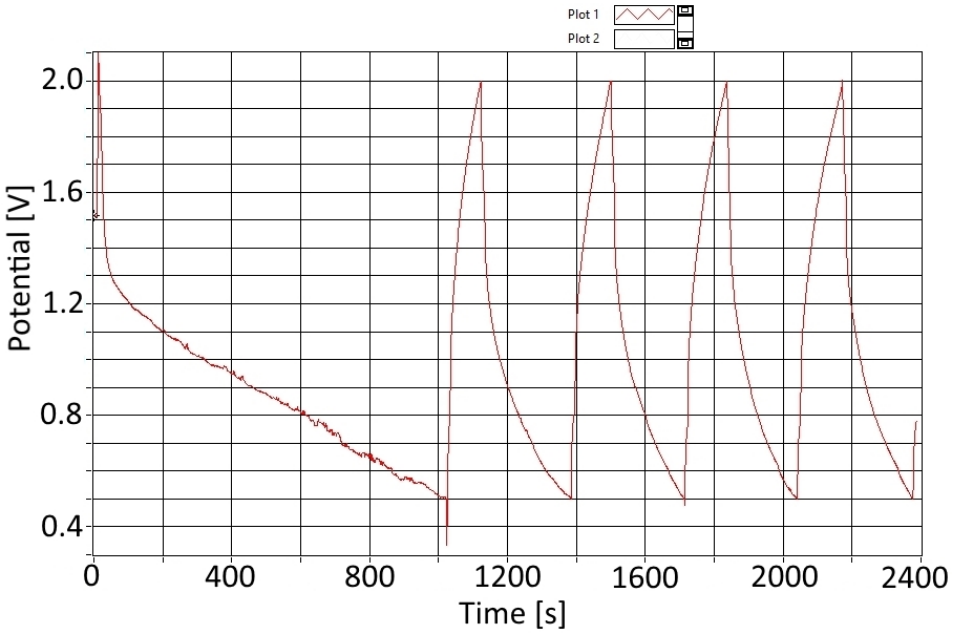

Figure 4.13: *As seen in Figure 4.12 above, the applied current was set to 0.6 mA. Just like previously observed, the first cycle lasted significantly longer compared to the following cycles and thus consumed a greater charge.*

washed off without damaging the underlying electrodes. Therefore, direct imaging was only possible before the tests, as had been done in Figure 4.2. Advanced equipment to observe the development of the solid-electrolyte interphase and alterations of the surface topology during cycling has recently been developed, but was not available during the course of this investigation.

This concluded the work done on the SnS_2 system. In the next part of the work, the second system, the hybrid lithium niobate nano-particles, is investigated.

Chapter 5

Lithium Niobates as Lithium Ion Battery Electrodes

5.1 Material Synthesis

The synthesis of the desired material involved two major steps. First, a lithium niobate precursor had to be produced. Second, the precursor material had to be subjected to sulfidisation in order to create thin outer layers of niobium sulfide on the powder grains of the material.

5.1.1 Synthesis of the Lithium Niobate Precursor

The main objective in creating the lithium niobate precursor was to obtain a material of sufficiently small particle sizes, which could then be sulfidised and successfully tested in a lithium ion battery prototype. The particle size was of importance, because the smaller the particle size, the easier and faster the sulfidisation of the material grains would take place due to the increased total surface area compared to the weight of the material. Sufficiently small particle sizes also required the use of electron microscopy for the physical characterisation of the nano-particles. In the electrochemical testing phase, small particle sizes is also helpful (as in the case of SnS_2) in alleviating the problems caused by the volume expansion/contraction of the particles due to the uptake/discharge of lithium ions during battery cycling, thus contributing to a prolonged battery lifetime.

In order to ensure small and homogeneous particle sizes on a nano-scale, a hydrothermal approach was chosen, as the well-controlled precipitation from a liquid phase seemed best suited for achieving this aim. For the synthesis of the lithium niobate powder, commercially available niobium pentoxide powder (Sigma Aldrich,

Niobium(V) oxide, 99.99% trace metals basis), water and lithium hydroxide (Sigma Aldrich, Lithium hydroxide, reagent grade, 98%) grains were mixed. The reactions leading to the synthesis of lithium niobate took place according to the following reaction pathways [Magrez et al. [2006]]:

$$3Nb_2O_5 + 8OH^- \rightarrow Nb_6O_{19}^{8-} + 4H_2O \tag{5.1}$$

$$Nb_6O_{19}^{8-} + 34OH^- \rightarrow 6NbO_6^{7-} + 17H_2O \tag{5.2}$$

$$NbO_6^{7-} + Li^+ + 3H_2O \rightarrow LiNbO_3 + 6OH^- \tag{5.3}$$

This reaction scheme allowed for the calculation of the required amounts of material, while care had to be taken to consider the requirements of each separate reaction step. However, as was pointed out by Magrez et al. [2006] in the case of potassium niobates, variations in stochiometries could have an effect on the overall morphology of the synthesised product. Therefore, morphological characterisations of the products were carried out after each synthesis.

After an initial trial and error optimisation phase, the production of the lithium niobate needed was chosen to be based on the following procedure: dissolution of 500 mg of lithium hydroxide in 40 ml of distilled water, followed by stirring for 4 hours. 500 mg of niobium pentoxide was then added and the mixture was stirred for another hour before being filled into a Teflon-lined autoclave (see Figure 5.1). The autoclave was sealed and heated to 160°C for a time period ranging from 24 to 120 hours (various times were tested to determine the right dwell time for the formation of lithium niobate). After this heating period, the autoclave was allowed to return to room temperature naturally and the contents were washed with ethanol and distilled water. The white precipitate was collected using vacuum filtration and dried at 40°C overnight.

For control purposes and with the goal of having an independent source of well-characterised lithium niobate, commercially available lithium niobate (Sigma Aldrich, Lithium niobate, 99.9% trace metal basis) was used as a second route to obtain a precursor. Upon receipt, it was realised that the particle size of the commercially available material was not sufficiently small. It consisted of small crystals similar in size to caster sugar, with particle sizes in the order of magnitude of 1 mm, whilst the project required particle sizes in the range of tens of nanometres. Both hand grinding (using an agate mortar and pestle) and automated grinding (using a ball mill such as shown in Figure 5.2) were tested as possible routes to

Figure 5.1: *A photo taken of the Teflon-lined autoclave used for the hydrothermal synthesis of lithium niobate nano-particles. The total internal volume was 50 ml.*

reduce particle sizes. Both methods produced similar particle size, but as the ball mill was found to produce negligible amounts of contamination in the powder with a greater homogeneity in particle sizes, only this alternative to reduce the size of the commercial powder grains for the remainder of the project was employed. Hand grinding was excluded due to the greater spread in particle size obtained using this route.

Both routes, synthesised and bought lithium niobate, delivered suitable and comparably fine white powders, which then were both used for the subsequent sulfidisation step.

5.1.2 Sulfidisation of the Lithium Niobate Precursor

For the sulfidisation of the lithium niobate, a simple short-time exposure to dihydrogen sulfide gas at elevated temperatures in the range of 700 to 800°C was chosen. Due to the small amounts necessary and the dangerous and corrosive nature of dihydrogen sulfide, it was decided to produce the required quantities of gas in-house.

The production of dihydrogen sulfide was set up by making use of the following reaction between iron sulfide and concentrated hydrochloric acid [Heinen and

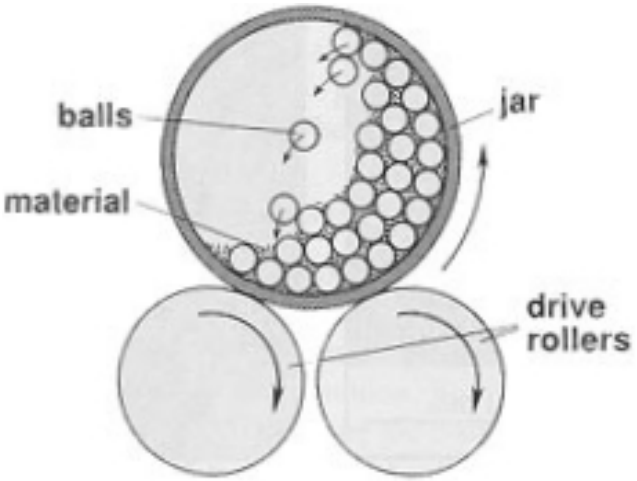

Figure 5.2: *In order to lower the average particle size of commercially available lithium niobate, a ball mill system was used. The ball mill consisted of a ceramic container and ceramic grinding balls. From [German [1984]]*

Lauwers [1996]]:

$$FeS + 2HCl \rightarrow FeCl_2 + H_2S \tag{5.4}$$

The apparatus used to house the reaction and collect the produced gas was a Kipp's Apparatus as illustrated in Figure 2.20. The reaction and collection took place in the middle chamber, while the reaction was controlled by the gas pressure in this chamber. When the middle valve was turned, H_2S was released into the connected section of the experimental set-up.

The gas flow was controlled via a turn valve and a glycerin-filled Dreschel bubbler, which allowed the monitoring of the flow rate. The gas was then introduced into a quartz glass tube, containing an alumina boat filled with the lithium niobate precursor material, inside a tube furnace. After the gas had passed over the precursor sample, it was pumped through a series of Dreschel bubblers filled with bleach and potassium permanganate, as can be seen in Figure 5.3. The reactions of any residual H_2S with both substances ensured that no toxic gas was released into the environment [Day [2003]]:

$$H_2S + 4ClO^- \rightarrow HSO_4^- + H^+ + 4Cl^- \tag{5.5}$$

Equation (5.5) described the reaction of hydrogen sulfide with bleach. The reaction of H_2S with potassium permanganate was a bit more complex and could have taken two different routes, depending on the acidity of the environment [Ed-

wards et al. [2002]]:

$$3H_2S + 2KMnO_4 \rightarrow 3S + 2H_2O + 2KOH + 2MnO_2 \tag{5.6}$$

$$3H_2S + 8KMnO_4 \rightarrow 3K_2SO_4 + 8MnO_2 + 2KOH + 2H_2O \tag{5.7}$$

Equation (5.6) corresponded to the reaction in an acidic environment, while Equation (5.7) described the same process in an alkaline solution. As a result, any remaining H_2S gas leaving the furnace was neutralised.

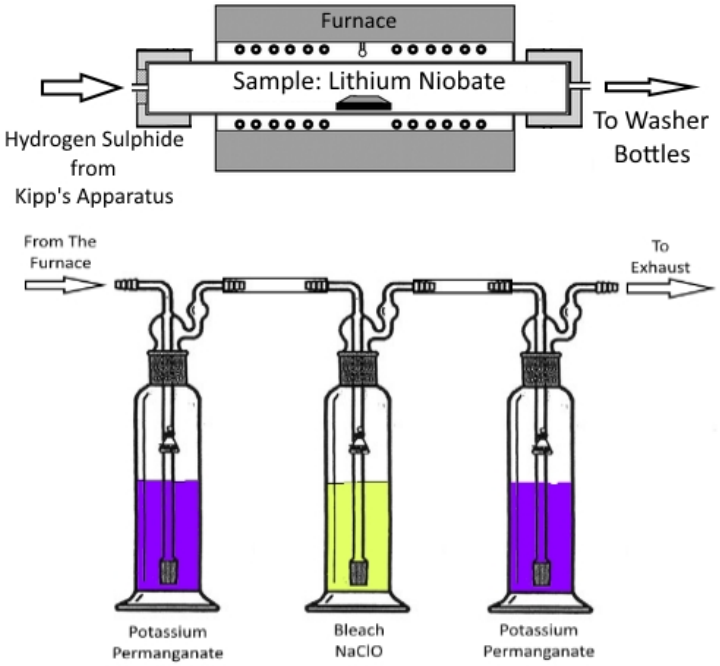

Figure 5.3: *The schematic breakdown of the sulfidisation rig. The Kipp's apparatus generated H_2S and fed it to the furnace, where it passed over the sample before it was neutralised on its journey through the three scrubber bottles. Adapted using: [AT-MAR Glass Inc. [2014]; Moore and Wang [2006]]*

During a typical sulfidisation run, the sample was inserted into the furnace and all valves were sealed. For 10 minutes, the entire system was purged with nitrogen gas to ensure that no oxygen or other contaminating gases were present during the heating phase. The furnace was then ramped to 800°C while the nitrogen was still being pumped through the system. Once the target temperature was reached and held stable, the nitrogen was turned off and the valve to the Kipp's Apparatus opened. Bubble size and frequency in the glycerine control bubbler

were registered and converted into a flow rate. The flow rates varied slightly from experiment to experiment, but stayed in the range from 20 to 30 ml/min. The flow of H_2S was maintained for a pre-determined period of time (from 15 minutes to 3 hours) and then exchanged for nitrogen gas again as the furnace was shut down. Once the sample had reached room temperature naturally, it was collected and readied for characterisation. A full schematic of the process is depicted in Figure 5.3.

5.2 Morphological Characterisation

5.2.1 Characterisation of Lithium Niobate Precursor

Both the characteristics of the lithium niobate precursor material obtained via the hydrothermal synthesis as described in Section 5.1.1 and the purchased, ball-milled powder needed to be examined before progressing further to the sulfidisation stage.

For each precursor batch used, a brief examination of the average particle size was carried out to ensure that respective powder grains were sufficiently small. Sample images for synthesised and purchased powders respectively were taken and are shown in Figure 5.4 and Figure 5.5.

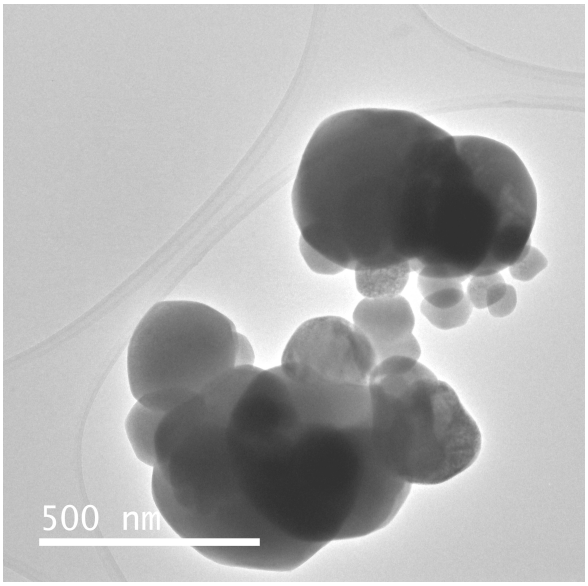

Figure 5.4: *A transmission electron microscope image showing a typical distribution of synthesised $LiNbO_3$ particles. The particles were observed to have diameters ranging from as small as 50 nm to 700 nm. Noteworthy was the spherical shape of the particles.*

Results obtained showed that synthesised lithium niobate particles were in

the size range of 50 nm to 700 nm, while the ball milled purchase particles reached diameters of 200 nm to 3 microns. The analysis under the TEM were carried out at 80keV.

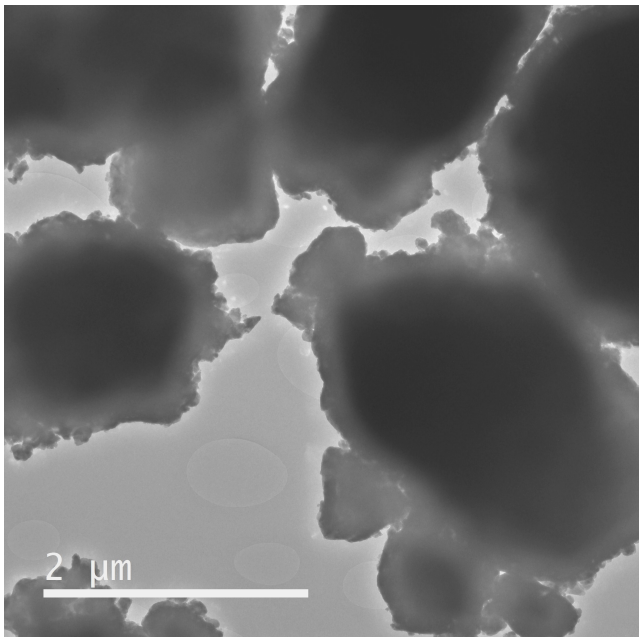

Figure 5.5: *A transmission electron microscope image of a typical cluster of bought and ball-milled lithium niobate particles. Unlike their synthesised counterparts as seen in Figure 5.4, these particles could reach several micrometres in diameter and had jagged edges.*

Monte Carlo simulations using 200 electrons and accelerating voltages of 10 - 20 keV were performed to ensure EDX could be performed. The results can be seen in Figure 5.6.

The purchased material was briefly investigated using quantitative EDX and it showed a ratio of 1:3 for Nb:O as would be expected of a pure sample. When the same experiment was conducted using the synthesised lithium niobate, some variations in the stochiometry arose. Some synthesised samples proved to have a good ratio of 1:3 for Nb:O, such as seen in Figure 5.7. However, in some cases the ratio went up to 1:4, for example as seen in Figure 5.8, which suggested contamination of the sample with other niobium oxides.

An elemental map was collected to determine the locations of the main elements present in the sample. An area was chosen at the border of a bigger pile of particles so that signals both from the bulk and from dispersed particles could be collected at the same time. The maps are shown in Figure 5.9. They show the

secondary electron image of the area of interest, as well as maps for aluminium, niobium and oxygen. As expected, niobium and oxygen were fairly well-confined to the particles, while aluminium was only visible where the bare substrate was visible. Noteworthy was that this meant that any additional oxygen in the collected spectra couldn't result from aluminium oxides. The additional oxygen could therefore only come from a combination with any of the other elements present in the spectrum. This made the presence of other niobium oxides very likely.

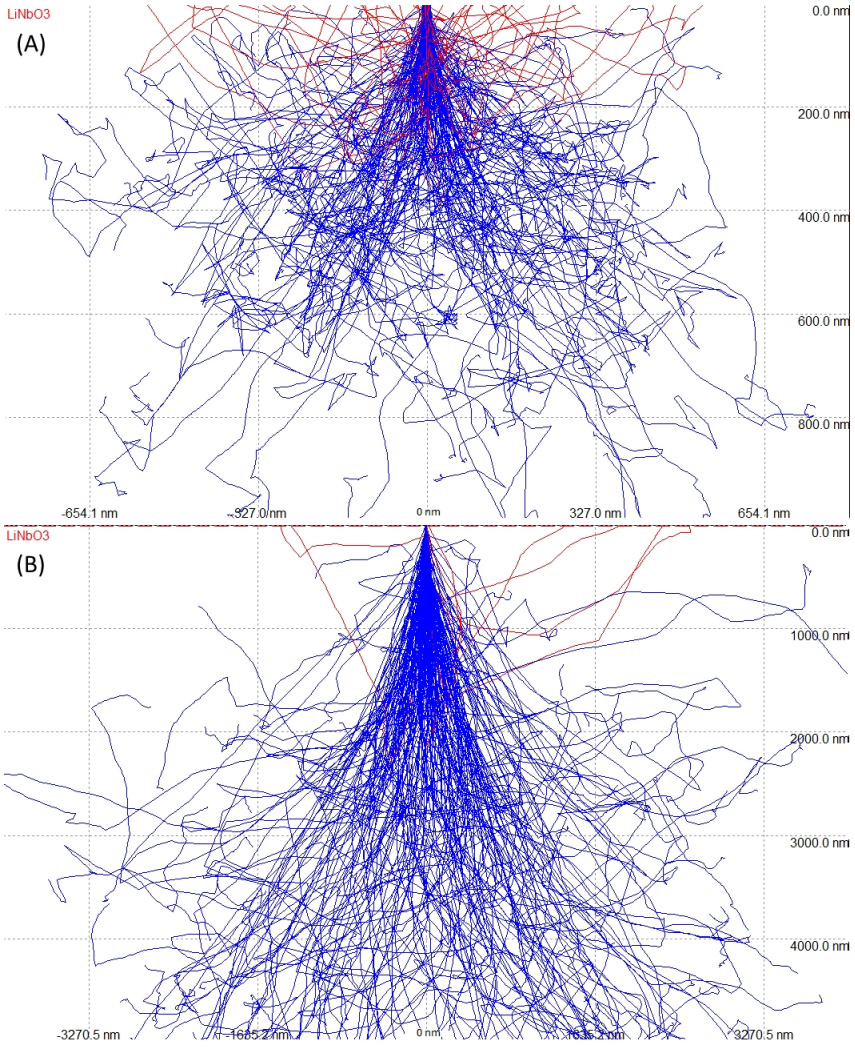

Figure 5.6: *Monte Carlo simulations for $LiNbO_3$ using 200 electrons accelerated at 10 keV (A) and 20 keV (B). Blue trajectories correspond to electrons that are eventually absorbed into the material, while red trajectories correspond to electrons leaving the sample again.*

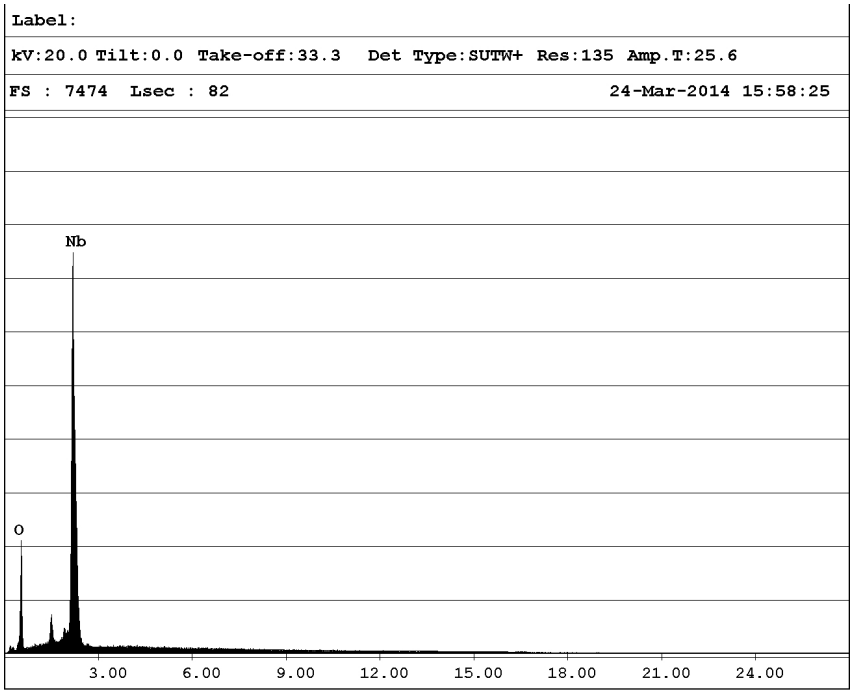

Element	Wt %	At %	K-Ratio	Z	A	F
O K	36.06	76.61	0.0617	1.1370	0.1505	1.0002
NbL	63.94	23.39	0.5817	0.8882	1.0243	1.0000
Total	100.00	100.00				

Figure 5.7: *An EDX spectrum collected for the synthesised lithium niobate samples together with the raw data provided from the experiment. The ratio between niobium and oxygen was roughly 23:77, which was close to the expected value of 1:3. This suggested the desired sample composition for lithium niobate.*

In order to shed further light on the composition of the synthesised samples, XRD spectra were collected both for the pure, commercial lithium niobate powder and the synthesised material. The spectrum for the material obtained from Sigma Aldrich showed clean and clear peaks that corresponded to what was expected for lithium niobate and is shown in Figure 5.10. In comparison to this, the spectrum obtained for the hydrothermally synthesised material was noisy and contained a great number of additional peaks, as shown in Figure 5.11. While it wasn't possible to rule out that there was at least a minor presence of lithium niobate in the sample, it became clear that the synthesis method needed to be adjusted. However, even after several attempts to change the parameters of the synthesis, no visible improvement could be noted.

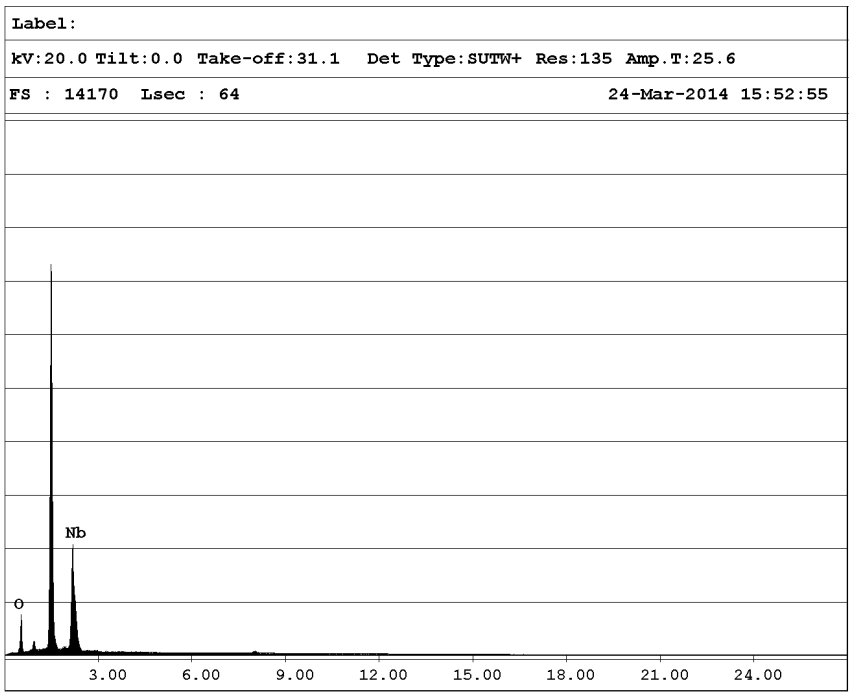

Element	Wt %	At %	K-Ratio	Z	A	F
O K	41.89	80.72	0.0746	1.1212	0.1589	1.0002
NbL	58.11	19.28	0.5223	0.8735	1.0289	1.0000
Total	100.00	100.00				

Figure 5.8: *A spectrum collected from the same sample as in Figure 5.7 together with a printout of the raw quantification data, but from a different area. In this area, the ratio between Nb:O was roughly 19:81 and so close to 1:4. This suggested the presence of other niobium oxides in the sample. The strong, unlabelled peak was Silicon, which was not used in the calculations.*

It was still decided to attempt to sulfidise both types of samples, even though the synthesised material contained a variety of additional, different niobium oxides.

5.2.2 Characterisation of Sulfidised Lithium Niobate

Sulfidised Synthesised Lithium Niobate

Synthesised lithium niobate powder was subjected to dihydrogen sulfide at 800 °C for a duration of variable length. Initial runs were set to last 15 minutes, but subsequent TEM analysis showed no build up of sulfidised layers on the particle surface. By increasing the dwell time to 1 hour as well as raising the furnace temperature to 825 °C, it was possible to observe the growth of several layers of material around the sample (see Figure 5.12):

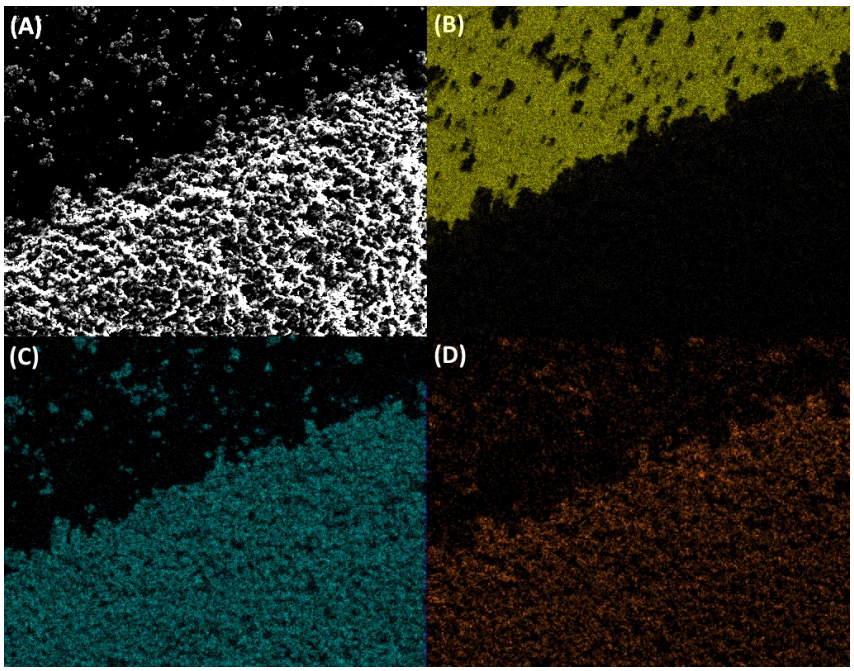

Figure 5.9: *An elemental map was collected to determine the confinement of elements to certain areas of the sample. The four images corresponded to: (A) Secondary electron image; (B) Aluminium locations; (C) Niobium locations; (D) Oxygen locations. SEM was carried out at 20keV.*

The TEM image in Figure 5.12 also demonstrates that the overall particle morphology was not impacted severely by the sulfidisation process and that the built-up layers formed a roughly homogeneous skin around the particles. The particles did not change their overall morphology from their unsulphidised state. They were roughly spherical with diameters ranging from 50 nm to about 500 nm. TEM analysis was undertaken at 80 keV.

Unfortunately, sufficient time was not available to further optimise the sulfidisation parameters with a view to initiate more pronounced sulfide layer growth on the synthesised lithium niobate powder.

5.3 Electrochemical Analysis

Even though time for the research project was running out, an attempt at an electrochemical analysis of sulfidised lithium niobate was still made. For this purpose, material obtained via sulfidising the commercially available lithium niobate was used in a set-up similar to the work done on SnS_2.

The powdered material was carefully washed and dried to ensure that no

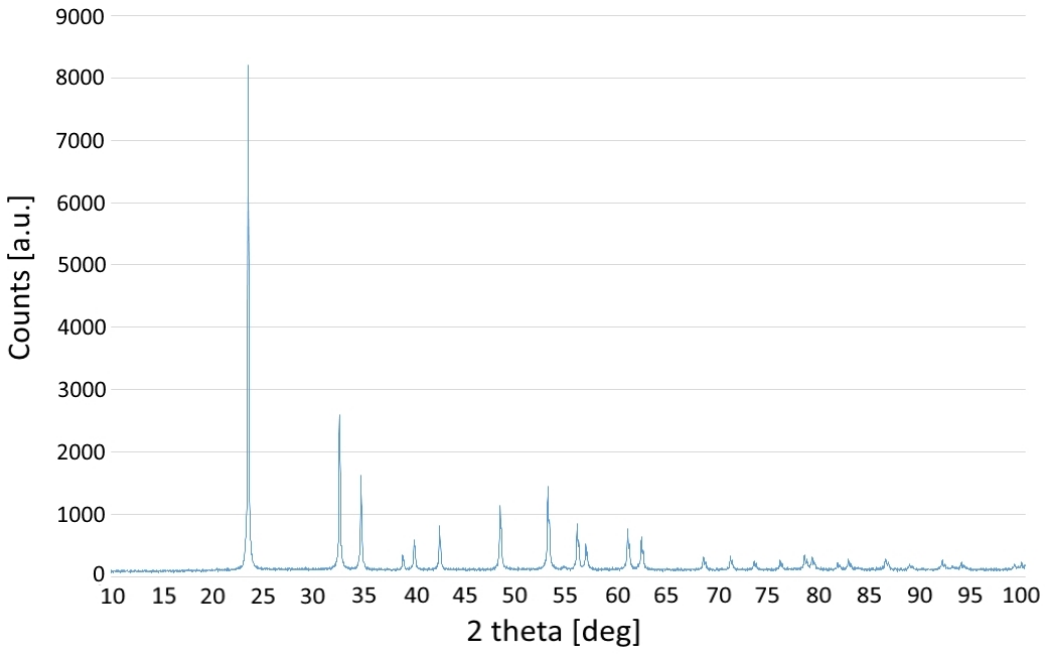

Figure 5.10: *An XRD spectrum collected from the commercial lithium niobate sample, which was obtained from Sigma Aldrich.*

contamination from atmospheric water was present. This was done by first drying it under vacuum at 40°C for 4 hours and then transferring it to an argon-filled glove box, where it was left to continue drying at room temperature overnight. The final powder was weighed and mixed with polyvinylidene fluoride and carbon black in the ratio of 70:15:15 (Active material : Carbon Black : PVDF). The mixing phase occurred in an agate mortar and produced a coarse dark-grey powder. Special care was taken not to apply too much force during the mixing, as it was feared that this could shear the thin sulfidised layers off the surface of the sulfidised lithium niobate particles.

N-methyl-pyrrolidinone was added in small drops to the mixed powder until a smooth slurry was created. The slurry was cast onto a copper current collector foil and left to dry under vacuum at 40°C overnight.

At this stage, the first major problems became apparent in the form of severe cracking. During the drying process, the electrodes went through a phase of strong contraction, which was believed to be the cause of the cracking. By thinning out the electrode slurry with more N-methyl-pyrrolidinone, it was observed that the cracks became smaller in size. Furthermore, by physically spreading the electrode slurry over a bigger surface, a further improvement could be registered. A strong reaction with the copper substrate was not observed.

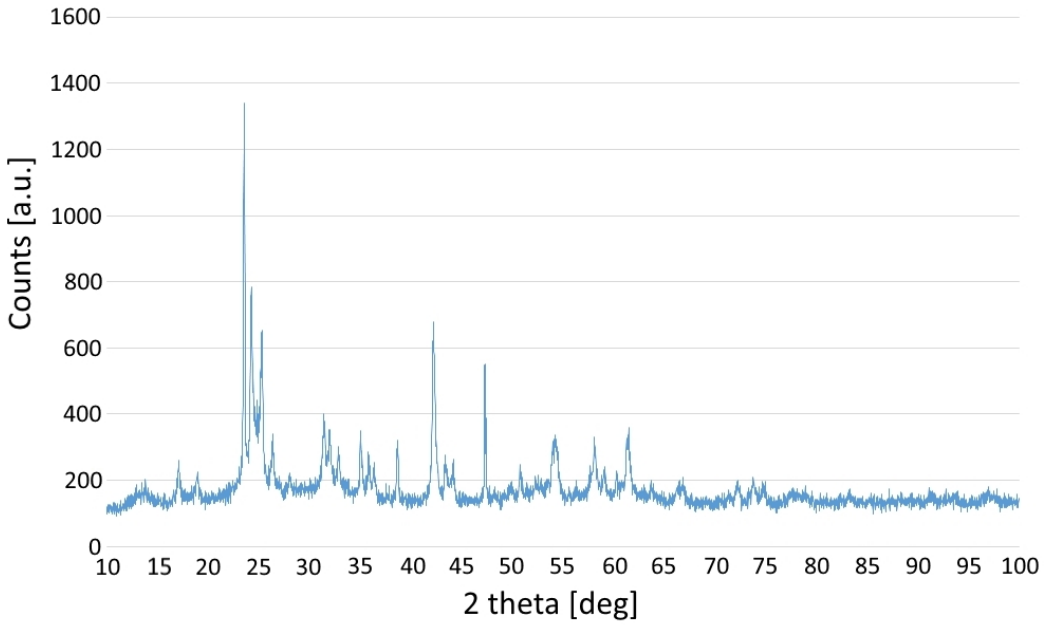

Figure 5.11: *An XRD spectrum collected from one of the in-house synthesised lithium niobate samples.*

It was possible to obtain a few good electrode foils this way, which were then cut into a set of circular disks with diameter 18 mm. The weight of each electrode was determined via weighing the disk and then subtracting the weight of a copper disk of the same dimensions as the electrode. Typical amounts of active material were in the range of 2 to 3 mg per electrode.

However, it should be noted that even these improved electrodes were still suffering from small fractures and showed signs of feeble connection to the copper current collector.

Typical CR2016 coin cells were used in the electrochemcial testing. The electrodes were combined with a porous polypropylene separator supplied by Cellgard and a lithium metal counter electrode. The battery assembly took place in an argon-filled glove-box for safety and contamination reasons. The electrolyte was a 1M mixture of lithium hexafluorophosphate in an ethylene carbonate and diethyl carbonate carrier solution. Ethylene carbonate and diethyl carbonate were present in a ratio of 1:1 w/w. The cells were assembled, crimped at 800 psi and then taken out of the glove-box.

Electrochemical testing was performed on a potentiostat supplied by MTI. However, it was not possible to collect clean data from the cells due to the early onset of cell failures. It is believed that the main cause for cell failure was the observed

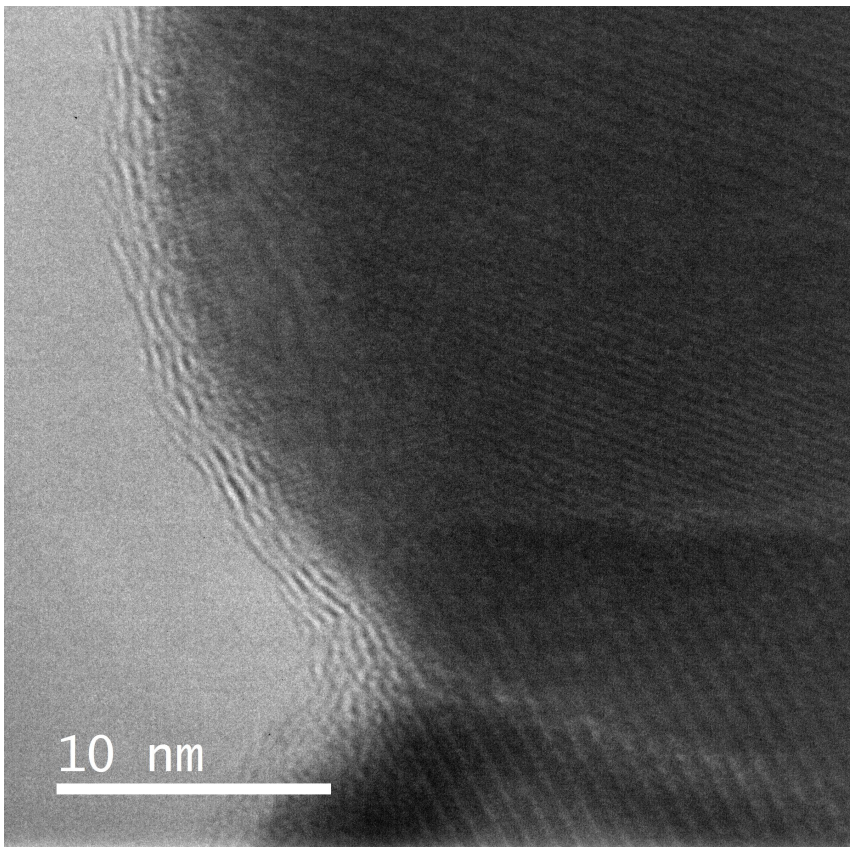

Figure 5.12: *A transmission electron microscopy image showing the build-up of several surface layers around the outside of a synthesised lithium niobate nano-particle. A weak sulfide signal could be detected with EDX, but it was drowned out by the strong signal from the core of the particle.*

cracking, which may have caused loose contacts and variable electrode sizes.

At this point in time the experimental work was concluded due to the nearing end of the research period of the project. The last part of the work was to summarise and to evaluate the outcome of the whole work undertaken during the project.

Chapter 6

Conclusions

6.1 Summary of Work Done

During the course of this project it was possible to gain several valuable insights. A short summary of these will be given here.

Chapter 3 provides an introduction to the work on novel morphologies of SnS_2 nano-particles. It was possible to grow several different morphologies using a hydrothermal route: Nano-flowers, nano-platelets, flower-type nano-sheets and nano-worms. The former three had already been discovered, characterised and described in the literature (see Chapter 2 for the respective references). Nano-worms, however, had not yet been described in literature, and it was possible to synthesise two different types of worms. A facile route to their synthesis using low-cost reagents was developed and it was demonstrated that they can be grown over a large range of synthesis parameters, including at room temperature. Advanced electron microscopy and x-ray techniques were used to characterise the composition and topology of these nano-worms and determined their average dimensions. A successful growth study was able to provide a rational theory of the growth mechanism behind the synthesis of these nano-worms. The ratio between surface area and volume was investigated successfully by the development of a computational simulation of their topology. The work has provided a good understanding of the nano-worm morphology and a solid basis for future work to expand existing knowledge in the field.

In Chapter 4, the synthesised SnS_2 nano-worms were used to investigate their lithium ion storage properties. For this, two different designs of SnS_2 prototype test cells were produced. It was possible to perform proof-of-concept experiments confirming the possibility of lithium intercalation in SnS_2 nano-worms. Further,

it was possible to demonstrate good cell stability during cyclic voltammetry and several previously unknown peaks in these cyclic voltammograms were discovered. Galvanostatic cycling revealed cell capacities below what had been reported for other SnS_2 morphologies, but strong variations in test results indicated that under certain conditions the precise cell capacity could be significantly higher.

In Chapter 5, lithium niobate nano-powder and its sulfidisation were investigated. An attempt was made to synthesise lithium niobate nano-particles via a hydrothermal approach. While lithium niobate was not purely produced, hard nano-spheres of niobium oxide were synthesised, which may be of interest to other researchers. The research was continued using commercially available lithium niobate and it was possible to produce good initial sulfidisation results by tuning the parameters of the designed sulfidisation apparatus. This resulted in the growth of several layers of material around the nano-particles, thus creating the desired lithium niobate hybrid. Unfortunately, time ran out before large-scale sulfidisation was possible, but it was still possible to lay the groundwork for both this and the subsequent testing of the material in lithium ion test cells.

6.2 Suggestions for Future Work

As SnS_2 is a material with several interesting properties, a range of potential future projects could be pursued. First of all, a continued investigation of the lithium ion storage properties of SnS_2 could result in the development of very potent lithium ion anodes and thus batteries.

SnS_2 has also been under investigation in terms of its gas sensing properties [Shi et al. [2006b]], and several prototype gas sensors based on it have already been produced and tested. The nano-worm morphology could be particularly suited to this application because of its large surface area. Additionally, due to their well-defined cylindrical shapes, SnS_2 nano-worms may also prove to be easier to integrate into the necessary gas sensing circuits.

Finally, large surface areas are of interest in catalytic chemistry. It may be possible to develop SnS_2 nano-worm catalysts to boost reaction rates for specific types of reactions. A good start for this may be to continue the investigation into the interaction of SnS_2 with nitrogen, which has led to the interesting results during the BET measurements.

A particularly interesting field of future work could be to elucidate the mechanisms which led to nano-worm growth first along their axes, and then later perpendicular to them. This could lead to reinforced nano-worm structures and thus

broaden their field of application.

The work on sulfidised lithium niobate is still in its early stages. A primary topic of future work would be to continue to investigate the sulfidisation of nanoparticles and to further examine their suitability as lithium ion battery electrode materials.

Sulfidised lithium niobate may also prove to be a good lubricant in a similar fashion to tungsten sulfide (WS_2), as the outer layers of the structure seem to be easily rolled off due to their weak adhesion based on Van-der-Waals-forces.

As lithium niobate is commonly used for its optical properties, it may prove useful to investigate what impact a handful of layers of sulfidised material could have on these properties.

6.3 Impact on Society

As already highlighted in Chapter 1, the world is currently going through a phase where strongly growing energy demand, growing concerns about meeting this demand and concerns about the environment all affect modern energy policy. It has therefore become more important than ever to find efficient ways of storing and distributing energy. The predominant energy carriers of the last century, fossil fuels, are slowly being replaced with greener versions relying on electrical energy. This work has made an impact in the field of lithium ion storage, which is a significant technology in today's energy storage field. The work may in future be used to construct better, more stable lithium ion batteries, which could have a positive global impact. Furthermore, as laid out in the section on future work above, this work may provide the foundation of research branching out from the original goal of this project.

Glossary

2D Two Dimensional.

3D Three Dimensional.

ADF Annular Dark Field.

ADF ET Annular Dark Field Electron Tomography.

BET Brunauer-Emmett-Teller method.

BF Bright Field.

CCD Charge-Coupled Device.

CV Cyclic Voltammetry.

DEC Diethyl Carbonate.

DF Dark Field.

EC Ethylene Carbonate.

EDAX Energy-Dispersive X-Ray Spectroscopy.

EDS Energy-Dispersive X-Ray Spectroscopy.

EDX Energy-Dispersive X-Ray Spectroscopy.

EDXS Energy-Dispersive X-Ray Spectroscopy.

EELS Electron Energy-Loss Spectroscopy.

EIS Electrochemical Impedance Spectroscopy.

FEG Field Emission Gun.

GC Galvanostatic Cycling.

Ge(Li) Lithium-Doped Germanium Crystal.

HAADF High-Angle Annular Dark Field.

HRTEM High Resolution Transmission Electron Microscopy.

JCPDS Joint Committee on Powder Diffraction Standards.

LCO Lithium Cobalt Oxide.

LIB Lithium Ion Battery.

LIP Lithium Iron Phosphate.

LiTFSI Lithium (trifluormethylsulfone)-imide.

LMNCO Lithium Nickel Manganese Cobalt Oxide.

LMO Lithium Manganese Oxide.

LNCA Lithium Nickel Cobalt Aluminium.

LTO Lithium Titanate Oxide.

LVP Lithium Vanadium Phosphate.

NA Numerical Aperture.

NMP N-Methyl Pyrrolidinone.

PVDF Poly Vinylidene Fluoride.

SDD Silicon Drift Detector.

SEI Solid-Electrolyte Interphase.

SEM Scanning Electron Microscope.

Si(Li) Lithium-Doped Silicon Crystal.

SSD Solid State Detector.

STEM Scanning Transmission Electron Microscope.

TEM Transmission Electron Microscope.

UN United Nations.

WURC Warwick University Rifle Club.

WWII World War 2.

XRD X-ray Powder Diffraction.

Bibliography

Agar Scientific (2014). Square Mesh Grids - Copper. Adapted from: `http://www.agarscientific.com/tem/grids-agar.html`; Accessed: 07/12/2014.

Airy, G. (1835). On the Diffraction of an Object-glass with Circular Aperture. *Transactions of the Cambridge Philosophical Society*.

Amatucci, G., Tarascon, J., and Klein, L. (1996). CoO_2, The End Member of the Li_xCoO_2 Solid Solution. *Journal of The Electrochemical Society*, 143(3):1114–1123.

Antoine, C. (1888). Tensions des Vapeurs; Nouvelle Relation entre les Tensions et les Températures. *Comptes Rendus des Séances de l'Académie des Sciences*, 107.

Arrhenius, S. (1889). *Über die Dissociationswärme und den Einfluss der Temperatur auf den Dissociationsgrad der Elektrolyte*. Wilhelm Engelmann.

AT-MAR Glass Inc. (2014). Bottle. `http://www.atmarglass.com/xcart/Bottle/`; Accessed: 20/12/2014.

Avadhanulu, M. and Kshirsagar, P. (1992). *A Textbook Of Engineering Physics For B.E., B.Sc.* S. Chand and Company Ltd., New Dehli.

Balbuena, P. and Wang, Y. (2004). *Lithium-Ion Batteries: Solid-Electrolyte Interphase*. World Scientific Publishing, Singapore.

Bard, A. and Faulkner, L. (2000). *Electrochemical Methods: Fundamentals and Applications*. John Wiley & Sons, Hoboken (USA), 2nd edition.

Basu, S. (1981). Rechargeable battery (US4304825 A). *United States Patent*.

Basu, S., Zeller, C., Flanders, P., Fuerst, C., Johnson, W., and Fischer, J. (1979). Synthesis and Properties of Lithium-Graphite Intercalation Compounds. *Materials Science and Engineering*, 38(3):275 – 283.

Beckhoff, B., Kanngiesser, B., Langhoff, N., Wedell, R., and Wolff, H. (2006). *Handbook of Practical X-ray Fluorescence Analysis*. Springer.

Besenhard, J. (1976). The Electrochemical Preparation and Properties of Ionic Alkali Metal- and NR_4-Graphite Intercalation Compounds In Organic Electrolytes. *Carbon*, 14(2):111 – 115.

Besenhard, J. and Eichinger, G. (1976). High Energy Density Lithium Cells: Part I - Electrolytes and Anodes. *Journal of Electroanalytical Chemistry and Interfacial Electrochemistry*, 68(1):1 – 18.

Besenhard, J. and Fritz, H. (1974). Cathodic Reduction of Graphite in Organic Solutions of Alkali and NR_4^+ Salts. *Journal of Electroanalytical Chemistry and Interfacial Electrochemistry*, 53(2):329 – 333.

Besenhard, J. and Schöllhorn, R. (1977). The Discharge Reaction Mechanism of the MoO_3 Electrode in Organic Electrolytes. *Journal of Power Sources*, 1(3):267 – 276.

Bletskan, D. (2005). Phase equilibrium in binary systems aivbvi. *Journal of Ovonic Research Vol*, 1(5):47–52.

Brain, M. (2006). How Lithium-ion Batteries Work. *HowStuffWorks.com*. `http://electronics.howstuffworks.com/everyday-tech/lithium-ion-battery1.htm`; Accessed: 07/12/2014.

British Petroleum (2014). *Statistical Review of World Energy 2014*. British Petroleum. `http://www.bp.com/en/global/corporate/about-bp/energy-economics/statistical-review-of-world-energy/statistical-review-downloads.html`; Accessed: 25/04/2015.

Bronstein, I. and Semendjajew, K. (1984). *Taschenbuch der Mathematik*. Verlag Harri Deutsch, Frankfurt am Main (Germany).

Brousse, T., Retoux, R., Herterich, U., and Schleich, D. (1998). Thin-Film Crystalline SnO2-Lithium Electrodes. *Journal of The Electrochemical Society*, 145(1):1–4.

Brunauer, S., Emmett, P., and Teller, E. (1938). Adsorption of Gases in Multimolecular Layers. *Journal of the American Chemical Society*, 60(2):309–319.

Brunk, U., Collins, V., and Arro, E. (1981). The Fixation, Dehydration, Drying and Coating of Cultured Cells for SEM. *Journal of Microscopy*, 123(2):121–131.

Bullen, H. (2008). Basic Theory: Instrument Design. http://www.asdlib.org/onlineArticles/ecourseware/Bullen_XRD/LearningActivity_Instrumentation.pdf. Accessed: 07/12/2014.

Bundy, C., Graham, R., Kuehn, S., Precit, R., and Rogers, M. (1990). *Lithium Niobate Explosion Monitor*. Google Patents. US Patent 4,893,049.

Byrappa, K. and Yoshimura, M. (2012). *Handbook of Hydrothermal Technology*. William Andrew.

Caceres-Valencia, P. (2006). *Scanning Electron Microscopy and Ancilliary Techniques*. University of Puerto Rico.

Campos, J., Beidaghi, M., Hatzell, K., Dennison, C., Musci, B., Presser, V., Kumbur, E., and Gogotsi, Y. (2013). Investigation of carbon materials for use as a flowable electrode in electrochemical flow capacitors. *Electrochimica Acta*, 98(0):123 – 130.

Cargille, J. (1964). Immersion Oil and the Microscope. *New York Microscopical Society Yearbook*.

Chagnes, A., Carré, B., Willmann, P., and Lemordant, D. (2002). Modeling Viscosity and Conductivity of Lithium Salts in γ-Butyrolactone. *Journal of Power Sources*, 109(1):203 – 213.

Chan, C., Peng, H., Liu, G., McIlwrath, K., Zhang, X., Huggins, R., and Cui, Y. (2007). High-Performance Lithium Battery Anodes using Silicon Nanowires. *Nature nanotechnology*, 3(1):31–35.

Chang, H. and Wang, L. (2010). A Simple Proof of Thue's Theorem on Circle Packing. *arXiv preprint arXiv:1009.4322*. Accessed: 20/12/2014.

Chen, C., Liu, J., Stoll, M., Henriksen, G., Vissers, D., and Amine, K. (2004). Aluminium-Doped Lithium Nickel Cobalt Oxide Electrodes for High-Power Lithium-Ion Batteries. *Journal of Power Sources*, 128(2):278 – 285.

Chen, H., Qiu, X., Zhu, W., and Hagenmuller, P. (2002). Synthesis and High Rate Properties of Nanoparticled Lithium Cobalt Oxides as the Cathode Material for Lithium-Ion Battery. *Electrochemistry Communications*, 4(6):488 – 491.

Chen, J. and Whittingham, M. (2006). Hydrothermal Synthesis of Lithium Iron Phosphate. *Electrochemistry Communications*, 8(5):855 – 858.

Choi, H., Jung, Y., Noda, I., and Kim, S. (2003). A Study of the Mechanism of the Electrochemical Reaction of Lithium with CoO by Two-Dimensional Soft X-ray Absorption Spectroscopy (2D XAS), 2D Raman, and 2D Heterospectral XAS-Raman Correlation Analysis. *The Journal of Physical Chemistry B*, 107(24):5806–5811.

Choi, S. and Jo, S. (2014). Lithium manganese oxide positive active material for lithium ion secondary battery and lithium ion secondary battery including the same. US Patent 8,778,536.

Corbari, L., Cambon-Bonavita, M., Long, G., Grandjean, F., Zbinden, M., Gaill, F., and Compère, P. (2008). Iron oxide deposits associated with the ectosymbiotic bacteria in the hydrothermal vent shrimp rimicaris exoculata. *Biogeosciences*, 5.

Crank, J. (1976). *The Mathematics of Diffusion (2ed)*. Oxford University Press, Oxford (UK).

Crewe, A. (1971). *Electron Microscopy in Materials Science*. Academic Press.

Darling, D. (2013). Kipp's apparatus. *Encyclopedia of Science*. `http://www.daviddarling.info/encyclopedia/K/Kipps_apparatus.html`; Accessed: 20/12/2014.

Darlington, E. (1975). Backscattering of 10-100 keV Electrons from Thick Targets. *Journal of Physics D: Applied Physics*, 8(1):85.

Day, E. (2003). *Synthesis and Characterisation of Inorganic Fullerene-type compounds from Alkali Metal Tungsten Bronzes*. PhD thesis, Lincoln College, University of Oxford.

Disher, B., Lenarduzzi, L., Lewis, B., and Teeuwen, J. (2006). The Physics of Computed Tomography. `http://web2.uwindsor.ca/courses/physics/high_schools/2006/Medical_Imaging/ctphysics.html`; Accessed: 07/12/2014.

Edwards, V., Velasco, C., and Jr., K. E. (2002). Solving the Hydrogen Sulfide Odor Problem. *Alken-Murray Corp.* `http://www.alken-murray.com/H2SFrameSet.html`; Accessed: 20/12/2014.

Egerton, R., Li, P., and Malac, M. (2004). Radiation Damage in the TEM and SEM. *Micron*, 35(6):399–409.

Eichinger, G. and Besenhard, J. (1976). High Energy Density Lithium Cells: Part II - Cathodes and Complete Cells. *Journal of Electroanalytical Chemistry and Interfacial Electrochemistry*, 72(1):1 – 31.

Elias, A., Perea-López, N., Castro-Beltrán, A., Berkdemir, A., Lv, R., Feng, S., Long, A., Hayashi, T., Kim, Y., and Endo, M. (2013). Controlled Synthesis and Transfer of Large-Area WS_2 Sheets: From Single Layer to Few Layers. *ACS nano*, 7(6):5235–5242.

EUROSTAT (2015). *Final energy consumption in EU-28 by sector*. EUROSTAT. `http://ec.europa.eu/eurostat/tgm/refreshTableAction.do?tab=table&plugin=0&pcode=tsdpc320&language=en`; Accessed: 25/04/2015.

Fauteux, D. and Koksbang, R. (1993). Rechargeable Lithium Battery Anodes: Alternatives to Metallic Lithium. *Journal of Applied Electrochemistry*, 23(1):1–10.

Fong, R., von Sacken, U., and Dahn, J. (1990). Studies of Lithium Intercalation into Carbons using Non-Aqueous Electrochemical Cells. *Journal of The Electrochemical Society*, 137(7):2009–2013.

Fultz, B. and Howe, J. (2007). *Transmission Electron Microscopy and Diffractometry of Materials*. Springer.

Gabriel, B. (1985). *SEM: A User's Manual for Materials Science*. ASM International, Materials Park (USA).

Gaudin, A. and Hamlyn, W. (1938). Pyrosynthesis, Identification, and Study of Tin Sulphides and of Compounds of Tin Sulphides with Antimony and Lead Sulphides. *Economic Geology*, 33(8):868–888.

German, R. (1984). *Powder Metallurgy Science*. MPFI, Princeton.

Gledhill, A., Reddy, K., Drexler, J., Shinoda, K., Sampath, S., and Padture, N. (2011). Mitigation of damage from molten fly ash to air-plasma-sprayed thermal barrier coatings. *Materials Science and Engineering: A*, 528(24):7214 – 7221.

Goldstein, J., Costley, J., Lorimer, G., and Reed, S. (1977). Quantitative X-ray Analysis in the Electron Microscope. *Scanning Electron Microscopy*, 1(315):24.

Goldstein, J., Newbury, D., Joy, D., Lyman, C., Echlin, P., Lifshin, E., Sawyer, L., and Michael, J. (2003). *Scanning Electron Microscopy and X-Ray Microanalysis*. Springer Science.

Goodenough, J. and Mizushima, K. (1981). Electrochemical Cell with new Fast Ion Conductors (US4302518 A). *United States Patent*.

Gratwohl, P. (1998). *Diffusion in natural porous media: Contaminant transport, sorption/desorption and dissolution kinetics*. Kluwer Academic.

Grivet, P., Bernard, M., Hawkes, P., and Septier, A. (1972). *Electron Optics*. Pergamon Press, Oxford (UK).

Grupen, C. and Buvat, I. (2012). *Handbook of Particle Detection and Imaging*. Springer.

Hafner, B. (2007). Scanning electron microscopy primer. *Characterization Facility, University of Minnesota-Twin Cities*, pages 1–29.

Hai, B., Tang, K., Wang, C., An, C., Yang, Q., Shen, G., and Qian, Y. (2001). Synthesis of SnS_2 Nanocrystals via a Solvothermal Process. *Journal of Crystal Growth*, 225(1):92 – 95.

Halliday, D., Resnick, R., and Walker, J. (2009). *Halliday Physik*. Wiley-VCH, Weinheim (Germany), 2nd edition.

Hamilton, S. (2013). Airbus Examines Lithium Battery Safety, Fire Suppression. *Leeham News and Comment*. `http://leehamnews.com/2013/01/28/airbus-examines-lithium-battery-safety-fire-suppression/`; Accessed: 07/12/2014.

Hammond, K. and Conner, W. (2013). Analysis of catalyst surface structure by physical sorption. *ADVANCES IN CATALYSIS, VOL 56*, 56:1–101.

Harding Energy (2004). *Harding Battery Handbook For Quest®Rechargeable Cells and Battery Packs*. Harding Energy Inc, Muskegon (USA).

Harris, L. (1968). Analysis of Materials by Electron-Excited Auger Electrons. *Journal of Applied Physics*, 39(3):1419–1427.

Heinen, W. and Lauwers, A. (1996). Organic Sulfur Compounds Resulting from the Interaction of Iron Sulfide, Hydrogen Sulfide and Carbon Dioxide in an Anaerobic Aqueous Environment. *Origins of Life and Evolution of the Biosphere*, 26(2):131–150.

Hickling, A. (1942). Studies in Electrode Polarisation: Part IV. - The Automatic Control of the Potential of a Working Electrode. *Trans. Faraday Soc.*, 38:27–33.

Holzwarth, U. and Gibson, N. (2011). The Scherrer Equation Versus the Debye-Scherrer Equation. *Nature Nanotechnology*, 6(9):534–534.

Hong, S., Popovitz-Biro, R., Prior, Y., and Tenne, R. (2003). Synthesis of SnS_2/SnS Fullerene-like Nanoparticles: A Superlattice with Polyhedral Shape. *Journal of the American Chemical Society*, 125(34):10470–10474.

Huang, J., Zhuang, T., Zhang, Q., Peng, H., Chen, C., and Wei, F. (2015). Permselective graphene oxide membrane for highly stable and anti-self-discharge lithiumsulfur batteries. *ACS Nano*, 9(3):3002–3011.

International Energy Agency (2009). *Gadgets and Gigawatts - Policies for Energy Efficiency*. International Energy Agency. `https://www.iea.org/publications/freepublications/publication/gadgets-and-gigawatts-policies-for-energy-efficient-electronics.html`; Accessed: 25/04/2015.

Janesick, J. (2001). *Scientific Charge-Coupled Devices*, volume 83. SPIE press, Washington.

Jesson, D. and Pennycook, S. (1995). Incoherent Imaging of Crystals Using Thermally Scattered Electrons. *Proceedings of the Royal Society of London A: Mathematical, Physical and Engineering Sciences*, 449(1936):273–293.

Jiang, Z., Li, C., Hao, S., Zhu, K., and Zhang, P. (2014). An easy way for preparing high performance porous silicon powder by acid etching AlSi alloy powder for lithium ion battery. *Electrochimica Acta*, 115(0):393 – 398.

Johnson, C., Li, N., Vaughey, J., Hackney, S., and Thackeray, M. (2005). Lithium Manganese Oxide Electrodes with Layered-Spinel Composite Structures for Lithium Batteries. *Electrochemistry Communications*, 7(5):528 – 536.

Joy, D. (1991). An Introduction to Monte Carlo Simulations. *Scanning Microscopy*, 5(2):329–337.

Kanellopoulos, N. (2011). Nanoporous materials: Advanced techniques for characterization, modeling, and processing.

Ke, H., Luo, W., Cheng, G., Tian, X., and Pi, Z. (2009). Synthesis of Flower-like SnS_2 Nano-structured Microspheres using PEG 200 as Solvent. *Micro & Nano Letters, IET*, 4(3):177–180.

Kganyago, K. and Ngoepe, P. (2003). Structural and Electronic Properties of Lithium Intercalated Graphite LiC_6. *Phys. Rev. B*, 68:205111.

Kim, T., Kim, C., Son, D., Choi, M., and Park, B. (2007). Novel SnS_2 Nanosheet Anodes for Lithium-Ion Batteries. *Journal of Power Sources*, 167(2):529–535.

Kinsman, T. (2008). A Scanning Electron Microscope in the Dining Room. *Microscopy UK*. `http://www.microscopy-uk.org.uk/mag/artsep08/tk-sem.html`; Accessed: 07/12/2014.

Kirchhoff, G. and Bunsen, R. (1861). XXIV. - On Chemical Analysis by Spectrum-Observations. *Q. J. Chem. Soc.*, 13:270–289.

Klug, H. and Alexander, L. (1974). *X-ray Diffraction Procedures: for Polycrystalline and Amorphous Materials*. Wiley-VCH, New York.

Knapek, E. and Dubochet, J. (1980). Beam Damage to Organic Material is Considerably Reduced in Cryo-Electron Microscopy. *Journal of Molecular Biology*, 141(2):147–161.

Kübel, C., Niemeyer, D., Cieslinski, R., and Rozeveld, S. (2010). Electron tomography of nanostructured materialstowards a quantitative 3D analysis with nanometer resolution.

Langford, J. and Wilson, A. (1978). Scherrer After Sixty Years: A Survey and some New Results in the Determination of Crystallite Size. *Journal of Applied Crystallography*, 11(2):102–113.

Lechner, P., Fiorini, C., Hartmann, R., Kemmer, J., Krause, N., Leutenegger, P., Longoni, A., Soltau, H., Stötter, D., and Stötter, R. (2001). Silicon Drift Detectors for High Count Rate X-ray Spectroscopy at Room Temperature. *Nuclear Instruments and Methods in Physics Research Section A: Accelerators, Spectrometers, Detectors and Associated Equipment*, 458(1):281–287.

Lee, D. and Schachter, B. (1980). Two Algorithms for Constructing a Delaunay Triangulation. *International Journal of Computer & Information Sciences*, 9(3):219–242.

Lee, S., Han, J., Lee, Y., Jeong, M., Shin, W., Ue, M., and Choi, N. (2014). A bi-functional lithium difluoro(oxalato)borate additive for lithium cobalt oxide/lithium nickel manganese cobalt oxide cathodes and silicon/graphite anodes in lithium-ion batteries at elevated temperatures. *Electrochimica Acta*, 137(0):1 – 8.

Leung, K., Pincosy, P., and Ehlers, K. (1984). Directly Heated Lanthanum Hexaboride Filaments. *Review of Scientific Instruments*, 55(7).

Li, M., Yang, Y., Huang, B., Lou, X., Zhang, W., Han, M., and Ru, J. (2013). Development of advanced electron tomography in material science based on tem and stem. *Trans. Nonferrous.*

Li, W., Dahn, J., and Wainwright, D. (1994). Rechargeable Lithium Batteries with Aqueous Electrolytes. *Science*, 264(5162):1115–1118.

Li, X., Tang, S., Qu, M., Huang, P., Li, W., and Yu, Z. (2014). A novel spherically porous zr-doped spinel lithium titanate (li4ti5xzrxo12) for high rate lithium ion batteries. *Journal of Alloys and Compounds*, 588(0):17 – 24.

Li, Y., Bai, W., Zhang, Y., Niu, X., Wang, D., Wang, X., Gu, C., and Tu, J. (2015). Synthesis and electrochemical performance of lithium vanadium phosphate and lithium vanadium oxide composite cathode material for lithium ion batteries. *Journal of Power Sources*, 282(0):100 – 108.

Lichte, H. (1991). Optimum focus for taking electron holograms. *Ultramicroscopy*, 38.

Liu, S., Yin, X., Chen, L., Li, Q., and Wang, T. (2010a). Synthesis of Self-Assembled 3D Flowerlike SnS_2 Nanostructures with Enhanced Lithium Ion Storage Property. *Solid State Sciences*, 12(5):712–718.

Liu, S., Yin, X., Hao, Q., Zhang, M., Li, L., Chen, L., Li, Q., Wang, Y., and Wang, T. (2010b). Chemical Bath Deposition of SnS_2 Nanowall Arrays with Improved Electrochemical Performance for Lithium Ion Battery. *Materials Letters*, 64(21):2350–2353.

Love, G., Cox, M., and Scott, V. (1978). A Versatile Atomic Number Correction for Electron-Probe Microanalysis. *Journal of Physics D: Applied Physics.*

Magrez, A., Vasco, E., Seo, J., Dieker, C., Setter, N., and Forro, L. (2006). Growth of Single-Crystalline $KNbO_3$ Nanostructures. *The Journal of Physical Chemistry B*, 110(1):58–61.

Max Planck Institute for Intelligent Systems (2014). TEM Comparison Table. `http://www.is.mpg.de/15555205/TEM_Comparison_Table`. Accessed: 07/12/2014.

Meschede, D. (2010). *Gerthsen Physik - 24. Auflage.* Springer, Heidelberg.

Mollenkopf, J. (2011). *TESLA Forum - Technical Battery Discussion*. TESLA Motors. http://my.teslamotors.com/it_IT/forum/forums/technical-battery-discussion; Accessed: 16/06/2015.

Moore, D. and Wang, Z. (2006). Growth of Anisotropic One-Dimensional ZnS Nanostructures. *J. Mater. Chem.*, 16:3898–3905.

Moore, G. (1965). Cramming more components onto integrated circuits. *Electronics*.

Mouawad, J. (2014). Report on Boeing 787 Dreamliner Battery Flaws Finds Lapses at Multiple Points. *New York Times*.

Mpt-Matthew (2013). Lithium Polymer Battery. *https://en.wikipedia.org/wiki/Lithium_polymer_battery*. Accessed: 07/12/2014.

MTI Corporation (2013). Stainless Steel Spacer for CR20XX Cell. *MTI Corporation Catalogue*. http://www.mtixtl.com/304StainlessSteelSpacerforCR20XXCell15.4mmDiax0.2mm-EQ-CR20-.aspx; Accessed: 20/12/2014.

Muñoz-Rojas, D., Leriche, J., Delacourt, C., Poizot, P., Palacn, M., and Tarascon, J. (2007). Development and Implementation of a High Temperature Electrochemical Cell for Lithium Batteries. *Electrochemistry Communications*, 9(4):708 – 712.

NIST (2011). *Ethanol*. US National Institute of Standards and Technology. http://webbook.nist.gov/cgi/cbook.cgi?ID=C64175&Mask=4&Type=ANTOINE&Plot=on; Accessed: 20/12/2014.

Otten, M. and Coene, W. (1993). High-Resolution Imaging on a Field Emission TEM. *Ultramicroscopy*, 48:77–91.

Özer, N. and Lampert, C. (1995). Electrochemical Lithium Insertion in Sol-Gel Deposited $LiNbO_3$ Films. *Solar Energy Materials and Solar Cells*, 39(24):367 – 375. International Meeting of Electrochromism.

Panasonic (2015). *NCR18650 Catalogue*. Panasonic. http://industrial.panasonic.com/ww/products/batteries/secondary-batteries/lithium-ion/cylindrical-type/NCR18650; Accessed: 16/06/2015.

Particle Analytical (2014). Brunauer, Emmett and Teller (BET) Theory. http://particle.dk/methods-analytical-laboratory/surface-area-bet/surface-area-bet-theory/; Accessed: 07/12/2014.

Pawley, J. (1997). The Development of Field-Emission Scanning Electron Microscopy for Imaging Biological Surfaces. *Scanning*, 19:324–336.

Pennycook, S., Lupini, A., Varela, M., Borisevich, A., Peng, Y., Oxley, M., Benthem, K., and Chisholm, M. (2007). *Scanning Microscopy for Nanotechnology*. Springer.

Potts, P. (1987). Electron Probe Microanalysis. In *A Handbook of Silicate Rock Analysis*. Springer Netherlands.

Pralong, V., Reddy, M., Caignaert, V., Malo, S., Lebedev, O., Varadaraju, U., and Raveau, B. (2011). A New Form of $LiNbO_3$ with a Lamellar Structure Showing Reversible Lithium Intercalation. *Chemistry of Materials*, 23(7):1915–1922.

Reimer, L. and Kohl, H. (2008). *Transmission Electron Microscopy: Physics of Image Formation*, volume 36. Springer.

Rothschild, A., Sloan, J., and Tenne, R. (2000). Growth of WS2 nanotubes phases. *Journal of the American chemical Society*, 122(21):5169–5179.

Saïdi, M., Barker, J., Huang, H., Swoyer, J., and Adamson, G. (2003). Performance Characteristics of Lithium Vanadium Phosphate as a Cathode Material for Lithium-Ion Batteries. *Journal of Power Sources*, 119121(0):266 – 272. Selected papers presented at the 11th International Meeting on Lithium Batteries.

Sanyo Electric (2004). *Lithium Ion*. Sanyo Electric Ltd., Moriguchi (Japan).

Schlüter, C. and Schlüter, M. (1973). The Electronic Structure of SnS_2 and $SnSe_2$. *Physica Status Solidi (b)*, 57(1):145–155.

Schöllhorn, R., Kuhlmann, R., and Besenhard, J. (1976). Topotactic Redox Reactions and Ion Exchange of Layered MoO_3 Bronzes. *Materials Research Bulletin*, 11(1).

Seiler, H. (1983). Secondary Electron Emission in the Scanning Electron Microscope. *Journal of Applied Physics*, 54(11):R1–R18.

Seo, J., Jang, J., Park, S., Kim, C., Park, B., and Cheon, J. (2008). Two-Dimensional SnS_2 Nanoplates with Extraordinary High Discharge Capacity for Lithium Ion Batteries. *Advanced Materials*, 20(22):4269–4273.

Severin, K. (1999). *Cyclic Voltammetry*. Michigan State University. `http://www2.chemistry.msu.edu/courses/cem419/cem372cyclicvoltammetry.pdf`; Accessed: 20/12/2014.

Shi, W., Huo, L., Wang, H., Zhang, H., Yang, J., and Wei, P. (2006a). Hydrothermal Growth and Gas Sensing Property of Flower-shaped SnS_2 Nanostructures. *Nanotechnology*, 17(12):2918.

Shi, W., Huo, L., Wang, H., Zhang, H., Yang, J., and Wei, P. (2006b). Hydrothermal Growth and Gas Sensing Property of Flower-Shaped SnS_2 Nanostructures. *Nanotechnology*, 17(12):2918.

Smart Electronics (2013). *Lithium Ion: Technical Handbook*. Gold Peak Industries Ltd., Hongkong.

Smil, V. (2010). *Energy Transitions: History, Requirements, Prospects*. Praeger.

Sony Corporation (2014). *Lithium Ion Rechargeable Batteries: Technical Handbook*. Sony Corporation.

Steyn, J. and Holt, D. (1976). An Efficient Spectroscopic Detection System for Cathodoluminescence Mode Scanning Electron Microscopy (SEM). *Journal of Microscopy*, 107(2):107–128.

Summerfield, J. (2013). Modeling the Lithium Ion Battery. *Journal of Chemical Education*.

Sunkara, M. (2014). Tin oxide nanowires as high energy density anodes for lithium-ion batteries. In *225th ECS Meeting (May 11-15, 2014)*. ECS.

Takami, N., Ohsaki, T., and Inada, K. (1992). The Impedance of Lithium Electrodes in $LiPF_6$-Based Electrolytes. *Journal of The Electrochemical Society*, 139(7):1849–1854.

Tang, Y., Yang, L., Qiu, Z., and Huang, J. (2009). Template-Free Synthesis of Mesoporous Spinel Lithium Titanate Microspheres and their Application in High-Rate Lithium Ion Batteries. *J. Mater. Chem.*, 19:5980–5984.

Tanzilli, S., Riedmatten, H. D., Zbinden, H., Baldi, P., Micheli, M. D., Ostrowsky, D., and Gisin, N. (2001). Highly Efficient Photon-Pair Source using Periodically Poled Lithium Niobate Waveguide. *Electronics Letters*, 37(1):26–28.

Tarascon, J. and Armand, M. (2001). Issues and Challenges Facing Rechargeable Lithium Batteries. *Nature*, 414.

Tesla Motors Inc. (2014). Tesla Model S Specs. `http://www.teslamotors.com/en_GB/models/specs`; Accessed: 15/12/2014.

Thach, R. and Thach, S. (1971). Damage to Biological Samples Caused by the Electron Beam During Electron Microscopy. *Biophysical Journal*, 11(2):204–210.

Thackeray, M., David, W., Bruce, P., and Goodenough, J. (1983). Lithium Insertion into Manganese Spinels. *Materials Research Bulletin*, 18(4):461 – 472.

The Economist (2002). Hooked on Lithium. *The Economist Science Technology Quarterly Q2*. Accessed: 07/12/2014.

Thinius, S., Islam, M., Heitjans, P., and Bredow, T. (2014). Theoretical study of lithium migration in lithiumgraphite intercalation compounds with dispersion-corrected dft methods. *The Journal of Physical Chemistry C*, 118(5):2273–2280.

Towada, J., Karouji, T., Sato, H., Kadoma, Y., Shimada, K., and Ui, K. (2015). Charge and discharge characteristics of natural graphite electrode in N, N-diethyl-N-methyl-N-(2-methoxyethyl)ammonium bis(trifluoromethylsulfonyl)amide containing lithium ion for lithium-ion secondary batteries. *Journal of Power Sources*, 275(0):50 – 54.

Travessa, D., Silva, F., Cristovan, F., Jorge, J., and Cardoso, K. (2014). Ag Ion Decoration for Surface Modifications of Multi-Walled Carbon Nanotubes. *Materials Research*, 17:687 – 693.

Tuggle, D. and Swanson, L. (1985). Point Cathodes for use in Virtual Source Electron Optics. *J. Vac. Sci. Technol. B*.

Tverberg, G. (2012). *World Energy Consumption Since 1820 in Charts*. Our Finite World. `http://ourfiniteworld.com/2012/03/12/world-energy-consumption-since-1820-in-charts/`; Accessed: 25/04/2015.

U.S. Census Bureau (2013). *Total Midyear Population for the world 1950-2050*. U.S. Census Bureau. `http://www.census.gov/population/international/data/worldpop/table_population.php`; Accessed: 25/04/2015.

Venugopal, G., Hunt, A., and Alamgir, F. (2010). Nanomaterials for Energy Storage in Lithium-ion Battery Applications. *Mater. Matter*, 5:42–45.

Vine, J. and Einstein, P. (1964). Heating Effect of an Electron Beam Impinging on a Solid Surface, Allowing for Penetration. *Electrical Engineers, Proceedings of the Institution of*, 111(5):921–930.

Vu, A. and Stein, A. (2014). Lithium iron phosphate spheres as cathode materials for high power lithium ion batteries. *Journal of Power Sources*, 245(0):48 – 58.

Wahl, A. (2005). A Short History of Electrochemistry. *Galvanotechnik*, 96.

Wang, X., Xing, L., Liao, X., Chen, X., Huang, W., Yu, Q., Xu, M., Huang, Q., and Li, W. (2015). Improving cyclic stability of lithium cobalt oxide based lithium ion battery at high voltage by using trimethylboroxine as an electrolyte additive. *Electrochimica Acta*, 173(0):804 – 811.

Watanabe, S., Kinoshita, M., Hosokawa, T., Morigaki, K., and Nakura, K. (2014). Capacity fading of $LiAl_yNi_{1-x-y}Co_xO_2$ cathode for lithium-ion batteries during accelerated calendar and cycle life tests (effect of depth of discharge in charge-discharge cycling on the suppression of the micro-crack generation of $LiAl_yNi_{1-x-y}Co_xO_2$ particle) . *Journal of Power Sources*, 260(0):50 – 56.

Weis, R. and Gaylord, T. (1985). Lithium niobate: summary of physical properties and crystal structure. *Applied Physics A*, 37(4):191–203.

White, E. (2014). *Wet cells and dry cells: in situ transmission electron microscopy of electrically-driven, dynamical processes*. UCLA.

Whittingham, M. (1976). Electrical Energy Storage and Intercalation Chemistry. *Science*, 192(4244):1126–1127.

Wilka, M. (2013). *Dissertation: Untersuchungen von Polarisationseffekten an Lithium-Ionen-Batterien und deren Einfluss auf Sicherheit, Alterung sowie weiterer anwendungsrelevanter Eigenschaften*. Universität Ulm (Germany), Fakultät für Naturwissenschaften.

Williams, D. and Carter, C. (2009). *Transmission Electron Microscopy: A Textbook for Materials Science*. Springer.

Winter, M. and Brodd, R. (2004). What Are Batteries, Fuel Cells, and Supercapacitors? *Chemical Reviews*, 104(10):4245–4270.

Wittke, J. (2008). *GLG 510 - Microbeam Techniques in Geology*. Northern Arizona University. `http://www4.nau.edu/microanalysis/Microprobe/NewOverview.html`.

Wu, P., Du, N., Zhang, H., Liu, J., Chang, L., Wang, L., Yang, D., and Jiang, J. (2012). Layer-Stacked Tin Disulfide Nanorods in Silica Nanoreactors with Improved Lithium Storage Capabilities. *Nanoscale*, 4:4002–4006.

Yazami, R. (1999). Surface Chemistry and Lithium Storage Capability of the Graphite-Lithium Electrode. *Electrochimica Acta*, 45(12):87 – 97.

Yazami, R. and Touzain, P. (1983). A Reversible Graphite-Lithium Negative Electrode for Electrochemical Generators. *Journal of Power Sources*, 9(3):365 – 371.

Yoshino, A., Sanechika, K., and Nakajima, T. (1987). Secondary Battery (US4668595 A). *United States Patent*.

Yoshio, M., Brodd, R., and Kozawa, A. (2010). *Lithium-Ion Batteries: Science and Technologies*. Springer Science and Business Media.

Yoshizawa, H. and Ohzuku, T. (2007). An Application of Lithium Cobalt Nickel Manganese Oxide to High-Power and High-Energy Density Lithium-Ion Batteries. *Journal of Power Sources*, 174(2):813 – 817. 13th International Meeting on Lithium Batteries.

Zanini, M., Basu, S., and Fischer, J. (1978). Alternate Synthesis and Reflectivity Spectrum of Stage 1 Lithium-Graphite Intercalation Compound. *Carbon*, 16(3):211 – 212.

Zhai, C., Du, N., and Yang, H. (2011). Large-Scale Synthesis of Ultrathin Hexagonal Tin Disulfide Nanosheets with Highly Reversible Lithium Storage. *Chemical Communications*, 47(4):1270–1272.

Zhang, H., Zhang, Q., Tang, J., and Qin, L. (2005). Single-crystalline LaB_6 Nanowires. *Journal of the American Chemical Society*, 127(9):2862–2863.

Zhu, H., Ji, X., and Yang, D. (2006). Hydrothermal Synthesis and Characterization of Novel Aloe-like SnS_2 Nanostructures. *Journal of Materials Science*, 41(11):3489–3492.

Zhu, Y., Sekine, T., Li, Y., Wang, W., Fay, M., Edwards, H., Brown, P., N. Fleischer, N., and Tenne, R. (2005). WS_2 and MoS_2 inorganic fullerenes - super shock absorbers at very high pressures. *Advanced Materials*, 17(12):1500–1503.

Zhuang, Q., Qui, X., Xu, S., Qiang, Y., and Sun, S. (2012). Diagnosis of Electrochemical Impedance Spectroscopy in Lithium-Ion Batteries. In Belharouak, I., editor, *Lithium Ion Batteries - New Developments*. InTech, Rijeka (Croatia).